Title

Evolutionary Warfare: Characterizing Viral Antagonism of Host Innate Immune Components

Permalink

https://escholarship.org/uc/item/22w2s5n7

Author

Beierschmitt, Christopher

Publication Date

2022

Supplemental Material

https://escholarship.org/uc/item/22w2s5n7#supplemental

Peer reviewed|Thesis/dissertation

UNIVERSITY OF CALIFORNIA SAN DIEGO

Evolutionary Warfare: Characterizing Viral Antagonism of Host Innate Immune Components

A Dissertation submitted in partial satisfaction of the requirements
for the degree Doctor of Philosophy

in

Biology

by

Christopher Beierschmitt

Committee in charge:

    Professor Matthew Daugherty, Chair
    Professor Tariq Rana
    Professor Samara Reck-Peterson
    Professor Alistair Russell
    Professor Erica Ollmann Saphire
    Professor Emily Troemel

2022

The Dissertation of Christopher Beierschmitt is approved, and it is acceptable in quality and form for publication on microfilm and electronically.

University of California San Diego

2022

DEDICATION

This work is dedicated to the memory of Gina Kosla and Dr. Chinweike Okegbe.

EPIGRAPH

"An ant hurries along a threshing floor with its wheat grain, moving between huge stacks of wheat, not knowing the abundance all around. It thinks its one grain is all there is to love. So, we choose a tiny seed to be devoted to. This body, one path, or one teacher. Look wider and farther. The essence of every human being can see, and what that essence-eye takes in, the being becomes. Saturn. Solomon! The ocean pours through a jar, and you might say it swims *inside* the fish! This mystery gives peace to your longing and makes the road home, *home*."
-Rumi, "The Road Home"

"Great!"
-Matthew Daugherty, PhD.

TABLE OF CONTENTS

LIST OF SUPPLEMENTARY FILES

beierschmitt_supplementary_files.zip. Contains Supplementary files 2.1-3.6.

Supplementary File 2.1. Training set of enteroviral polyproteins.

Supplementary File 2.2. Enteroviral polyproteins with unique 8mer 3Cpro cleavage site concatenations.

Supplementary File 2.3. Un-optimized 3Cpro cleavage motif scores for true positive, false positive, and human sites within the enteroviral polyprotein and human training sets.

Supplementary File 2.4. Optimized 3Cpro cleavage motif scores for true positive, false positive, and human sites within the enteroviral polyprotein and human training sets.

Supplementary File 2.5. List of primers and gBlocks used.

Supplementary File 2.6. List of antibodies used for immunoblots.

Supplementary File 3.1. Evolutionary analyses on dynein, dynactin, and activating adaptor genes.

Supplementary File 3.2. Codon positions in NINL predicted to be evolving under positive selection.

Supplementary File 3.3. Evolutionary analysis of N-terminal and C-terminal domains of NINL.

Supplementary File 3.4. Differentially regulated transcripts in WT A549, NINL KO, and NIN KO cell lines induced and uninduced with IFN.

Supplementary File 3.5. List of primers and gBlocks used.

Supplementary File 3.6. List of antibodies used for immunoblots and immunofluorescence.

LIST OF FIGURES

LIST OF TABLES

ACKNOWLEDGEMENTS

For his role as my mentor and thesis advisor, I would like to thank Professor Matt Daugherty at University of California San Diego. Throughout my time in his lab, Matt has given me the tools and freedom to explore science that is exciting, intellectually stimulating, and applicable to my future endeavors as a scientist. Beyond this, he has cultivated a lab environment that encourages a supportive, constructive, and collaborative spirit. I am lucky to have worked with such a creative and passionate investigator.

For giving me my first experience in a research laboratory and establishing the foundation upon which I have built an identity as a scientist, I would like to thank Professor Lars Dietrich at Columbia University. I entered the Dietrich Lab with plenty of enthusiasm, but no experience to match. Through direct mentorship and by establishing mentoring relationships with several talented scientists, I was able to learn and gain more hands-on experience than I would have ever dreamed possible. Although many people in this lab were kind enough to work with me, I want to specifically thank Dr. Abigail Sporer, Dr. Jeanyoung Jo, Dr. Chinweike Okegbe, and William Cole Cornell for the extensive time and energy they spent with me.

Although they are specifically acknowledged as co-authors, I want to emphasize my gratitude to Donté Alexander Stevens, Professor Sam Reck-Peterson, and Dr. Brian Tsu for being wonderful scientific collaborators. Entering into a research project with multiple "first authors" is an exercise in communication, patience, and intellectual growth. These individuals made for fantastic partners in research, and I am grateful to have had the privilege of working with them.

I would like to thank the members of the Daugherty Lab, the Reck-Peterson Lab, and my PhD committee for invaluable feedback on research presentations, written proposals, and

Chapter 2 is published and can be found available in eLife in Immunology and Inflammation Microbiology and Infectious Disease 2021, including co-authors Brian V. Tsu, Andrew P. Ryan, Rimjhim Agarwal, Patrick S. Mitchell and Matthew D. Daugherty. I, Christopher Beierschmitt, am the co-first author of this paper, alongside Brian V. Tsu.

Chapter 3 has been submitted for review. It can be found on the BioRxiv preprint server at https://www.biorxiv.org/content/10.1101/2022.07.11.499552v1. It includes co-authors Donté A. Stevens, Swetha Mahesula, Miles R. Corley, John Salogiannis, Brian V. Tsu, Bryant Cao, Andrew P. Ryan, Samara Reck-Peterson, and Matthew D. Daugherty. I, Christopher Beierschmitt, am the co-first author of this paper, alongside Donté A. Stevens.

If I try to thank everyone by name, I'm sure I will forget someone. Thank you to my friends and family for their support, inspiration, encouragement, and optimism. I love you.

VITA

2017   Bachelor of Arts in Biological Sciences, Columbia University

2022   Doctor of Philosophy in Biology, University of California San Diego

PUBLICATIONS

Tsu B.V.†, Beierschmitt C.†, Ryan A.P., Agarwal R., Mitchell P.S., Daugherty M.D. "Diverse viral proteases activate the NLRP1 inflammasome." eLife. 2021.

Nguyen K.T., Sugie J., Khanna K., MacKennon E.E., Birkholz E.A., Lee J., Beierschmitt C., Villa E., Pogliano J. Selective transport of fluorescent proteins into the phage nucleus. PLOS One. 2021.

Beierschmitt C.†, Sporer A.J.†, Bendebury A., Zink Z.E., Price-Whelan A., Buzzeo M.C., Sanchez L.M., Dietrich L.E.P. *Pseudomonas aeruginosa* PumA acts on an endogenous phenazine to promote self-resistance. Microbiology. 2018.

Okegbe C., Fields B.L., Cole S.J., Beierschmitt C., Price-Whelan A., Stewart R.C., Lee V.T., Dietrich L.E.P. Electron-shuttling antibiotics structure bacterial communities by modulating cellular levels of c-di-GMP. Proc Natl Acad Sci. 2017.

PUBLICATIONS SUBMITTED OR IN PREPARATION

Stevens D.A.†, Beierschmitt C.†, Mahesula S., Corley M., Salogiannis J., Tsu B.V., Cao B., Ryan A.P., Reck-Peterson S.‡, Daugherty M.D.‡ Antiviral function and viral antagonism of the rapidly evolving dynein activating adapter NINL.

Tsu B.V., Agarwal R., Beierschmitt C., Fay E.J., Castro L.K., Ryan A.P., Mitchell P.S., Daugherty MD. CARD8 is a rapidly evolving and polymorphic sensor of diverse viral proteases.

† denotes equal contribution
‡ denotes co-corresponding authors

ABSTRACT OF THE DISSERTATION

Evolutionary Warfare: Characterizing Viral Antagonism of Host Innate Immune Components

by

Christopher Beierschmitt

Doctor of Philosophy in Biology

University of California San Diego, 2022

Professor Matthew Daugherty, Chair

Host-pathogen conflicts are major drivers of evolution and generate a seemingly endless array of challenges to the fields of medicine and scientific research. While extensive work has been conducted to combat diseases caused by viruses and to understand their molecular mechanisms, there is a need for better tools to identify and predict host components that have interacted with viruses over evolutionary history. By seeking out these evolutionary battlegrounds, we can discover novel and otherwise difficult-to-identify struggles between

viruses and their hosts. Many logical host targets, such as sensors of non-self markers and effectors of the immune system have been characterized as important players in host defense. Here, I describe two instances of the evolution-guided discovery of unique viral interactors of the host innate immune response. The first chapter characterizes a host-evolved "tripwire" immune sensor that baits viruses into activation, and the second chapter details virus-driven evolution of a previously undescribed effector of the host innate immune response.

Chapter 1: Introduction and Overview

Viruses and hosts: war all the time

For as long as humans have existed, viruses have adapted to use us as their hosts (Nasir 2020, Stringer 2016). Throughout evolutionary history, viral interaction with the human lineage has been so extensive that roughly 8% of the human genome is comprised of endogenized viral components (Lander 2001, Grandi 2018). As obligate intracellular parasites, viruses require resources from host cells in order to complete their replicative cycle. In order to evade detection by the host's immune defenses, viruses have developed a wide array of tools to increase their success in parasitizing necessary host resources (Iwasaki, 2012; Schneider, 2014). These tools, in turn, have necessitated defensive and proactive innovations on the part of the host to defend against viral invaders (Janeway, 1989; Akira, 2006, Thompson, 2011). Historically, candidate sites of viral antagonism have been investigated after previously being identified as antiviral genes or components of innate immune response pathways (Meyerson, 2011; Schneider, 2014; King, 2022). While this has yielded important information in the production of antiviral therapeutics and our understanding of interactions, this *post hoc* approach is likely failing to capture important evolutionary battlegrounds between viruses and their hosts. Here, I will introduce an evolution-guided method to identify potentially interesting host-virus conflicts, as well as some examples of the results this method has yielded. These ideas will be covered in greater depth in Chapters 2 and 3.

Looking back in time

Practically limitless environmental factors can bias the rate of evolutionary selection, but the necessary material for all evolution is genetic mutation. Evolution can, retrospectively, be

quantified and ranked by how closely a mutational rate approximates a process of neutral selection. One of the earliest established metrics of measuring mutational bias is dN/dS ratio (also known as omega), or the observed rate of non-synonymous vs synonymous codon changes for a given coding region (Jeffares, 2015). Because the nucleic acid coding scheme for amino acids is degenerate, not every nucleotide change will necessarily result in a translational change. In an ideal system, neutral selection of a coding region is described by a dN/dS ratio of 1—that is, the rate of observed non-synonymous coding changes approximates the rate of synonymous coding changes. Accordingly, if a given region is experiencing a higher rate of non-synonymous substitutions than neutrality would predict, we observe a dN/dS ratio greater than 1 and would classify this as "positive selection." Finally, when the rate of synonymous coding changes exceeds the rate of non-synonymous changes, we see a dN/dS ratio approaching 0 and call this "purifying selection." Regardless of organism, genes that are crucial for sustaining life and housekeeping functions most often display signatures of purifying selection, while genes that are involved with adaptive immunity will show signs of recurrent positive selection. Other evolutionary modeling tools, such as PAML, MEME, and FIMO use a similar logic and different statistical analyses to score evolutionary rate (Yang, 2007; Bailey, 2009). By analyzing orthologous sequences across species, from closest related to most distant, we can infer whether something might be changing more often than randomness predicts. This type of recurrent positive selection is, in some cases, driven by viral antagonism. In order to narrow down which sites of rapid evolution might be sites of conflict, we needed tools from the virus side of the equation.

Dual purpose tools: viral proteases

All known viruses encode components that assist them in completing their replicative cycle in a host cell. While some larger viruses have evolved tools whose explicit purpose appears to be antagonizing their hosts, most viruses must be more resourceful due to their relatively small genome size. One fantastic example of viral ingenuity comes in the form of 3C proteases of the *Picornaviridae* family (Tsu, 2021). The genomes of these positive sense, single-strand RNA viruses are translated by the host cell machinery into a single genomic polyprotein (Figure 1.1). These viruses, however, do not rely on host enzymatic activity to process this polyprotein into its necessary structural and non-structural components; they encode their own proteases. One such protease, the 3C protease, self-matures and proceeds to cleave the polyprotein in a site-specific fashion, liberating individual components, and allowing the virus to start its replicative cycle. Importantly, if this protease fails to complete this function properly, the virus is stopped dead in its tracks. In addition to polyprotein processing, the 3C protease of the *Picornaviridae* family is well-characterized as a direct antagonist of known host innate immune components (Sun, 2016). The fact that viruses *require* site-specific enzymatic function of the protease and there is strong selective pressure to retain this function, but that it also is an apparently important tool for defeating host defenses, makes it a uniquely exploitable tool for identifying potential sites of uncharacterized host-virus interactions.
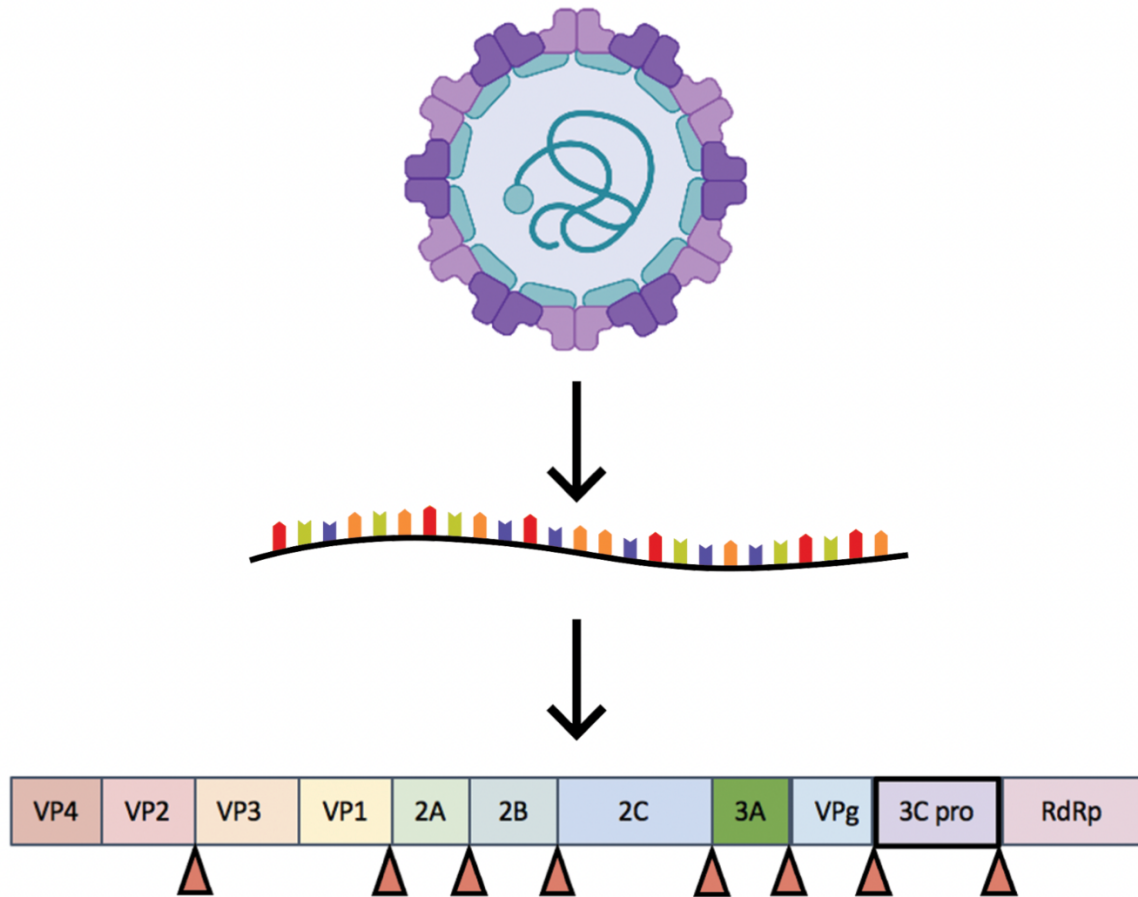
Figure 1.1. Enteroviruses encode a +ssRNA genome, which is translated into a single genomic polyprotein. Cartoon showing the progression from complete virion, to release of the positive-sense single strand RNA genome into the host cell. From there, it is translated by host machinery into a genomic polyprotein. A self-encoded 3C protease (highlighted by a thick black box above) is responsible for cleaving the polyprotein in a sequence-specific manner at sites between the structural and non-structural subunits (orange triangles), in addition to antagonizing an array of host target genes. The polyprotein cartoon is adapted from Brain Tsu (unpublished).

The intersection of viral and host evolution

By comparing viral polyprotein cleavage sites for different viruses within the *Picornaviridae* family, our group was able to generate an 8-mer amino acid consensus cleavage motif for their 3C protease (this is covered in greater detail in Chapter 2). This motif, though somewhat degenerate, can be queried against coding sequence databases to validate known viral

targets and potentially identify novel sites of interaction. More importantly, this consensus motif can be cross-referenced with sequences that we have previously identified as "rapidly evolving." The combination of signatures of rapid evolution with 3C protease cleavage sites suggests not only that a gene is evolving quickly, but that the changes observed may have been engendered by viral pressure. This evolution-guided pipeline allows us to begin a line of inquiry not necessarily based on phenotype or conventional logic, but by what the genome's changes over time are suggesting (Figure 1.2). Potential candidates are then validated, first by confirming that viral proteases can cleave as predicted *in vitro*, then by mutating predicted residues within the target site to confirm that they are important for enzymatic cleavage, and ideally by confirming the above observations with replication-competent virus in living cells. From here, the molecular mechanisms and functional consequences of disrupting this interaction can be assayed in any number of biological model systems. The results of this screening system have revealed new methods of interaction for previously described immune pathways and well as completely new components of long-known innate immune responses.
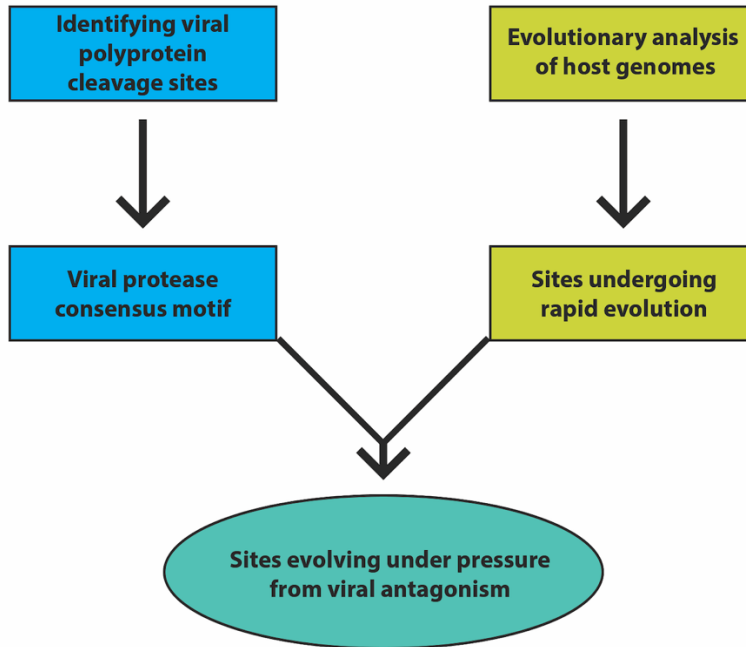
Figure 1.2. A novel discovery pipeline for host targets of viral antagonism. A diagram describing the workflow for generating a viral protease consensus motif (blue, left) and identification of rapidly evolving sites within a host data set (yellow, right). Genes or gene regions that are both undergoing rapid evolution and have high-confidence viral protease cut sites (green, center) and good candidates for novel genes involved in host immunity.

Tripwire activation of established targets

Early host recognition and response to pathogens is achieved by many different sensors of physical components as well as activity of pathogenic invaders (Akira, 2006; Iwasaki, 2012). While pattern recognition has been explored for decades and characterized as the primary method of pathogen detection, more recent research has begun to investigate the activity of pathogen-encoded antagonists. This type of detection has been named "effector-triggered immunity" (ETI), and one such system, the NLRP1 inflammasome, is covered in detail in Chapter 2. It was previously known that the *Bacillus anthrasis* Lethal Toxin protease (LeTx) cleaved a mouse ortholog of human NLRP1, named NLRP1B (Chavarría-Smith, 2013). Upon cleavage and N-terminal processing by the proteasome, a C-terminal caspase activating and recruiting domain (CARD) is liberated, where is complexes with and activates Caspase-1. Active

Caspase-1 then causes the maturation and release of pro-inflammatory cytokines, which activates an inflammatory response and pyroptotic cell death in the neighboring cells. Two details of this system are particularly interesting in the context of host-virus evolution. Firstly, the LeTx cleavage site is rapidly evolving and is not conserved from mice to humans. As such, LeTx is unable to cleave human NLRP1 and activate the downstream response. We found that the human cleavage site has, however, evolved to be cleavable by some 3C proteases encoded by viruses of the *Picornaviridae* family. This suggests that this NLRP1 inflammasome has independently evolved to be cleaved by a diverse range of pathogens. Secondly, unlike most previously described instances of ETI, cleavage of NLRP1 does not inactivate it, but activates it and facilitates the inflammatory response. This mechanism, which we've described as a "tripwire," is a case of the host evolving to be cut, rather than evolving to avoid cleavage (Figure 1.3). This finding was fascinating and hinted that other examples of tripwire systems might be identified. Indeed, it appears that a protein that shares similar domain elements to NLRP1, CARD8, is another tripwire sensor that activates an inflammatory response. Research on CARD8 as well as other potential tripwires is part of our group's ongoing research.
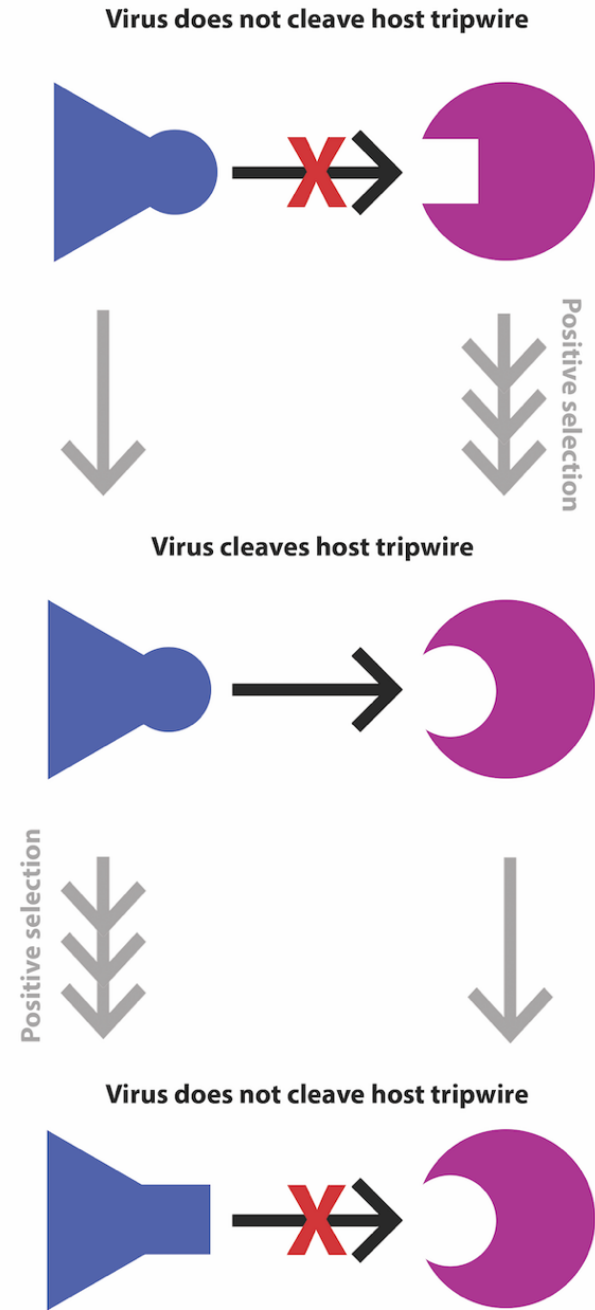
Figure 1.3. Tripwire proteins select for mutations that allow viral cleavage. The above cartoon illustrates a scenario where a viral protease (blue) does not initially cleave a host tripwire sequence (purple). Selective pressure chooses viral sequences that are able to be cut by viral proteases. In turn, this places selective pressure on proteases to evolve away from activating the host tripwire.

Attacking the transport, not just the cargo

Viruses have been shown to antagonize every major component of the type I interferon response. One branch of this response, the JAK-STAT pathway, is well-described in basic research and medicine as being an important precursor to the production of anti-viral interferon-stimulated genes (ISGs), among other important cellular responses (Darnell, 1994). Dysfunction of the JAK-STAT pathway is implicated in an array of different human diseases (O'Shea, 2015). While the characterized components of this pathway are known viral targets, it was previously unexplored how viruses might be disrupting the transport of these proteins and complexes (Figure 1.4). In Chapter 3, we describe antagonism of the dynein activating adapter, ninein-like (NINL). Activating adapters are interchangeable components of the dynein molecular motor, which are essential for procession along the microtubule, and have only recently begun to be understood. Each activating adapter has different cargo specificities—most of which have been largely undescribed in literature so far (Reck-Peterson, 2018). Through our pipeline analysis, we found that out of thirteen known activating adapters of dynein, NINL (and interestingly, not its closely related paralog, ninein) was the only one that appeared to be rapidly evolving. Further analysis revealed three high-probability 3C protease cut sites in human NINL, suggesting that viruses could be driving the evolution of this gene. This theory was further supported following evolutionary analysis, where we found that many primate orthologs of NINL were predicted to be uncleavable, suggesting a canonical host-virus evolutionary struggle (Figure 1.5). To determine whether NINL was involved in some sort of antiviral function, we generated knock-out cell lines and infected these cells with various viruses. All viruses tested showed increased

replication in the absence of NINL. Because the interferon response is one of the primary ways hosts respond to viral infection, we tested whether this pathway was functioning as normal. The production of ISGs (on a protein level, as well as on a transcriptional level) was diminished, but the phosphorylation of STAT1 and STAT2 was uninterrupted. This suggests that cleavage of NINL somehow prevents the transcription of ISGs after STAT phosphorylation. Further research is necessary to elucidate the exact mechanism of NINL and whether its involvement in innate immunity is truly dynein dependent or not. Since we began this research, more activating adapters of dynein have been discovered. Early analyses suggest that at least one of these new activating adapters deserves further investigation, as it appears to be rapidly evolving as well.
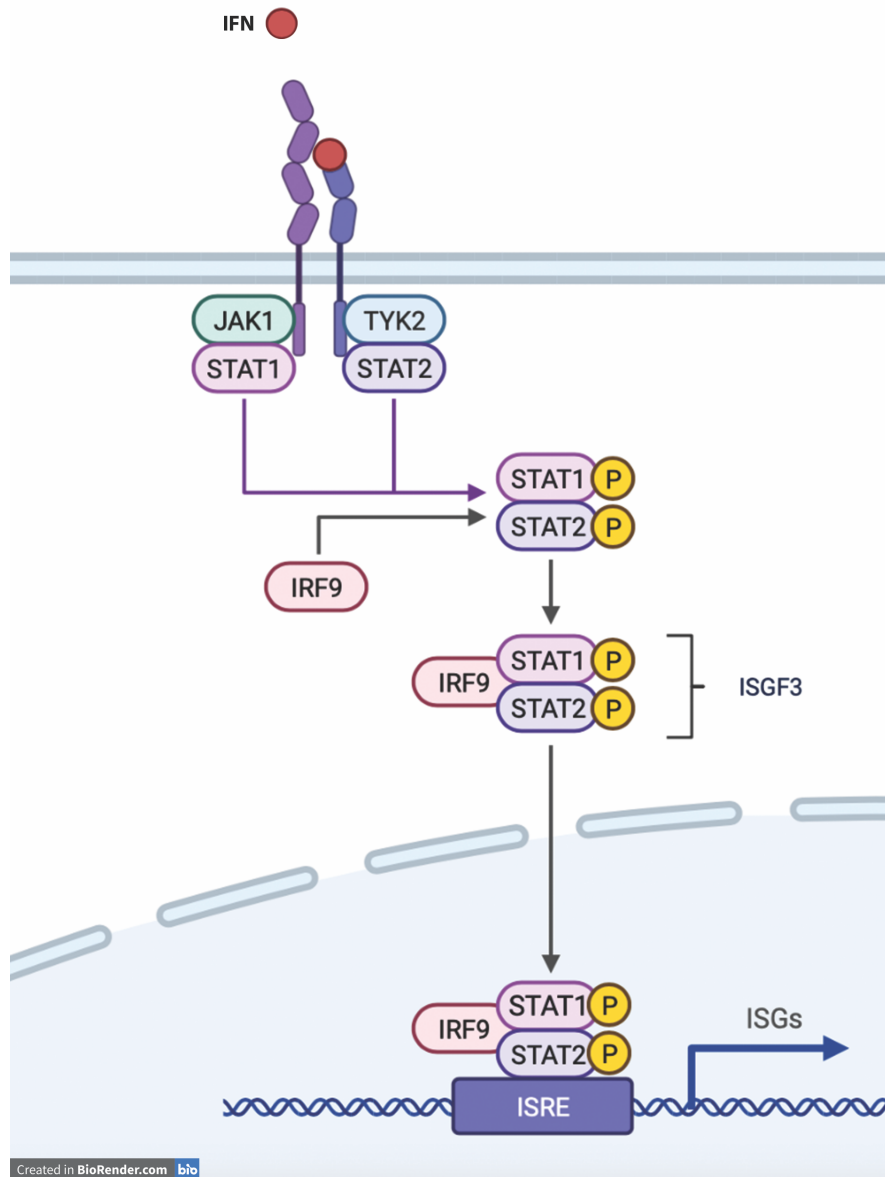
Figure 1.4. The JAK-STAT pathway. Cartoon of the JAK-STAT pathway from the receipt of IFN signal to the production of ISGs. Adapted from BioRender.com
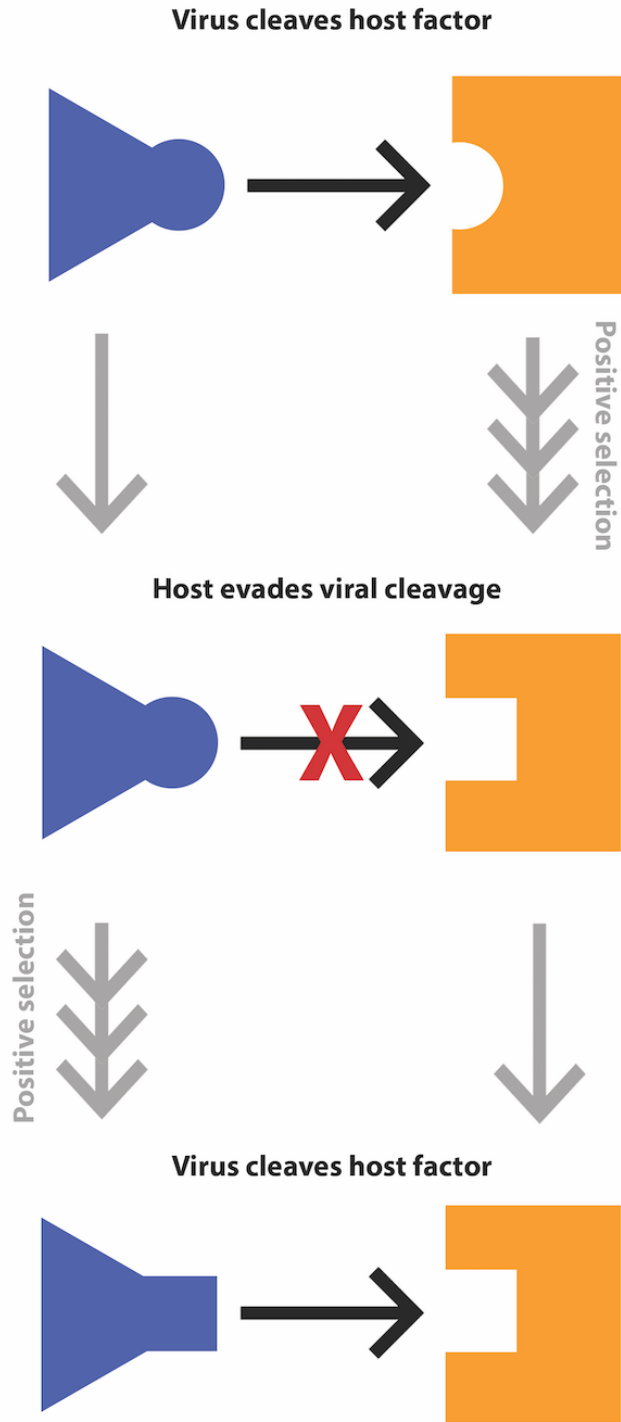
Figure 1.5. Host-virus evolutionary arms race. The above cartoon shows a scenario where a viral protease (blue) successfully recognizes and defeats a host antiviral protein (orange). This places selective pressure on the host, which selects for mutations that are able to evade viral attack. In turn, this places evolutionary pressure on the virus to be able to once again recognize the new host protein.

The future of discovery

In the case of both NLRP1 and NINL, we used an evolution-guided approach to identify novel targets of viral antagonism. Beyond this, though, we were able to make site-specific, validated predictions of where these viruses were attacking. From there, we dissected host systems to better understand the roles of our genes of interest. The NLRP1 story describes a novel host evolutionary strategy—to evolve to be cleaved by an existing viral protease. The target, however, was already well-known as an effector of the cellular immune response. On the other hand, the role of NINL has been largely uncharacterized, but the evolutionary battle it has undergone with viruses is similar to many others—direct viral antagonism results in increased viral success. These two stories are just the beginning of what our discovery pipeline has to offer. I am confident that this approach will yield innovative findings in the fields of virology and immunology for years to come.

References

Akira S, Uematsu S, Takeuchi O. 2016. Pathogen recognition and innate immunity. *Cell*. **124**(4):783-801. doi: 10.1016/j.cell.2006.02.015.

Bailey TL, Boden M, Buske FA, Frith M, Grant CE, Clementi L, Ren J, Li WW, Noble WS. 2009. MEME SUITE: tools for motif discovery and searching. *Nucleic Acids Res*. **W202**-8. doi: 10.1093/nar/gkp335.

Chavarría-Smith J, Vance RE. 2013. Direct proteolytic cleavage of NLRP1B is necessary and sufficient for inflammasome activation by anthrax lethal factor. *PLoS Pathog*. **9**(6):e1003452. doi: 10.1371/journal.ppat.1003452.

Darnell JE Jr, Kerr IM, Stark GR. 1994. Jak-STAT pathways and transcriptional activation in response to IFNs and other extracellular signaling proteins. *Science*. **264**(5164):1415-21. doi: 10.1126/science.8197455.

Grandi N, Tramontano E. 2018. Human Endogenous Retroviruses Are Ancient Acquired

Elements Still Shaping Innate Immune Responses. *Front Immunol*. **9**:2039. doi: 10.3389/fimmu.2018.02039.

Iwasaki A. 2012. A virological view of innate immune recognition. *Annu Rev Microbiol*. **66**:177-96. doi: 10.1146/annurev-micro-092611-150203.

Janeway, C. A., Jr. 1989. Approaching the asymptote? Evolution and revolution in immunology. *Cold Spring Harb Symp Quant Biol, 54 Pt 1*, 1-13. doi:10.1101/sqb.1989.054.01.003

Jeffares DC, Tomiczek B, Sojo V, dos Reis M. 2015. A beginners guide to estimating the non-synonymous to synonymous rate ratio of all protein-coding genes in a genome. *Methods Mol Biol*. **1201**:65-90. doi: 10.1007/978-1-4939-1438-8_4.

King K, Larsen BB, Gryseels S, Richet C, Kraberger S, Jackson R, Worobey M, Harrison JS, Varsani A, Van Doorslaer K. 2022. Coevolutionary Analysis Implicates Toll-Like Receptor 9 in Papillomavirus Restriction. *mBio*. **13**(2):e0005422. doi: 10.1128/mbio.00054-22.

Lander ES, Linton LM, Birren B, Nusbaum C, Zody MC, Baldwin J, et al. 2001. Initial sequencing and analysis of the human genome. *Nature*. **412**:860–921. doi: 10.1038/35057062

Meyerson, N. R., & Sawyer, S. L. 2011. Two-stepping through time: mammals and viruses. *Trends Microbiol*, **19**(6), 286-294. doi:10.1016/j.tim.2011.03.006

Nasir A, Romero-Severson E, Claverie JM. 2020. Investigating the Concept and Origin of Viruses. *Trends Microbiol*. **28**(12):959-967. doi: 10.1016/j.tim.2020.08.003.

O'Shea JJ, Schwartz DM, Villarino AV, Gadina M, McInnes IB, Laurence A. 2015. The JAK-STAT pathway: impact on human disease and therapeutic intervention. *Annu Rev Med*. **66**:311-28. doi: 10.1146/annurev-med-051113-024537.

Reck-Peterson SL, Redwine WB, Vale RD, Carter AP. 2018. The cytoplasmic dynein transport machinery and its many cargoes. *Nature Reviews Molecular Cell Biology* **19**:382–398. doi:10.1038/s41580-018-0004-3

Schneider WM, Chevillotte MD, Rice CM. 2014. Interferon-stimulated genes: a complex web of host defenses. *Annu Rev Immunol*. **32**:513-45. doi: 10.1146/annurev-immunol-032713-120231.

Stringer C. The origin and evolution of Homo sapiens. 2016. *Philos Trans R Soc Lond B Biol Sci*. **371**(1698):20150237. doi: 10.1098/rstb.2015.0237.

Sun D, Chen S, Cheng A, Wang M. 2016. Roles of the Picornaviral 3C Proteinase in the Viral Life Cycle and Host Cells. *Viruses*. **8**(3):82. doi: 10.3390/v8030082.

Thompson MR, Kaminski JJ, Kurt-Jones EA, Fitzgerald KA. 2011. Pattern recognition receptors and the innate immune response to viral infection. *Viruses*. **3**(6):920-40. doi: 10.3390/v3060920.

Tsu BV, Fay EJ, Nguyen KT, Corley MR, Hosuru B, Dominguez VA, Daugherty MD. 2021. Running With Scissors: Evolutionary Conflicts Between Viral Proteases and the Host Immune System. *Front Immunol*. **12**:769543. doi: 10.3389/fimmu.2021.769543.

Chapter 2: Diverse Viral Proteases Activate the NLRP1 Inflammasome

Abstract

The NLRP1 inflammasome is a multiprotein complex that is a potent activator of inflammation. Mouse NLRP1B can be activated through proteolytic cleavage by the bacterial Lethal Toxin (LeTx) protease, resulting in degradation of the N-terminal domains of NLRP1B and liberation of the bioactive C-terminal domain, which includes the caspase activation and recruitment domain (CARD). However, natural pathogen-derived effectors that can activate human NLRP1 have remained unknown. Here, we use an evolutionary model to identify several proteases from diverse picornaviruses that cleave human NLRP1 within a rapidly evolving region of the protein, leading to host-specific and virus-specific activation of the NLRP1 inflammasome. Our work demonstrates that NLRP1 acts as a 'tripwire' to recognize the enzymatic function of a wide range of viral proteases and suggests that host mimicry of viral polyprotein cleavage sites can be an evolutionary strategy to activate a robust inflammatory immune response.

Introduction

The ability to sense and respond to pathogens is central to the mammalian immune system. However, immune activation needs to be properly calibrated, as an overactive immune response can at times be as pathogenic as the pathogen itself. To ensure accurate discrimination of self and non-self, innate immune sensors detect broadly conserved microbial molecules such as bacterial flagellin or double-stranded RNA (Janeway, 1989). However, such microbial patterns can be found on harmless and pathogenic microbes alike. More recently, pathogen-specific activities such as toxins or effector enzymes have also been shown to be targets of innate immune recognition (Jones et al., 2016; Mitchell et al., 2019; Vance et al., 2009). Such a system

18

for detection, termed effector-trigged immunity (ETI), has been well-established in plants (Cui et al., 2015; Jones et al., 2016) and is emerging as an important means to allow the immune system to distinguish pathogens from harmless microbes in animals (Fischer et al., 2020; Jones et al., 2016).

Complicating the success of host detection systems, innate immune sensors are under constant selective pressure to adapt due to pathogen evasion or antagonism of immune detection. Such evolutionary dynamics, termed host-pathogen arms races, result from genetic conflicts where both host and pathogen are continually driven to adapt to maintain a fitness advantage. The antagonistic nature of these conflicts can be distinguished via signatures of rapid molecular evolution at the exact sites where host and pathogen interact (Daugherty and Malik, 2012; Meyerson and Sawyer, 2011; Sironi et al., 2015). Consistent with their role as the first line of cellular defense against incoming pathogens, innate immune sensors of both broad molecular patterns as well as specific pathogen-associated effectors have been shown to be engaged in genetic conflicts with pathogens (Cagliani et al., 2014; Chavarría-Smith et al., 2016; Hancks et al., 2015; Tenthorey et al., 2014; Tian et al., 2009).

Inflammasomes are one such group of rapidly evolving cytosolic immune sensor complexes (Broz and Dixit, 2016; Chavarría-Smith et al., 2016; Evavold and Kagan, 2019; Rathinam and Fitzgerald, 2016; Tenthorey et al., 2014; Tian et al., 2009). Upon detection of microbial molecules or pathogen-encoded activities, inflammasome-forming sensor proteins serve as a platform for the recruitment and activation of proinflammatory caspases including caspase-1 (CASP1) through either a pyrin domain (PYD) or a caspase activation and recruitment domain (CARD) (Broz and Dixit, 2016; Rathinam and Fitzgerald, 2016). Active CASP1 mediates the maturation and release of the proinflammatory cytokines interleukin (IL)−1β and

19

IL-18 (Broz and Dixit, 2016; Rathinam et al., 2012). CASP1 also initiates a form of cell death known as pyroptosis (Broz and Dixit, 2016; Rathinam et al., 2012). Together, these outputs provide robust defense against a wide array of eukaryotic, bacterial, and viral pathogens (Broz and Dixit, 2016; Evavold and Kagan, 2019; Rathinam and Fitzgerald, 2016).

The first described inflammasome is scaffolded by the sensor protein NLRP1, a member of the nucleotide-binding domain (NBD), leucine-rich repeat (LRR)-containing (NLR) superfamily (Martinon et al., 2002; Ting et al., 2008). NLRP1 has an unusual domain architecture, containing a CARD at its C-terminus rather than the N-terminus like all other inflammasome sensor NLRs, and a function-to-find domain (FIIND), which is located between the LRRs and CARD (Ting et al., 2008). The FIIND undergoes a constitutive self-cleavage event, such that NLRP1 exists in its non-activated state as two, noncovalently associated polypeptides (D'Osualdo et al., 2011; Finger et al., 2012; Frew et al., 2012), the N-terminal domains and the C-terminal CARD-containing fragment.

The importance of the unusual domain architecture of NLRP1 for mounting a pathogen-specific inflammasome response has been elucidated over the last several decades (Evavold and Kagan, 2019; Mitchell et al., 2019; Taabazuing et al., 2020). The first hint that NLRP1 does not detect broadly conserved microbial molecules came from the discovery that the Bacillus anthracis Lethal Toxin (LeTx) is required to elicit a protective inflammatory response against B. anthracis infection via one of the mouse NLRP1 homologs, NLRP1B (Boyden and Dietrich, 2006; Greaney et al., 2020; Moayeri et al., 2010; Terra et al., 2010). Paradoxically, inflammasome activation is the result of site-specific cleavage in the N-terminus of mouse NLRP1B by the Lethal Factor (LF) protease subunit of LeTx, indicating that protease-mediated cleavage of NLRP1 does not disable its function but instead results in its activation (Chavarría-

Smith and Vance, 2013; Levinsohn et al., 2012). More recently, the mechanism by which LF-mediated proteolytic cleavage results in direct NLRP1B inflammasome activation has been detailed (Chui et al., 2019; Sandstrom et al., 2019). These studies revealed that proteolysis of mouse NLRP1B by LF results in exposure of a novel N-terminus, which is then targeted for proteasomal degradation by a protein quality control mechanism called the 'N-end rule' pathway (Chui et al., 2019; Sandstrom et al., 2019; Wickliffe et al., 2008; Xu et al., 2019). Since the proteasome is a processive protease, it progressively degrades the N-terminal domains of NLRP1B but is disengaged upon arriving at the self-cleavage site within the FIIND domain. Degradation of the N-terminal domains thus releases the bioactive C-terminal CARD-containing fragment of NLRP1B from its non-covalent association with the N-terminal domains, which is sufficient to initiate downstream inflammasome activation (Chui et al., 2019; Sandstrom et al., 2019). By directly coupling NLRP1 inflammasome activation to cleavage by a pathogen-encoded protease, NLRP1 can directly sense and respond to the activity of a pathogen effector. Such a model indicates that the N-terminal domains are not required for NLRP1 activation per se, but rather serve a pathogen-sensing function. Interestingly, the N-terminal 'linker' region in mouse NLRP1B that is cleaved by LF is rapidly evolving in rodents, and the analogous linker region is likewise rapidly evolving in primate species (Chavarría-Smith et al., 2016). These data suggest that selection from pathogens has been driving diversification of this protease target region of NLRP1, possibly serving to bait diverse pathogenic proteases into cleaving NLRP1 and activating the inflammasome responses.

Consistent with the rapid evolution in NLRP1 at the site of proteolytic cleavage, LF neither cleaves nor activates human NLRP1 (Mitchell et al., 2019; Moayeri et al., 2012; Taabazuing et al., 2020). Despite this, human NLRP1 can also be activated by proteolysis when

a tobacco etch virus (TEV) protease site is engineered into the rapidly evolving linker region of human NLRP1 that is analogous to the site of LF cleavage in mouse NLRP1B (Chavarría-Smith et al., 2016). Thus, like mouse NLRP1B, it has been predicted that human NLRP1 may serve as a 'tripwire' sensor for pathogen-encoded proteases (Mitchell et al., 2019).

Here, we investigate the hypothesis that viral proteases cleave and activate human NLRP1. We reasoned that human viruses, many of which encode proteases as necessary enzymes for their replication cycle, may be triggers for NLRP1 activation. To pursue this hypothesis, we focused on viruses in the Picornaviridae family, which encompass a diverse set of human enteric and respiratory pathogens including coxsackieviruses, polioviruses, and rhinoviruses (Zell, 2018). These viruses all translate their genome as a single polyprotein, which is then cleaved into mature proteins in at least six sites in a sequence-specific manner by a virally encoded 3C protease, termed 3Cpro (Laitinen et al., 2016; Solomon et al., 2010; Sun et al., 2016; Zell, 2018). 3Cpro is also known to proteolytically target numerous host factors, many of which are associated with immune modulation (Croft et al., 2018; Huang et al., 2015; Lei et al., 2017; Mukherjee et al., 2011; Qian et al., 2017; Wang et al., 2019; Wang et al., 2012; Wang et al., 2014; Wang et al., 2015; Wen et al., 2019; Xiang et al., 2014; Xiang et al., 2016; Zaragoza et al., 2006). Because 3Cpro are evolutionarily constrained to cleave several specific polyprotein sites and host targets for replicative success, we reasoned that human NLRP1 may have evolved to sense viral infection by mimicking viral polyprotein cleavage sites, leading to NLRP1 cleavage and inflammasome activation. Using an evolution-guided approach, we now show that NLRP1 is cleaved in its rapidly evolving linker region by several 3Cpro from picornaviruses, resulting in inflammasome activation. These results are consistent with the recent discovery that human rhinovirus (HRV) 3Cpro cleaves and activates NLRP1 in airway epithelia (Robinson et al.,

22

2020). We also find that variation in the cleavage site among primates, and even within the human population, leads to changes in cleavage susceptibility and inflammasome activation. Interestingly, we observe that proteases from multiple genera of viruses cleave and activate human NLRP1 and mouse NLRP1B at different sites, supporting a role for an evolutionary conflict between viral proteases and NLRP1. Taken together, our work highlights the role of NLRP1 in sensing and responding to diverse viral proteases by evolving cleavage motifs that mimic natural sites of proteolytic cleavage in the viral polyprotein.

Results

Human NLRP1 contains mimics of viral protease cleavage sites

Our hypothesis that NLRP1 can sense viral proteases is based on two prior observations. First, both human NLRP1 and mouse NLRP1B can be activated by N-terminal proteolysis (Chavarría-Smith et al., 2016). Second, the linker in primate NLRP1, which is analogous to the N-terminal disordered region of NLRP1B that is cleaved by LF protease, has undergone recurrent positive selection (Chavarría-Smith et al., 2016), or an excess of non-synonymous amino acid substitutions over what would be expected by neutral evolution (Kimura, 1983). We reasoned that this rapid protein sequence evolution may reflect a history of pathogen-driven selection, wherein primate NLRP1 has evolved to sense pathogen-encoded proteases such as those encoded by picornaviruses. To test this hypothesis, we first generated a predictive model for 3Cpro cleavage site specificity. We chose to focus on the enterovirus genus of picornaviruses, as there is a deep and diverse collection of publicly available viral sequences within this genus due to their importance as human pathogens including coxsackieviruses, polioviruses, enterovirus D68, and HRV (Blom et al., 1996; Pickett et al., 2012). We first

compiled complete enterovirus polyprotein sequences from the Viral Pathogen Resource (ViPR)

database (Pickett et al., 2012) and extracted and concatenated sequences for each of the cleavage

sites within the polyproteins (Figure 2.1A and B, Supplementary files 2.1 and 2.2). After

removing redundant sequences, we used the MEME Suite (Bailey et al., 2009) to create the

following 3Cpro cleavage motif: [A/Φ]XXQGXXX (where Φ denotes a hydrophobic residue and

X denotes any amino acid), which is broadly consistent with previous studies that have

experimentally profiled the substrate specificity of enterovirus 3Cpros (Blom et al., 1996; Fan et

al., 2020; Jagdeo et al., 2018; O'Donoghue et al., 2012; Figure 2.1C).
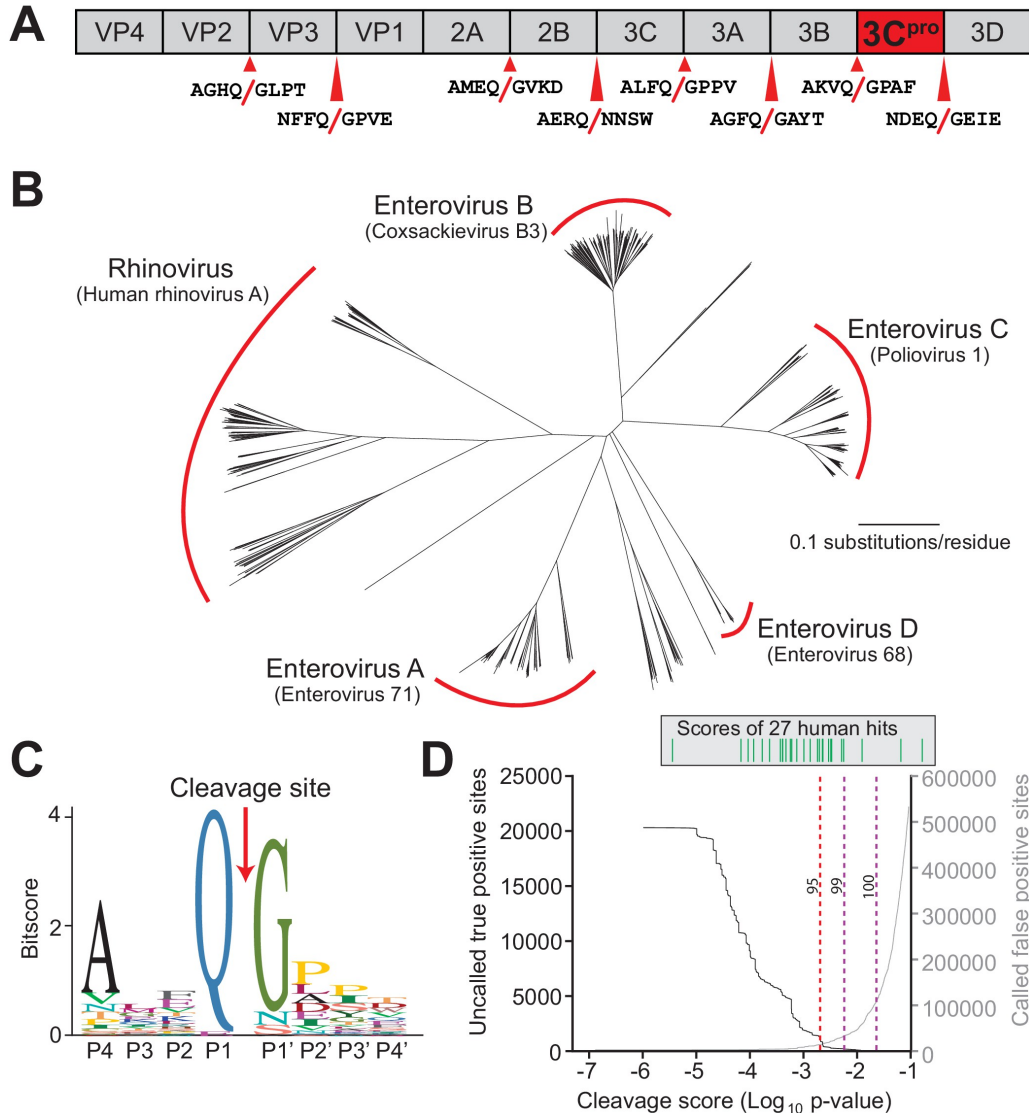
Figure 2.1. Conserved polyprotein cleavage sites across enteroviruses inform substrate specificity of the enteroviral 3Cpro. (A) Schematic of 3Cpro cleavage sites (red arrows) within the polyprotein of coxsackievirus B3 Nancy (CVB3), a model enterovirus. Shown are the eight amino acids flanking each cleavage site within the polyprotein. (B) Phylogenetic tree of 796 enteroviral polyprotein coding sequences depicting the major clades of enteroviruses sampled in this study with representative viruses from each clade in parentheses (Supplementary file 2.2). (C) Eight amino acid polyprotein cleavage motif for enteroviruses (labeled as positions P4 to P4') generated from the 796 enteroviral polyprotein sequences in (B) using the MEME Suite (Supplementary file 1.2). (D) Training set data used to determine the motif search threshold for FIMO (Supplementary files 2.1, 2.3 and 2.4). The X-axis represents a log10 of the p-value reported by FIMO as an indicator for the strength of the cleavage motif hit (cleavage score). (Left) The Y-axis depicts the number of uncalled true positives, or motif hits that overlap with the initial set of 8mer polyprotein cleavage sites used to generate the motif, in the training set of enteroviral polyprotein sequences (black). (Right) The Y-axis depicts the number of called false positive sites, or any motif hits found in the polyprotein that are not known to be cleaved by 3Cpro, in the training set of enteroviral polyprotein sequences (gray). (Above) Each line depicts a single, experimentally validated case of enteroviral 3Cpro cleavage site within a human protein as reported in Laitinen et al., 2016 and is ordered along the X-axis by its resulting cleavage score. A vertical dotted line is used to represent the decided threshold that captures 95% of true positive hits and 16 out of 27 reported human hits (Figure 2.2).
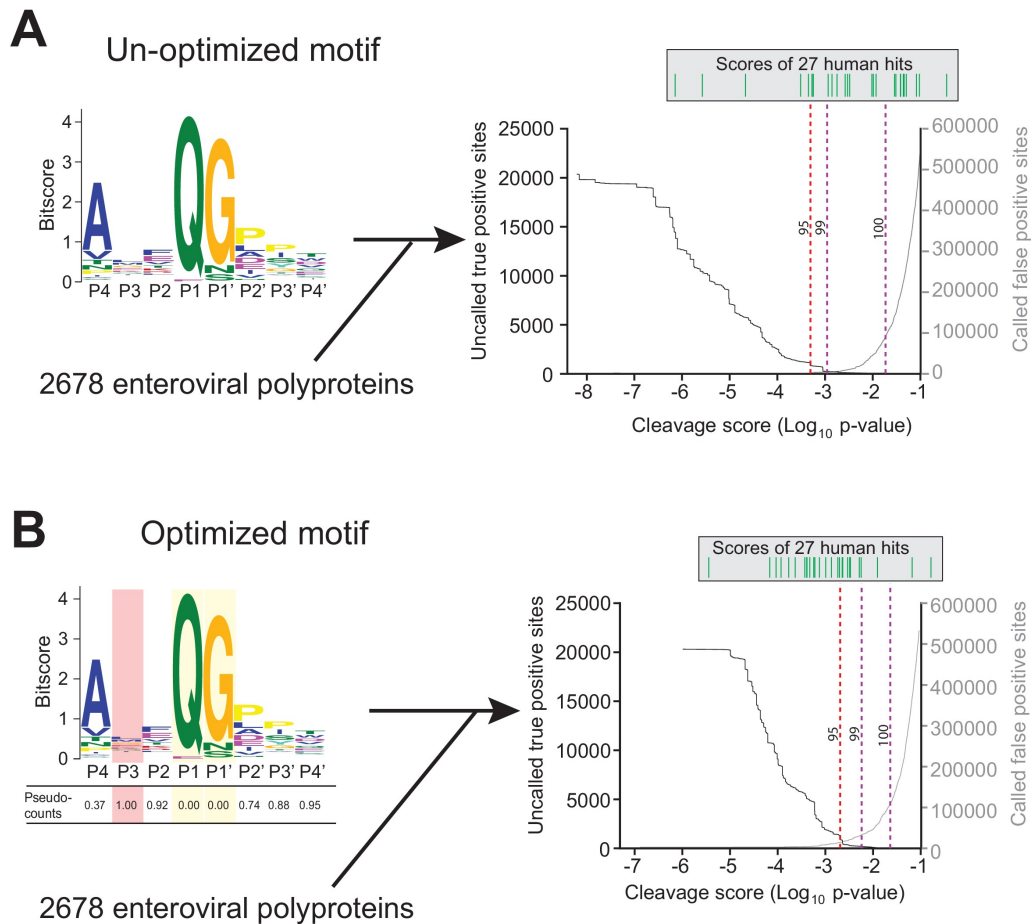
Figure 2.2. Motif optimization enhances capture of known human targets of enteroviral 3Cpro. (A) As described in Figure 2.1B and C and Materials and Methods, the 8mer (P4–P4') 3Cpro polyprotein cleavage motif was initially generated from unique, concatenated 8mer cleavage sites across 796 enteroviral polyprotein sequences. To assess the capture capability of the motif on both virus and host targets, the motif was then used to conduct a low threshold (p-value=0.1) FIMO (MEME Suite) search across training set of 2678 nonredundant enteroviral polyproteins from ViPR and 27 experimentally validated human targets of 3Cpro (Laitinen et al., 2016). In the graph, the X-axis represents a log10 of the p-value reported by FIMO as an indicator for the strength of the cleavage motif hit, or cleavage score. The left Y-axis depicts the number of uncalled 'true positives', or motif hits within the enteroviral polyprotein training set that overlap with the initial set of 8mer polyprotein cleavage sites used to generate the motif (black). The right Y-axis depicts the number of called false positive sites, or any motif hits that are not true positives, in the training set of enteroviral polyprotein sequences (gray). (Above) Each line depicts a single, experimentally validated case of enteroviral 3Cpro cleavage site within a human protein as reported in Laitinen et al., 2016 and is ordered along the x-axis by its corresponding cleavage score. Vertical dotted lines are used to represent the decided thresholds for comparison of capture capability. Capture of human targets at 95%, 99%, or 100% capture of true positives in the polyprotein dataset corresponds to capture of 4, 7, and 16 human hits. (B) Pseudo-counts to the position-specific scoring matrix of the motif shown in (A) were adjusted by total information content where the two most information-dense positions P1 and P1' are assigned pseudocount = 0 and the least information-dense position P3 pseudocount = 1, and the remaining positions are assigned a pseudocount value relative to the most information-dense position P1. This optimized motif is then used to FIMO search against the same training set as described in (A). Capture of human targets at 95%, 99%, or 100% capture of true positives in the polyprotein dataset corresponds to capture of 16, 23, and 24 human hits.

We next optimized our 3Cpro cleavage site motif prediction by querying against predicted viral polyprotein and experimentally validated host cleavage sites (Laitinen et al., 2016), allowing us to set thresholds for predicting new cleavage sites (Supplementary files 2.3 and 2.4). Due to the low-information content of the polyprotein motif (Figure 2.1C), such predictions are necessarily a compromise between stringency and capturing the most known cleavage sites. In particular, we wished to make sure that the model was able to capture a majority of experimentally validated human hits (compiled in Laitinen et al., 2016) in addition to the known sites of polyprotein cleavage ('true positives'), while minimizing the prediction of sites outside of known polyprotein cleavage sites ('false positives'). By adjusting the model to allow greater flexibility for amino acids not sampled in the viral polyprotein (see Materials and methods and Figure 2.2 and Supplementary file 2.4), we were able to capture 95% of known viral sites and the majority of the known human hits, while limiting the number of false negative hits within the viral polyprotein (Figure 2.1D).

The coxsackievirus B3 3Cpro cleaves human NLRP1 at a predicted site within the linker region

We next used our refined model to conduct a motif search for 3Cpro cleavage sites in NLRP1 using Find Individual Motif Occurrences (FIMO) (Grant et al., 2011). We identified three occurrences of the motif across the full-length human NLRP1 protein (Figure 2.3A). Of these sites, one in particular, 127-GCTQGSER-134, fell within the previously described rapidly evolving linker (Chavarría-Smith et al., 2016) and demonstrates the lowest percent conservation across mammalian species at each of the predicted P4-P4' positions (Figure 2.3B).
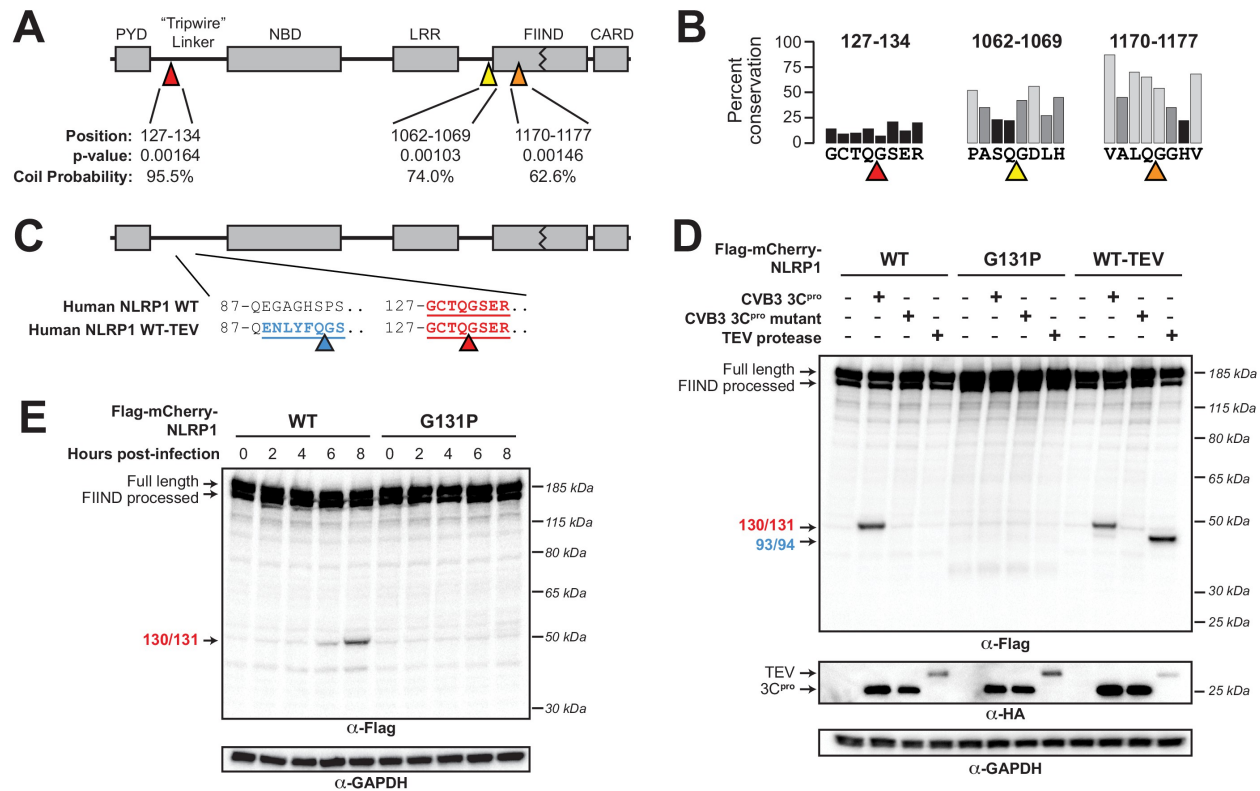
Figure 2.3. Enterovirus 3Cpro cleaves human NLRP1 at the predicted site of mimicry. (A) Schematic of the domain structure of NLRP1, with predicted cleavage sites (triangles). FIMO-reported p-values and average NetsurfP-reported coil probabilities are described at the predicted sites. (B) Percent conservation across 100 mammalian species at each position of each predicted 8mer cleavage site within human NLRP1. (C) Schematic of the human NLRP1 sequence used to assess enteroviral cleavage and activation. The predicted enteroviral cleavage site found in the linker region (127-GCTQGSER-134) is shown in red. Human NLRP1 WT-TEV contains an engineered TEV cleavage site between residues 93 and 94 (underlined green) in human NLRP1 WT. (D) Immunoblot depicting human NLRP1 cleavage by CVB3 3Cpro and TEV protease. HEK293T cells were co-transfected using 100 ng of the indicated Flag-tagged mCherry-NLRP1 fusion plasmid constructs with 250 ng of the indicated protease construct and immunoblotted with the indicated antibodies. (E) Immunoblot depicting human NLRP1 cleavage at the indicated timepoints after infection with 250,000 PFU (MOI = ~1) CVB3. HEK293T cells were transfected using 100 ng of either WT NLRP1 or NLRP1 G131P and infected 24–30 hr later. All samples were harvested 32 hr post-transfection and immunoblotted with the indicated antibodies.

To assess if human NLRP1 is cleaved by enteroviral 3Cpro, we co-expressed a N-terminal mCherry-tagged wild-type (WT) human NLRP1 with the 3Cpro from the model enterovirus, coxsackievirus B3 (CVB3) in HEK293T cells (Figure 2.3C). The mCherry tag stabilizes and allows visualization of putative N-terminal cleavage products, similar to prior studies (Chavarría-Smith et al., 2016). We observed that the WT but not catalytically inactive (C147A) CVB3 3Cpro cleaved NLRP1, resulting in a cleavage product with a molecular weight

consistent with our predicted 3Cpro cleavage at the predicted 127-GCTQGSER-134 site (44

kDa) (Figure 2.3D). Based on the presence of a single cleavage product, we assume that the

other predicted sites are either poor substrates for 3Cpro or less accessible to the protease as

would be predicted from their NetSurfP-reported (Klausen et al., 2019) coil probability within

structured domains of the protein (Figure 2.3A). To determine if the cleavage occurs between

residues 130 and 131, we mutated the P1' glycine to a proline (G131P), which abolished 3Cpro

cleavage of NLRP1 (Figure 2.3D). CVB3 3Cpro cleavage of NLRP1 resulted in a similarly

intense cleavage product when compared to the previously described system in which a TEV

protease site was introduced into the linker region of NLRP1 (Chavarría-Smith et al., 2016;

Figure 2.3D). Taken together, these results indicate that cleavage of WT NLRP1 by a protease

from a natural human pathogen is robust and specific.

　　　During a viral infection, 3Cpro is generated in the host cell cytoplasm after translation of

the viral mRNA to the polyprotein and subsequent processing of the viral polyprotein into

constituent pieces (Laitinen et al., 2016). To confirm that virally-produced 3Cpro, or the 3 CD

precursor that can also carry out proteolytic cleavage during infection (Laitinen et al., 2016), is

able to cleave NLRP1, we virally infected cells expressing either WT NLRP1 or the uncleavable

(G131P) mutant. We observed accumulation of the expected cleavage product beginning at 6 hr

post-infection when we infected cells expressing WT NLRP1 and no cleavage product when we

infected cells expressing the 131P mutant (Figure 2.3E). These results validate that CVB3

infection can result in rapid and specific cleavage of human NLRP1.

The CVB3 3Cpro activates human NLRP1 by cleaving within the linker region

Previous results with a TEV-cleavable human NLRP1 showed that cleavage by TEV protease was sufficient to activate the human NLRP1 inflammasome in a reconstituted inflammasome assay (Chavarría-Smith et al., 2016). Using the same assay, in which plasmids-encoding human NLRP1, CASP1, ASC, and IL-1β are transfected into HEK293T cells, we tested if the CVB3 3Cpro activates the NLRP1 inflammasome. We observed that the CVB3 3Cpro results in robust NLRP1 inflammasome activation, as measured by CASP1-dependent processing of pro-IL-1β to the active p17 form (Figure 2.4A). As expected, CVB3 3Cpro activation of the NLRP1 inflammasome was prevented by introduction of a mutation in the NLRP1 FIIND (S1213A) (D'Osualdo et al., 2011; Finger et al., 2012; Frew et al., 2012; Figure 2.5 – panel A), which prevents FIIND auto-processing and the release of the bioactive C-terminal UPA–CARD (Chui et al., 2019; Sandstrom et al., 2019). Consistent with recent results (Robinson et al., 2020), we also observed that chemical inhibitors of the proteasome (MG132) or the Cullin-RING E3 ubiquitin ligases that are required for the degradation of proteins with a novel N-terminal glycine (MLN4924) (Timms et al., 2019), also blocked CVB3 3Cpro activation of NLRP1 (Figure 2.5 – panel B). To confirm that 3Cpro-induced inflammasome activation resulted in release of bioactive IL-1β from cells, we measured active IL-1β levels in the culture supernatant using cells engineered to express a reporter gene in response to soluble, active IL-1β. When compared to a standard curve (Figure 2.6), we found that 3Cpro treatment resulted in release of >4 ng/ml of active IL-1β into the culture supernatant (Figure 2.4B). Importantly, in both western blot and cell culture assays, 3Cpro-induced inflammasome activation was comparable to TEV-induced activation and was ablated when position 131 was mutated, validating that CVB3 3Cpro cleavage at a single site is both necessary and sufficient to activate NLRP1 (Figure 2.4A and B). Taken together, our results are consistent with CVB3 3Cpro

activating the NLRP1 inflammasome via site-specific cleavage and subsequent 'functional degradation' (Chui et al., 2019; Sandstrom et al., 2019).
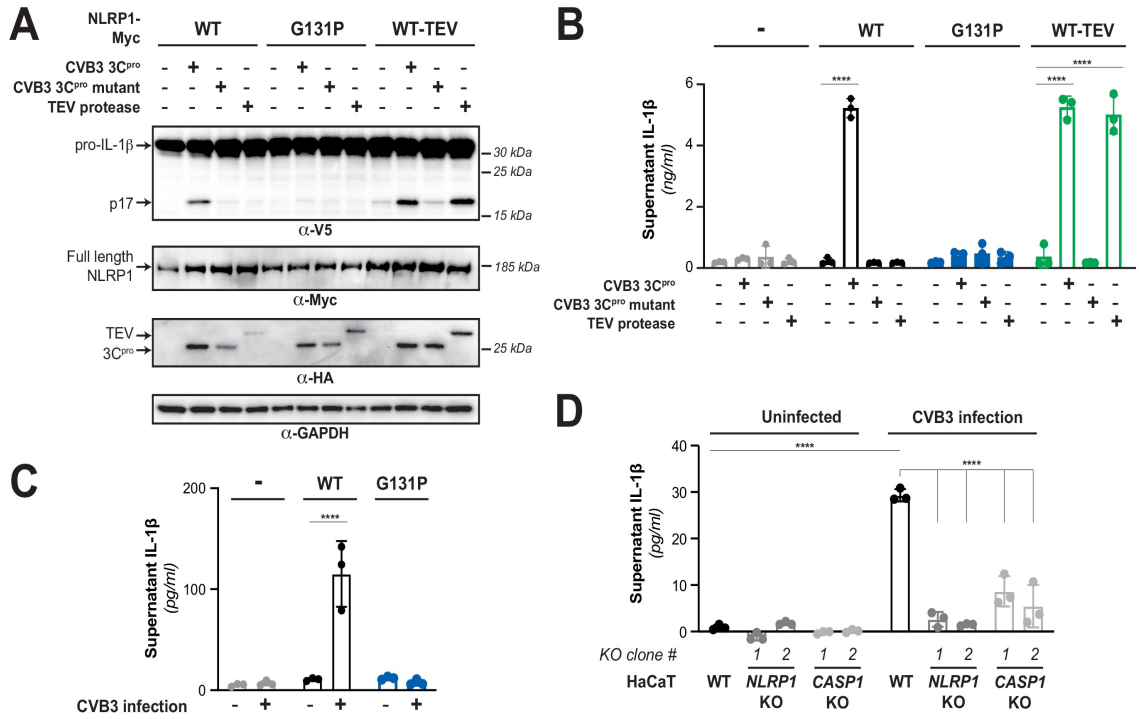
Figure 2.4. Enterovirus 3Cpro cleavage of human NLRP1 promotes pro-inflammatory cytokine release. (A) Immunoblot depicting human NLRP1 activation (maturation of IL-1β) by CVB3 3Cpro and TEV protease. HEK293T cells were co-transfected using 100 ng of the indicated protease, 50 ng V5-IL-1β, 100 ng CASP1, 5 ng ASC, and 4 ng of the indicated Myc-tagged NLRP1, and immunoblotted with the indicated antibodies. Appearance of the mature p17 band of IL-1β indicates successful assembly of the NLRP1 inflammasome and activation of CASP1. (B) Bioactive IL-1β in the culture supernatant was measured using HEK-Blue IL-1β reporter cells, which express secreted embryonic alkaline phosphatase (SEAP) in response to extracellular IL-1β. Supernatant from cells transfected as in (A) was added to HEK-Blue IL-1β reporter cells and SEAP levels in the culture supernatant from HEK-Blue IL-1β reporter cells were quantified by the QUANTI-Blue colorimetric substrate. Transfections were performed in triplicate and compared to the standard curve generated from concurrent treatment of HEK-Blue IL-1β reporter cells with purified human IL-1β (Figure 2.6). Data were analyzed using two-way ANOVA with Sidak's post-test. **** = $p < 0.0001$. (C) CVB3 infection of inflammasome-reconstituted HEK293T cells results in IL-1β release when NLRP1 can be cleaved by 3Cpro. Cells were transfected with the indicated NLRP1 construct and other NLRP1 inflammasome components as in (B). Sixteen hours post-transfection, cells were mock infected or infected with 250,000 PFU (MOI = ~1) CVB3. Eight hours post-infection, culture supernatant was collected and bioactive IL-1β was measured as in (B). (D) CVB3 infection of an immortalized human keratinocyte cell line, HaCaT, activates the NLRP1 inflammasome. WT or knockout (Figure 2.7) HaCaT cell lines were mock infected or infected with 100,000 PFU (MOI = ~0.4) CVB3. Forty-eight hours post-infection, culture supernatant was collected and bioactive IL-1β was measured as in (B).
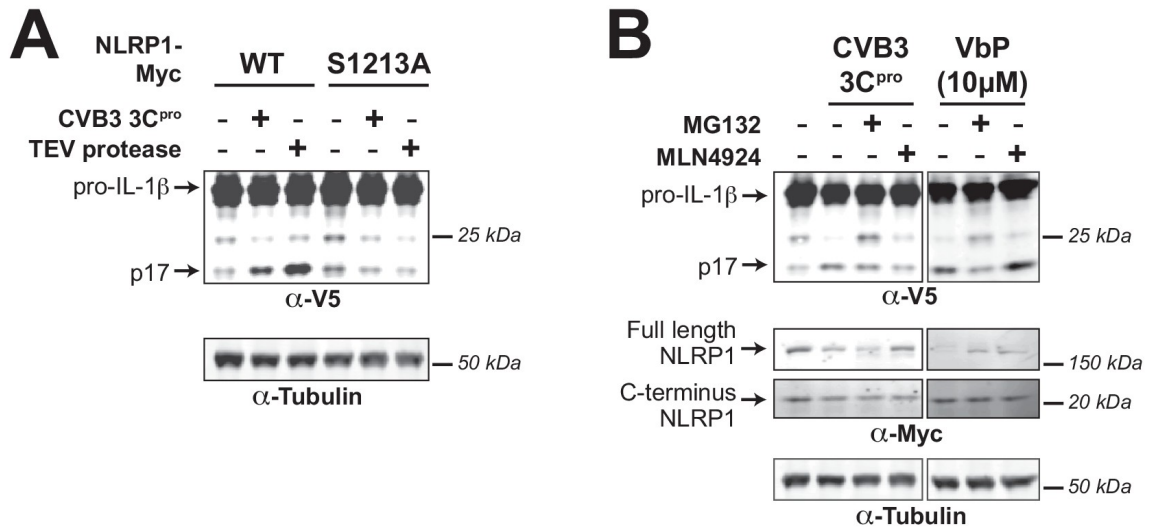
Figure 2.5. 3Cpro-mediated activation of the human NLRP1 inflammasome depends on FIIND autoprocessing and proteosomal degradation. (A) HEK293T cells were transfected with either WT NLRP1 or a FIIND auto-processed defective mutant (S1213A) along with other components of the NLRP1 inflammasome (CASP1, ASC, and IL-1β) as in Figure 2.4A. Only cells transfected with WT NLRP1 can produce mature IL-1β upon co-transfection with CVB3 3Cpro or TEV protease as indicated by the appearance of the p17 band. (B) HEK293T cells were transfected as in (A), and then treated with the indicated inhibitors of proteasomal-mediated degradation (0.5 µM MG132) or the N-glycine degron pathway (1.0 µM MLN4924) for 6 hr prior to harvest. Addition of 10 µM VbP, an inhibitor of the NLRP1 inhibitors DPP8/9 (Okondo et al., 2018), was used as a control for protease-independent activation of the inflammasome and is thus unaffected by MLN4924.
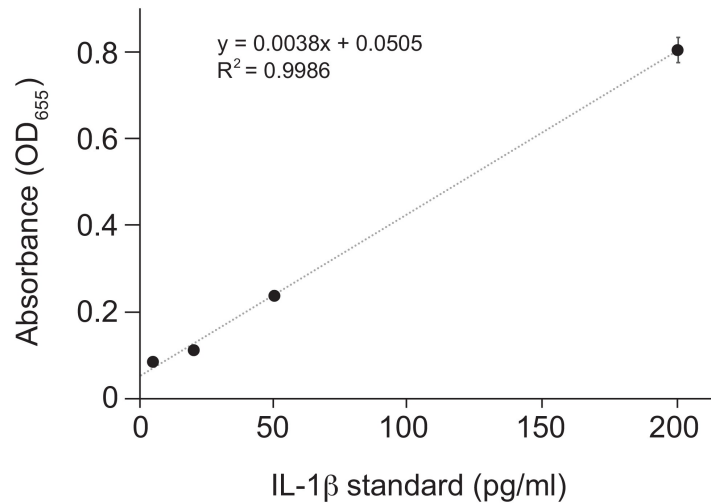
Figure 2.6. Standard curve for Figure 2.4B. Purified human IL-1β was added in duplicate to the indicated final concentration to HEK-Blue IL-1β reporter cells and SEAP activity was measured by increased absorbance at OD655. The indicated linear fit was used to calculate absolute concentrations of bioactive IL-1β from culture supernatants shown in Figure 2.4B. Note that supernatants from inflammasome-transfected cells was diluted 10-fold before addition to HEK-Blue IL-1β reporter cells to ensure that levels fell within the linear range of the indicated standard curve. Standard curves were generated in an identical manner for each panel of HEK-Blue data shown.

A *NLRP1* Knockouts   **B** *CASP1* Knockouts

NLRP1 exon 5

                          sgRNA   PAM
NLRP1 WT   C T C C A C T G C T T G T A C G A G A C T C G G A A C

NLRP1
KO clone #1   C T C C A C T G C T T G T A C G A G – – – – – G A A C
              G A G G T G A C G A A C A T G C T C – – – – – C T T G

NLRP1 exon 2

              PAM   sgRNA
NLRP1 WT   A G G C C A C T C T – C C C T C A T T C C C C T A C A

NLRP1
KO clone #2   A G G C C A C T C T T C C C T C A T T C C C C T A C A
              T C C G G T G A G A A G G G A G T A A G G G G A T G T

CASP1 intron1/exon 2

                          sgRNA   PAM
CASP1 WT   T C C A A A C A G A C A A G G T C C T G A A G G A G A

CASP1
KO clone #1   T C C A A A C A G A C A A G G T C C – G A A G G A A A
              A G G T T T G T C T G T T C C A G G – C T T C C T T T

CASP1
KO clone #2   T C C A A A C A G A C A A G G A C C – – – – – G A G A
              A G G T T T G T C T G T T C C T G G – – – – – C T C T

Figure 2.7. Validation of CRISPR/Cas9-editing of NLRP1 or CASP1 in HaCaT cells by Sanger sequencing.
(A) The WT NLRP1 (exon 5 or exon 2) sequence is shown with CRISPR-targeting sgRNA and PAM sequences indicated. Below each WT sequence is shown the Sanger sequencing chromatogram and associated mutant sequence for each indicated clone. (B) Same as panel A, except indicating WT CASP1 intron 1/exon two sequence and sequencing data from two independently isolated knockout clones.

We next wished to test whether CVB3 infection, through the site-specific cleavage of NLRP1 by 3Cpro, can activate the NLRP1 inflammasome. Consistent with our prediction, recent work has revealed that HRV infection can cleave and activate human NLRP1 in airway epithelia (Robinson et al., 2020). However, prior work has also implicated a role for the NLRP3 inflammasome in enterovirus infection (Kuriakose and Kanneganti, 2019; Xiao et al., 2019), including activation of the NLRP3 inflammasome during CVB3 infection in mice and human cell lines (Wang et al., 2019; Wang et al., 2018). NLRP1 and NLRP3 have distinct expression patterns (Robinson et al., 2020; Zhong et al., 2016) including in epithelial cells, which are important targets of enterovirus infection. NLRP3 is activated in response to various noxious stimuli or damage signals associated with pathogen infection (Evavold and Kagan, 2019; Spel and Martinon, 2021). In contrast, NLRP1 is activated by direct proteolytic cleavage of its N-

terminal 'tripwire' region by viral proteases. We therefore wished to confirm that specific 3Cpro cleavage of NLRP1 during CVB3 infection is able to activate the NLRP1 inflammasome. We first virally infected 293 T cells, which do not express either NLRP1 or NLRP3, that were co-transfected with either WT NLRP1 or the uncleavable (G131P) mutant in our reconstituted inflammasome assay and measured active IL-1β in the culture supernatant. Eight hours after infection with CVB3, we observe robust release of active IL-1β into the culture supernatant when cells were transfected with WT NLRP1 but not the uncleavable mutant NLRP1 (Figure 2.4C). To test whether CVB3 infection can activate the inflammasome in an NLRP1-dependent fashion in cells that naturally express an intact NLRP1 inflammasome, we took advantage of the fact that NLRP1 has been described as the primary inflammasome in human keratinocytes (Zhong et al., 2016). We therefore infected WT, NLRP1, or CASP1 KO (Figure 2.7) immortalized HaCaT human keratinocytes with CVB3 and measured release of active IL-1β in the culture supernatant. Consistent with our model that CVB3 infection cleaves and activates the NLRP1 inflammasome, we observe a significant increase in supernatant IL-1β after CVB3 infection that is reduced in cells that lack either NLRP1 or CASP1 (Figure 2.4D). Together, these results indicate that CVB3 infection, through 3Cpro cleavage of the tripwire region of NLRP1, activates the NLRP1 inflammasome.

NLRP1 diversification across primates and within humans confers host differences in susceptibility to viral 3Cpro cleavage and inflammasome activation

Our evolutionary model in which NLRP1 is evolving in conflict with 3Cpro suggests that changes in the NLRP1 linker region, both among primates and within the human population (Figure 2.8A), would confer host-specific differences to NLRP1 cleavage and inflammasome activation. To test this hypothesis, we aligned the linker regions from NLRP1 from diverse

34

mammals and human population sampling and compared the sequences around the site of CVB3

3Cpro cleavage (Figure 2.8B and C and Figure 2.9). We noted that while a majority of primate

NLRP1s are predicted to be cleaved similarly to the human ortholog, several primate proteins

would be predicted to not be cleaved by enteroviral 3Cpro as a result of changes to either the P4,

P1 or P1' residues. To confirm these predictions, we made the human NLRP1 mutants G127E or

G131R, which reflect the Old World monkey or marmoset residues at each position,

respectively. As predicted, both primate NLRP1 variants prevented 3Cpro cleavage of NLRP1

(Figure 2.8D). These results indicate that multiple viral 3Cpro activate host NLRP1 in a host

specific manner and suggest that single changes within a short linear motif can substantially alter

cleavage susceptibility and inflammasome activation.
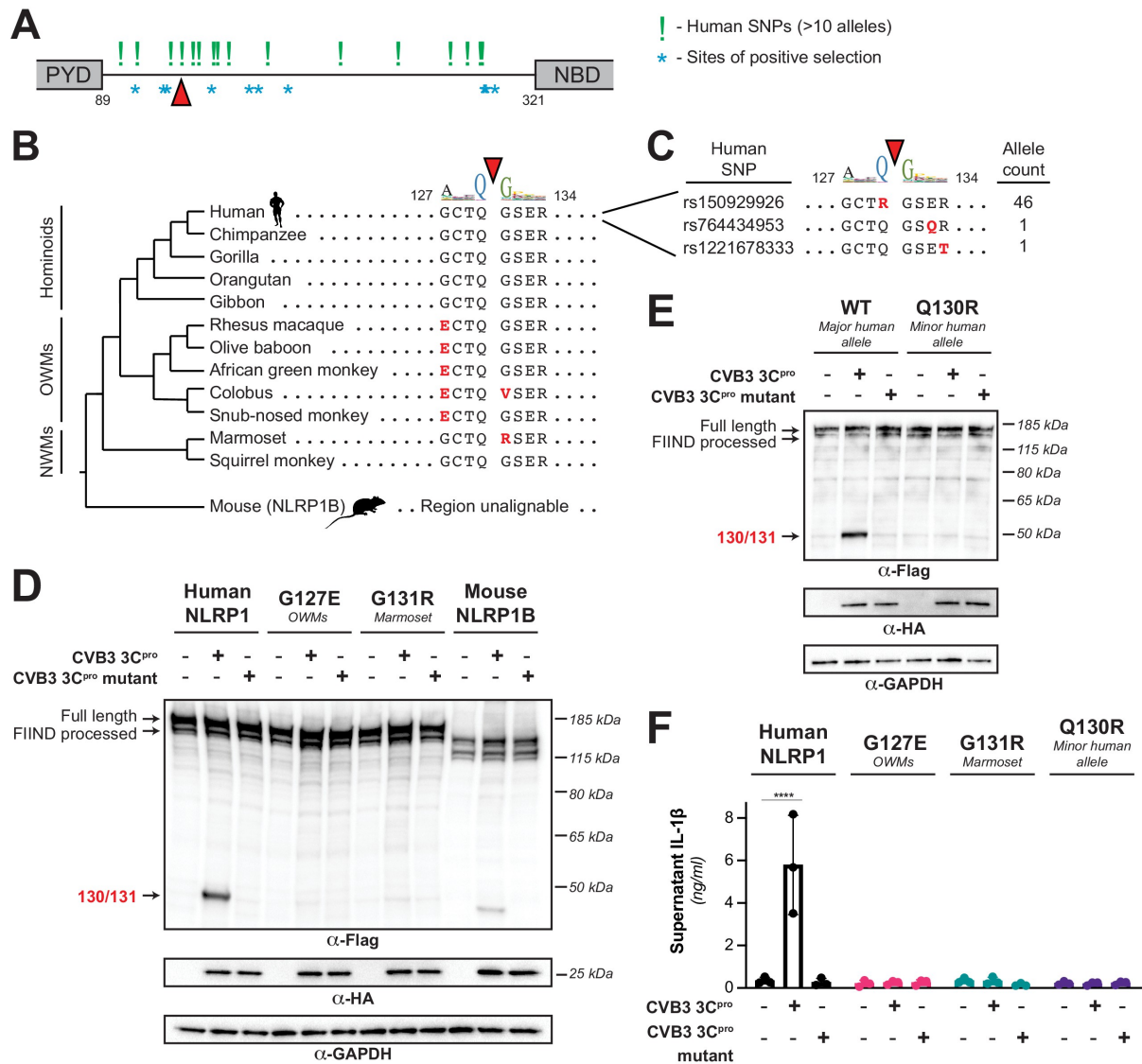
Figure 2.8. Naturally occurring cleavage site variants alter NLRP1 susceptibility to enteroviral 3Cpro. (A) Schematic of sites found to be evolving under positive selection (marked as *, from Chavarría-Smith and Vance, 2013) and human SNPs with at least 10 reported instances in the Genome Aggregation Database (GnomAD, Karczewski et al., 2020) (marked as !) within the linker region between the pyrin domain (PYD) and nucleotide binding domain (NBD) of NLRP1. The enteroviral 3Cpro cleavage site between position 130 and 131 is indicated by a red triangle. (B) Phylogenetic tree depicting the enteroviral 3Cpro cleavage site (red triangle) within NLRP1 across three clades of primates – hominoids, Old World monkeys (OWMs), and New World monkeys (NWMs). Mouse NLRP1B lacks any sequence that is alignable to this region of primate NLRP1 (see also Figure 2.9). Amino acid differences to the human NLRP1 reference sequence are highlighted in red. Above the alignment is the enterovirus 3Cpro sequence logo shown in Figure 2.1. (C) GnomAD-derived allele counts of each missense human SNP (by reference SNP #) within the 8mer of the determined enteroviral 3Cpro cleavage site. (D–E) Immunoblot depicting CVB3 3Cpro cleavage susceptibility of the indicated 8mer site variants introduced into human NLRP1 or full-length wild-type mouse NLRP1B (129 allele) (D) or the cleavage susceptibility of human NLRP1 Q130R, a naturally occurring human population variant (E). (F) Release of bioactive IL-1β into the culture supernatant was measured using HEK-Blue IL-1β reporter cells as in Figure 2.4B. Data were analyzed using two-way ANOVA with Sidak's post-test. **** = p<0.0001.

36
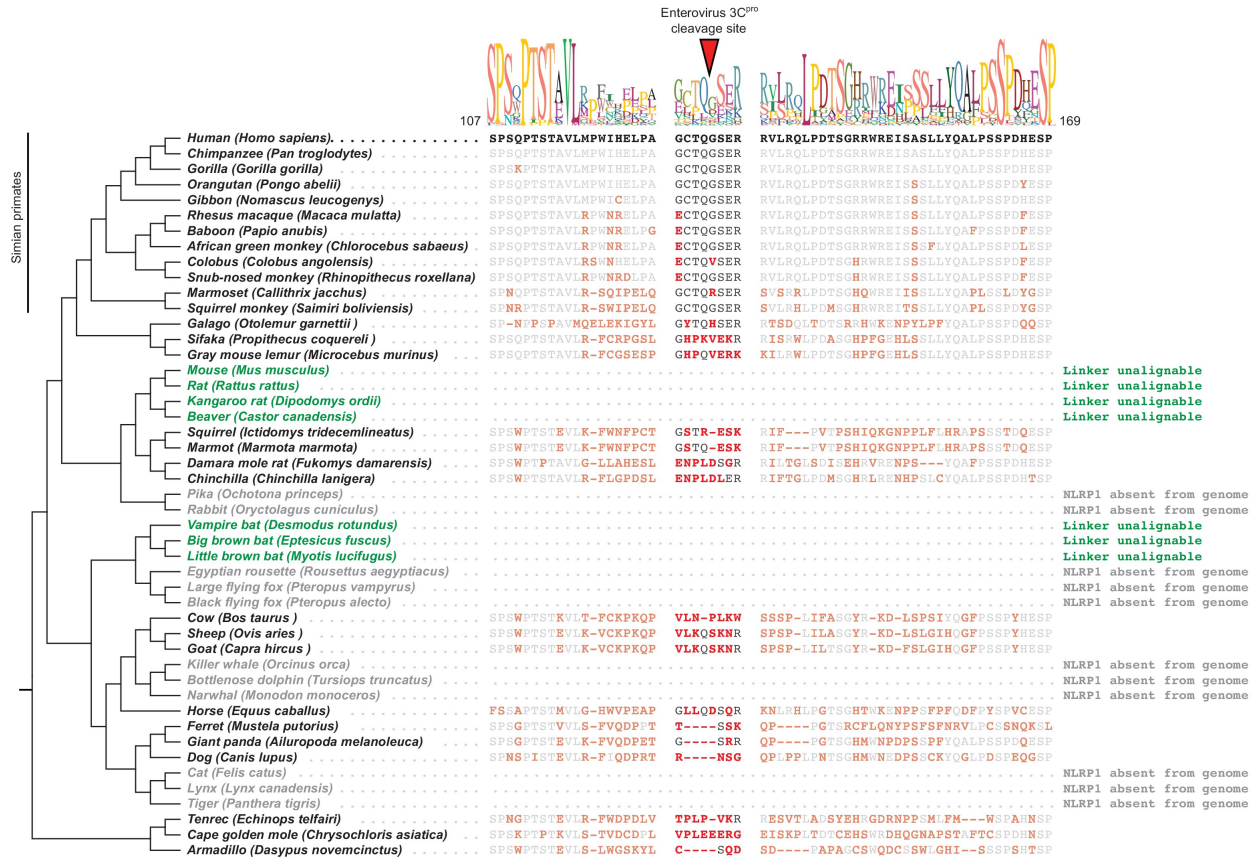
Figure 2.9. Mammalian NLRP1 phylogenomics and alignment of linker region. The indicated mammalian NLRP1 sequences were aligned and the region corresponding to residues 107–169 from human NLRP1 were extracted, which is anchored on both ends by well-conserved proline and serine-rich motifs. A consensus sequence generated from alignable sequences in this region is shown above the human sequence. The position of the CVB3 3Cpro cleavage site in human NLRP1 is shown, flanked by four amino acids on both sides (P4->P4'). In other mammals, residues that differ from the human sequence are shown in red. Within the aligned region that corresponds to the CVB3 3Cpro cleavage site, only simian primates have P4, P1 and P1' residues that would allow cleavage. The only other species that have a plausible cleavage site in this position are sheep and goats (P4 = Val, P1 = Gln, P1' = Ser), although those residues appear to have evolved independently at those positions. Two clades of species (the 'mouse-related' clade of rodents and the microbat clade, marked as green) have NLRP1 protein sequences with N-terminal linkers that are unalignable to human NLRP1 in this region. Four additional clades (lagomorphs, megabats, cetaceans, and felines, marked as gray) lack the NLRP1 gene altogether.

We further observed that this cleavage site is largely absent in non-primate species (Figure 2.9), suggesting that a 3Cpro cleavage site mimic emerged in simian primates 30–40 million years ago. While many other mammalian species have a region that is alignable to the primate linker, we noted that this region is unalignable to any sequence in the linker region of NLRP1 proteins from rodents or bats (Figure 2.8B and Figure 2.9). Despite this, we found that there was weak cleavage of mouse NLRP1B at a site closer to the N-terminus than the 127-GCTQGSER-134 site found in human NLRP1 (Figure 2.8D and Figure 2.15A), suggesting that an independent cleavage site could have arisen elsewhere in mouse NLRP1B. These data suggest that NLRP1 in other mammals may have convergently evolved cleavage sites in the linker region despite not having a cleavable sequence in the precise position that human NLRP1 is cleaved. Differential host susceptibility to NLRP1 cleavage and activation extends to the human population level. Using GnomAD (Karczewski et al., 2020), we sampled the alternative alleles within the direct cleavage site (Figure 2.8C). While this region does not appear to be highly polymorphic in humans, we note that one alternative allele (rs150929926) results in a Q130R mutation and is present in >1 in every 1000 African alleles sampled. Introducing this mutation into NLRP1, we find the Q130R mutation eliminates NLRP1 cleavage susceptibility to CVB3 3Cpro (Figure 2.8E). In the case of primate and human diversity alleles at the site of 3Cpro cleavage, we also find that loss of cleavage susceptibility results in a loss of inflammasome activation in response to 3Cpro (Figure 2.8F), supporting the aforementioned notion that single changes in the linker region can have drastic impacts on the ability of different hosts to respond to the presence of cytoplasmic 3Cpro.

3Cpro from diverse picornaviruses cleave and activate human NLRP1

Our evolutionary model predicted that NLRP1 would be cleaved by a broad range of

3Cpro from viruses in the enterovirus genus (Figure 2.1B). To test this hypothesis, we cloned

3Cpro from representative viruses from four additional major species of human enteroviruses:

enterovirus 71 (EV71, species: Enterovirus A), poliovirus 1 (PV1, species: Enterovirus C),

enterovirus D68 (EV68, species: Enterovirus D), human rhinovirus A (HRV, species: Rhinovirus

A), in order to compare them to the 3Cpro from CVB3 (species: Enterovirus B) (Figure 2.10A).

Despite <50% amino acid identity between some of these proteases (Figure 2.11), the overall

structures of these proteases are similar (Figure 2.12) and the cleavage motifs are closely related

(Figure 2.10A). Consistent with this predicted target similarity and prior data with HRV

(Robinson et al., 2020), we found that every tested member of enterovirus 3Cpro was able to

cleave NLRP1 between residues 130 and 131 (Figure 2.10B). Moreover, expression of every

tested enterovirus 3Cpro resulted in activation of the inflammasome in a manner that was

dependent on cleavage at the 127-GCTQGSER-134 site (Figure 2.10C).
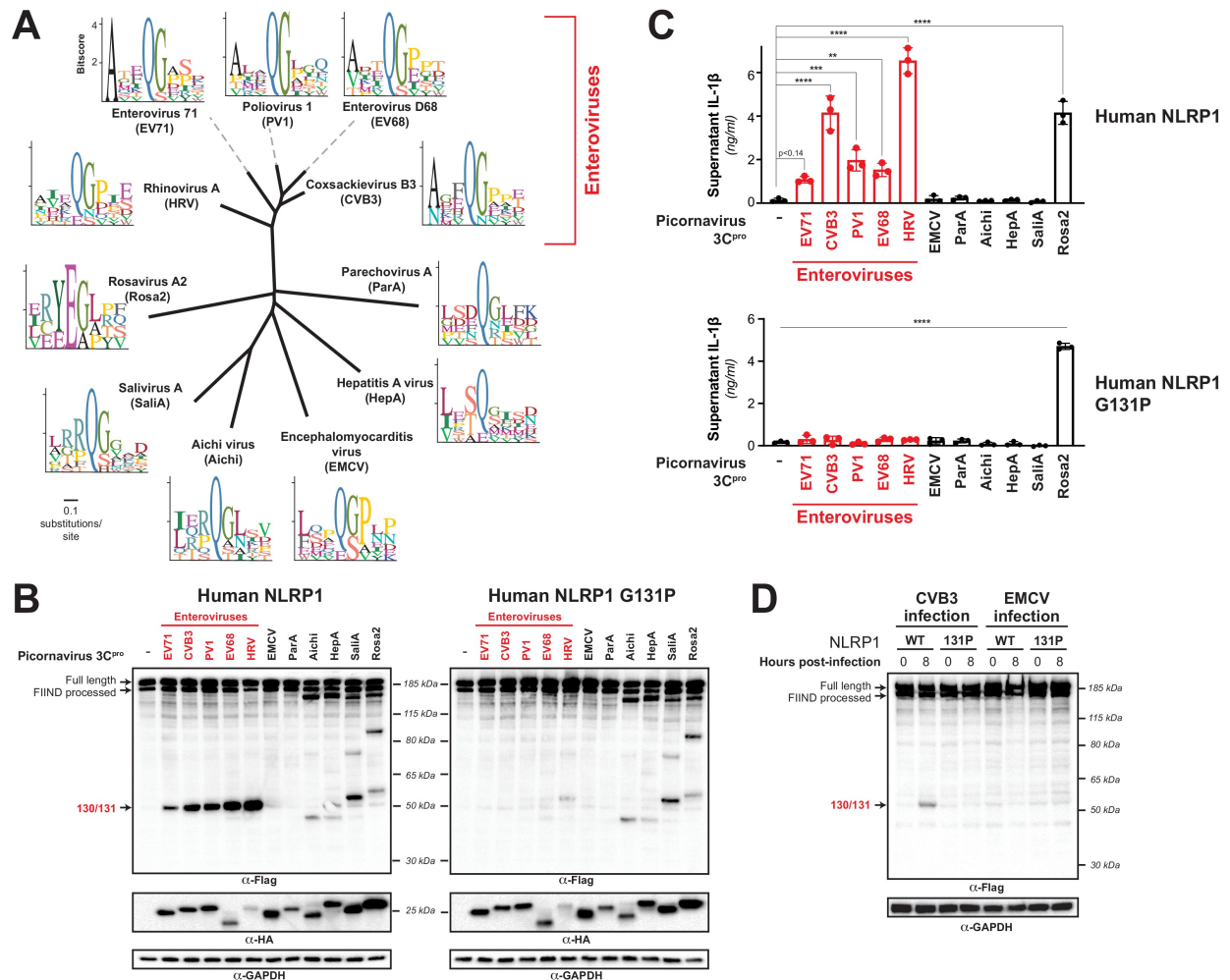
Figure 2.10. Diverse picornavirus 3Cpros cleave and activate NLRP1 at independently evolved sites. (A) Phylogenetic tree of 3Cpro protein sequences for the indicated picornaviruses (Figure 2.11). Shown next to the virus name is the sequence motif generated from the known sites of 3Cpro polyprotein cleavage in that specific virus. (B) Immunoblot depicting human NLRP1 cleavage by the indicated picornaviral 3Cpro. Abbreviations are as in (A). Assays were performed as in Figure 2.3D. (left) Cleavage assays against WT NLRP1. (right) Human NLRP1 G131P mutant used in Figure 2.3. (C) Release of bioactive IL-1β into the culture supernatant was measured using HEK-Blue IL-1β reporter cells as in Figure 2.4B. Data were analyzed using one-way ANOVA with Tukey's post-test. ** = p<0.01, *** = p<0.001, **** = p<0.0001. (D) Immunoblot depicting human NLRP1 cleavage at the indicated timepoints after infection with 250,000 PFU (MOI = ~1) CVB3 or EMCV. HEK293T cells were transfected using 100 ng of either WT NLRP1 or NLRP1 G131P and, 24 hr later, either mock infected (0 hr timepoint) or infected with CVB3 or EMCV as indicated (8 hr timepoint). All samples were harvested 32 hr post-transfection and immunoblotted with the indicated antibodies.

```
Coxsackievirus B3 3Cpro    1   GP--AFEFAVAMMK---RNSSTVKTEYG-------EFTMLGIYDRWAVLPRHAKPGP--------TILMN
Enterovirus D68 3Cpro      1   GP--GFDFAQAIMK---KNTVIARTEKG-------EFTMLGVYDRVAVIPTHASVGE--------IIYIN
Poliovirus 1 3Cpro         1   GP--GFDYAVAMAK---RNIVTATTSKG-------EFTMLGVHDNVAILPTHASPGE--------SIVID
Rhinovirus A 3Cpro         1   GP--EEEFGRSILK---NNTCVITTDNG-------KFTGLGIYDKTLIIPTHADPGR--------EVQVN
Enterovirus 71 3Cpro       1   GP--SLDFALSLLR---RNIRQAQTDQG-------HFTMLGVRDRLAILPRHSQPGK--------TIWVE
Hepatitis A virus 3Cpro    1   S---TLEIAGLVRK--NLVQFGVGEKNGCVR---WVMNALGVKDDWLLVPSHAYKFEKDYEMMEFYFNRG
Rosavirus A2 3Cpro         1   GL--PQIYRPVVANCFPINFYDCDPRDNARSGGVFTLTAVGMYDRTYICNAHGFKDA-------THIGLR
EMCV 3Cpro                 1   GPNPTMDFEKFVAK-FVTAPIGFVYPTGV-----STQTCLLVKGRTLAVNRHMAESD------WTSIVVR
Aichi virus 3Cpro          1   G------ISPAVPG-ISNNVVHVESGNGLNK---NVMSGFYIFSRFLLVPTHLREPH------HTTLTVG
Salivirus A 3Cpro          1   G------FDPAVMK-IMGNVDSFVTLSGTKP--IWTMSCLWIGGRNLIAPSHAFVSD---EYEITHIRVG
Parechovirus A 3Cpro       1   AP-----YDGQLEHIISQMAYITGSTTG------HITHCAGYQHDEIILHGHSIKYL--EQEEELTLHYK
                                                                                                *


Coxsackievirus B3 3Cpro    51  DQEVGVLDAKEL-VDKDGTNLELTLLKLNRNEKFRDIRGFLAKEEV----EVNEAVLAINTS-KFPNMYI
Enterovirus D68 3Cpro      51  DVETRVLDACAL-RDLTDTNLEITIVKLDRNQKFRDIRHFLPRCED----DYNDAVLSVHTS-KFPNMYI
Poliovirus 1 3Cpro         51  GKEVEILDAKAL-EDQAGTNLEITIITLKRNEKFRDIRPHIPTQIT----ETNDGVLIVNTS-KYPNMYV
Rhinovirus A 3Cpro         51  GIHTKVLDSYDL-YNRDGVKLEITVIKLDRNEKFRDIRKYIPETED----DYPECNLALSAN-QVEPTII
Enterovirus 71 3Cpro       51  HKLINVLDAVEL-VDEQGVNLELTLVTLDTNEKFRDITKFIPEVIT----GASDATLVINTE-HMPSMFV
Hepatitis A virus 3Cpro    63  GTYYSISAGNVVIQSLDVGFQDVVLMKVPTIPKFRDITQHFIKKGGP-PRALNRLATLVTTV-NGTPMLI
Rosavirus A2 3Cpro         62  GRVYPISEINKKHVRRNHRRTDLMIFQIPDGDCVRNILKYFRKSPE----EAPSRSPAVMAVRGKFNIDV
EMCV 3Cpro                 59  GVSHTRSSVKIIAIAKAGKETDVSFIRLSSGPLFRDNTSKFVKASDVLP---HSSSPLIGIMNVDIPMMY
Aichi virus 3Cpro          55  ADTYDWATLQTQ------EFGEITIVHTPTSRQYKDMRRFIGAHP-------HPTGLLVSQF-KAAPLYV
Salivirus A 3Cpro          59  SRTLDVSRVTRV------DDGELSLLSVPDGPEHKSLIRYIRSAS-------PKSGILASKF-SDTPVFV
Parechovirus A 3Cpro       58  NKVFPIEQPSVTQVTLGGKPMDLAIVKCKLPFRFKKNSKYYTNKI-------GTESMLIWMTEQGIITKE


Coxsackievirus B3 3Cpro    114 ---PVGQVTEYGFLNLGGTPTK------RMLMYNFPTRAGQ𝗖GGVLMS-----TGKVLGIHVGG-NGHQ-
Enterovirus D68 3Cpro      114 ---PVGQVTNYGFLNLGGTPTH------RILMYNFPTRAGQ𝗖GGVVTT-----TGKVIGIHVGG-NGAQ-
Poliovirus 1 3Cpro         114 ---PVGAVTEQGYLNLGGRQTA------RTLMYNFPTRAGQ𝗖GGVITC-----TGKVIGMHVGG-NGSH-
Rhinovirus A 3Cpro         114 ---KVGDVVSYGNILLSGNQTA------RMLKYNYPTKSGY𝗖GGVLYK-----IGQILGIHVGG-NGRD-
Enterovirus 71 3Cpro       114 ---PVGDVVQYGFLNLSGKPTH------RTMMYNFPTKAGQ𝗖GGVVTS-----VGKIIGIHIGG-NGRQ-
Hepatitis A virus 3Cpro    131 SEGPLKMEEKATYVHKKNDGTTVDLTVDQAWRGKGEGLPGM𝗖GGALVSSNQSIQNAILGIHVAG--GNSI
Rosavirus A2 3Cpro         127 ---LATCVESFAFVQMSGDVNY------GALRYHAMTMPGY𝗖GAPLISNDKA-AEKVLGIHMAS-NGAGI
EMCV 3Cpro                 126 T--GTFLKAGVSVPVETGQTFN------HCIHYKANTRKGW𝗖GSAILADLGG-SKKILGFHSAG---SM-
Aichi virus 3Cpro          110 ---RISDNRILDLDFPGVVVCK------QAYGYRAATFEGL𝗖GSPLVTDDPS-GVKILGLHVAGVAGTS-
Salivirus A 3Cpro          114 ---SFWNGKSHSTPLPGVVDEK------DSFTYRCSSFQGL𝗖GSPMIATDPG-GLGILGIHVAGVAGYN-
Parechovirus A 3Cpro       120 ---VQRVHHSGGIKTREGTEST------KTISYTVKSCKGM𝗖GGLLISKVEG-NFKILGMHIAG-NGEM-
                                                                       * **                * *


Coxsackievirus B3 3Cpro    169 GFSAA--LLKHYFNDE--------
Enterovirus D68 3Cpro      169 GFAAM--LLHSYFTDTQ-------
Poliovirus 1 3Cpro         169 GFAAA--LKRSYFTQSQ-------
Rhinovirus A 3Cpro         169 GFSAM--LLRSYFTDTQ-------
Enterovirus 71 3Cpro       169 GFCAG--LKRSYFASE--------
Hepatitis A virus 3Cpro    199 LVAKL--VTQEMFQNIDKKIE-SQ
Rosavirus A2 3Cpro         187 AYGTS--VYQSDFENLE-----YE
EMCV 3Cpro                 183 GVAAASIISQEMIDAVVQAFE-PQ
Aichi virus 3Cpro          170 GFSAP--IHP-ILGQITQFATTQQ
Salivirus A 3Cpro          174 GFSAR--LTPERVQAFLSHLATPQ
Parechovirus A 3Cpro       179 GVAIPFNFLKNDMSD--------Q
```

Figure 2.11. Alignment of 3Cpros used in this study. Sequences were aligned using MAFFT (Katoh and Standley, 2013) and used to generate the phylogenetic tree shown in Figure 2.10A. Asterisks indicate residues 100% conserved in all sequences. The position of the catalytic cysteine, analogous to C147 in CVB3 3Cpro, is highlighted in yellow.

A

█ Poliovirus (PDB 1L1N)
█ Enterovirus 71 (PDB 3OSY) - RMSD = 0.732
█ Cosackievirus B3 (PDB 3OSY) - RMSD = 0.659
█ Enterovirus D68 (PDB 3ZV8) - RMSD = 0.692
█ Human rhinovirus (PDB 2B0F) - RMSD = 1.204

B

█ Poliovirus (PDB 1L1N)
█ Hepatitis A virus (PDB 2H6M) - RMSD = 0.754 (near active site), 9.310 (overall)
█ Senacavirus (PDB 6L0T) - RMSD = 0.744 (near active site), 9.080 (overall)
█ Foot and mouth disease virus (PDB 2BHG) - RMSD = 1.870 (near active site), 3.051 (overall)

Figure 2.12. Structural similarity of picornavirus 3Cpros. (A) Structures of the indicated enterovirus 3Cpros were aligned to poliovirus 3Cpro using Pymol (https://pymol.org/2/ - The PyMOL Molecular Graphics System, Version 2.0 Schrödinger, LLC.). For each enterovirus species used in this study, PDB codes are indicated in parentheses and Pymol-calculated RMSD values are shown. The catalytic cysteine, C147, in the poliovirus 3Cpro structure is shown as a ball-and-stick representation (red stick and yellow ball for the catalytic S atom). Despite substantial divergence in amino acid identity, the overall fold and active site configuration of these enzymes is similar. (B) Structures of the indicated picornavirus 3Cpros were aligned to poliovirus 3Cpro using Pymol, with a similar representation of the catalytic C147 residue in poliovirus 3Cpro as in (A). RMSD values are shown for alignments to either the whole poliovirus 3Cpro structure ('overall' RMSD) or only the 50 amino acids flanking the catalytic cysteine, C147 ('near active site' RMSD). The displayed aligned structures are from the 'near active site' alignment. Neither senecavirus nor foot and mouth disease virus (FDMV) were used in this study, but are included as additional representatives of non-enterovirus 3Cpro enzymes for which there are experimentally determined molecular structures. Compared to proteases aligned in (A), divergent picornavirus proteases show greater divergence in overall fold as indicated by the larger 'overall' RMSD values. However, comparison of the regions around the active site still show high structural similarity, consistent with the constraint on protease evolution and similarity of cleavage specificity shown in Figure 2.10A.

Enteroviruses are only one genus within the broad *Picornaviridae* family of viruses. We next asked if viruses in other *Picornaviridae* genera that infect humans are also able to cleave and activate human NLRP1. We were unable to generate a robust sequence motif for every genera of picornavirus due to lower depth of publicly available sequences. Instead, we cloned a 3Cpro from a representative of every genus of picornavirus that are known to infect humans: encephalomyocarditis virus (EMCV, genus: Cardiovirus), parechovirus A virus (ParA, genus: Parechovirus), Aichi virus (Aichi, genus: Kobuvirus), hepatitis A virus (HepA, genus: Hepatovirus), salivirus A virus (SaliA, genus: Salivirus), and rosavirus A2 (Rosa2, genus: Rosavirus). Each of these viral proteases is <20% identical to CVB3 3Cpro. Despite this, the sequence motif built from cleavage sites within the polyprotein of these individual viruses is broadly consistent with the motif seen in enteroviruses (Figure 2.10A), reflective of the strong evolutionary constraint on evolution of the sequence specificity of these proteases and overall structural conservation of the active sites of these proteases (Figure 2.12). Interestingly, we found that there was substantial variation in NLRP1 cleavage sites across these diverse 3Cpro even though most picornavirus proteases cleaved human NLRP1 to some degree (Figure 2.10B). For instance, while 3Cpro from EMCV and ParA did not cleave NLRP1, we observed distinct cleavage sites for 3Cpro from Aichi, HepA, SaliA and Rosa2 (Figure 2.10B), all of which have at least one cleavage site predicted to occur in the linker region (expected size between 40 kDa and 67 kDa). Confirming that these proteases cleave at a site that is distinct from that of enteroviruses, the G131P NLRP1 mutant is still cleaved by the non-enteroviral proteases (Figure 2.10B).

Surprisingly, when we interrogated NLRP1 inflammasome activation by 3Cpros from Aichi, HepA, SaliA, and Rosa2, all of which robustly cleave NLRP1 at a site in the linker region, we found that only Rosa2 was able to activate the NLRP1 inflammasome (Figure 2.10C). While it is possible that NLRP1 cleavage by 3Cpro from these other viruses is too weak or in a region that may be inconsistent with activation, we also noted that there are obvious cleavage sites in NLRP1 that are outside of the linker region and closer to the FIIND autocleavage site. Cleavage at these sites in NLRP1, or cleavage of other host genes, may interfere with activation that may have otherwise been induced by 3Cpro cleavage in the linker region. Indeed, we find that co-expression of 3Cpro from Aichi, HepA, SaliA can attenuate NLRP1 activation by TEV protease (Figure 2.13), consistent with the idea that these three proteases can actively block NLRP1 activation. Further investigation will be needed to determine the exact mechanism by which this occurs. Nevertheless, our data demonstrate that non-enteroviral 3Cpros can cleave NLRP1 at independent sites in the rapidly evolving linker region and can, in at least one case, activate the human NLRP1 inflammasome.

To further confirm that 3Cpro cleavage (or lack thereof) of NLRP1 is reflective of 3Cpro during viral infection, we infected cells expressing WT or 131P NLRP1 with EMCV. Consistent with our co-transfection experiments, we see no cleavage of NLRP1 when we infect with EMCV, despite seeing robust cleavage when we infect with CVB3 (Figure 2.10D). Likewise, we see no IL-1β release when we infect either inflammasome-reconstituted HEK293T cells or inflammasome-competent HaCaT cells with EMCV (Figure 2.14). These data indicate that evolution of viral 3Cpro cleavage specificity alters whether a virus can be sensed by the NLRP1 tripwire or not.
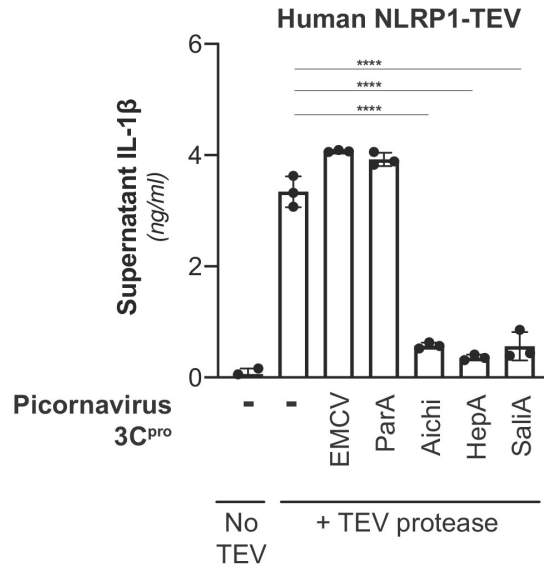
Figure 2.13. Inhibition of NLRP1 activation by non-enteroviral 3Cpro. HEK293T cells were transfected with inflammasome components as in Figure 2A using 100 ng TEV protease or pQCXIP empty vector, but with the additional inclusion of a non-enterovirus 3Cpro or empty vector (100 ng). Release of bioactive IL-1β into the culture supernatant was measured using HEK-Blue IL-1β reporter cells as in Figure 2.4B. Data were analyzed using one-way ANOVA with Tukey's post-test comparing all conditions containing TEV protease. **** = p<0.0001.
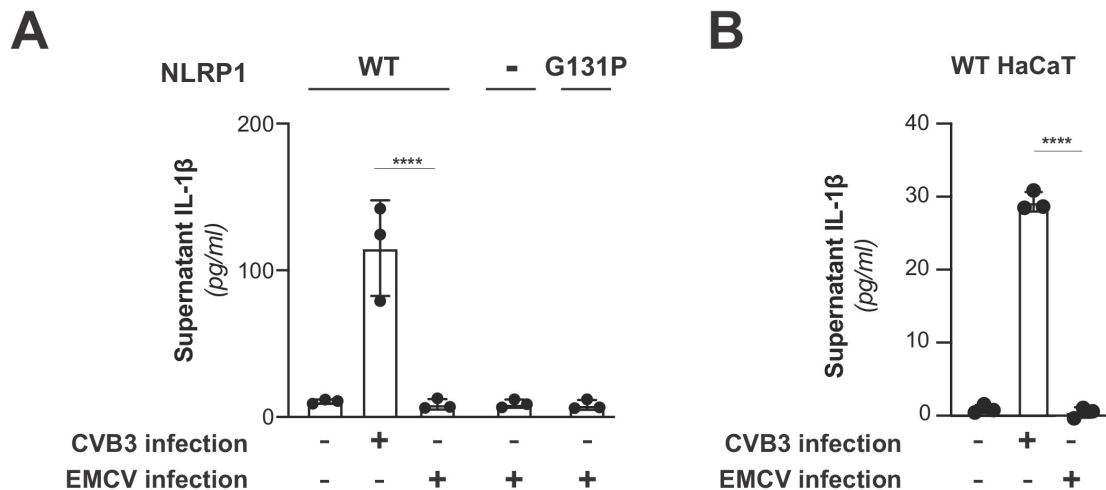
Figure 2.14. EMCV infection does not activate the NLRP1 inflammasome. (A) HEK293T cells were transfected with inflammasome components as in Figure 2.4C and mock infected or infected with 250,000 PFU (MOI = ~1) CVB3 or EMCV. Eight hours post-infection, culture supernatant was collected and bioactive IL-1β was measured as in Figure 2.4C. Data from the mock and CVB3 infections are reproduced from Figure 2.4C and included as a point of reference as they were done in parallel. Data were analyzed using two-way ANOVA with Sidak's post-test. **** = p<0.0001. (B) WT or knockout (Figure 2.7) HaCaT cell lines were mock infected or infected with 100,000 PFU (MOI = ~0.4) CVB3 of EMCV as in Figure 2D. Forty-eight hours post-infection, culture supernatant was collected and bioactive IL-1β was measured as in Figure 2.4D. Data from the mock and CVB3 infections are reproduced from Figure 2.4D and included as a point of reference as they were done in parallel. Data were analyzed using two-way ANOVA with Sidak's post-test. **** = p<0.0001.

Enterovirus 3Cpro cleaves and activates mouse NLRP1B in a virus- and host allele-specific manner

Two bacterial pathogen effectors are known to activate mouse NLRP1B, the LF protease from *B. anthracis* (Boyden and Dietrich, 2006; Greaney et al., 2020; Moayeri et al., 2010; Terra et al., 2010); (Chavarría-Smith and Vance, 2013; Levinsohn et al., 2012) and the IpaH7.8 E3 ubiquitin ligase from *Shigella flexneri* (Sandstrom et al., 2019). Interestingly, in both of these cases, activation is specific to the 129 allele of mouse NLRP1B, whereas the B6 allele of NLRP1B is not activated by these pathogenic effectors. Given the power of mouse models for understanding inflammasome biology, we wished to determine if 3Cpros cleave and activate mouse NLRP1B.

Strikingly, when we co-transfected NLRP1B from either the 129 or the B6 strains with diverse enterovirus 3Cpros, we observed allele-specific cleavage products (Figure 2.15A). Consistent with data in Figure 2.8D, we observed weak cleavage of 129 NLRP1B by CVB3 3Cpro. In addition, we found that 3Cpro from other enteroviruses varied substantially in their ability to cleave 129 NLRP1B, including no detectable cleavage with EV71 3Cpro and a different dominant position of cleavage by HRV 3Cpro. Despite this variation, we only observed weak cleavage (Figure 2.15A, left) and little to no inflammasome activation (Figure 2.15B, left) by any enterovirus 3Cpros tested against 129 NLRP1B. In contrast, enterovirus 3Cpro cleavage of B6 NLRP1B resulted in a consistent-sized cleavage product across all enterovirus 3Cpros that ranged in intensities between the different viral proteases, more similar to our observations with human NLRP1. Most interestingly, we observed that co-transfection with HRV 3Cpro resulted in the appearance of a very strong cleavage product (Figure 2.15A, right), almost complete loss of full length B6 NLRP1B (Figure 2.15A and B, right) and very strong activation of the

inflammasome (Figure 2.15B, right). These data indicate that mouse NLRP1B can also be cleaved and activated by viral proteases, which suggests that the evolution of the N-terminus of NLRP1B between closely related mouse strains (Figure 2.16) is not only shaping susceptibility to tripwire cleavage by the bacterial LF protease, but also impacts tripwire cleavage by viral 3Cpros. Taken together, these data further support the model in which both host and viral evolution, even within closely related host and viral species, shape the outcome of the interaction between NLRP1 and 3Cpro.
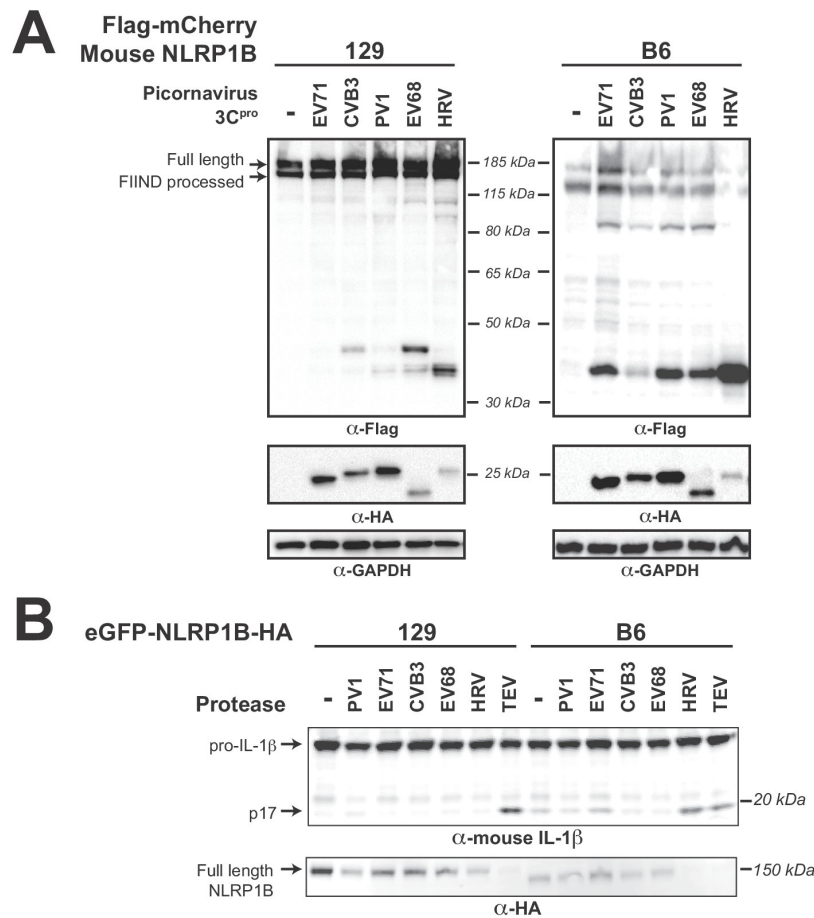
Figure 2.15. Diverse picornavirus 3Cpros cleave and activate mouse NLRP1B at independently evolved sites. (A) Immunoblot depicting CVB3 3Cpro cleavage susceptibility of two alleles (129 and B6) of mouse NLRP1B. Assays were performed as in Figure 2.3D. (B) Immunoblot depicting mouse NLRP1B activation (maturation of IL-1β) by enterovirus 3Cpro and TEV protease. HEK293T cells were co-transfected using 100 ng of the indicated protease, 50 ng mouse IL-1β, 50 ng mouse CASP1, and either 4 ng of 129 NLRP1B or 2.5 ng of B6 NLRP1B constructs and immunoblotted with the indicated antibodies. Appearance of the mature p17 band of IL-1β indicates successful assembly of the NLRP1B inflammasome and activation of CASP1.

```
NLRP1B (129)    1    MEESPPKQKSNTKVAQHEGQQDLNTT----RHMNVEL-KHRPKLERHLKLGMIPVVYMKQ
NLRP1B (B6)     1    MEQSQPKKKSRTKVAQHEGQLNLNPTFKTRKRKEVELMKRRPKPEGHLKLGTIPKVHIKQ
                     ** * ** ** ********  ** *        *** * *** * ***** ** *  **

NLRP1B (129)    56   GEEILYPAQSLREENLIQNFTSLLLLQKLCPKDPENMIRKSWASCVPEEGGHMINIQDLF
NLRP1B (B6)     61   KGETLDPTWSRKRKNLVQKLTNLLLFEKLCSRGSENLIRKSWYSCEEEERGHMIEIQDLF
                      * *  *   *      ** *  * ***  ***     ** ***** **  ** **** *****

NLRP1B (129)    116  GPNIGTQKEPQLVIIEGAA
NLRP1B (B6)     121  GPNRGTHKKPQLVIIEGAA
                     *** ** * *********
                                       Start of NBD
```

Figure 2.16. Alignment of N-termini of mouse NLRP1B 129 and B6 alleles. Sequences were aligned using MAFFT (Katoh and Standley, 2013). Asterisks indicate conserved residues and the start of the nucleotide-binding domain (NBD) is shown.

Discussion

Pathogens and their hosts are locked in a continual evolutionary conflict in which each side is attempting to exploit the others' weakness. One particularly successful strategy that pathogens have adopted is to exploit host processes that are highly constrained, leaving the host little room to evolutionarily adapt to overcome the pathogen. For instance, molecular mimicry of host proteins is commonly deployed by pathogens to antagonize host defenses, as it limits the evolutionary options for the host to counter-evolve (Elde and Malik, 2009). Beyond mimicry of entire proteins or protein domains, pathogens can also mimic so-called 'short linear motifs' (SLIMs) through evolution of only a small number of amino acids to hijack highly conserved host processes such as post-translational modifications or binding by small protein domains (Chemes et al., 2015; Hagai et al., 2014). Although these strategies are generally described as taking advantage of host evolutionary constraint, pathogens also have potential weak points of evolutionary constraint. In particular, proteases from positive-sense RNA viruses, such as picornaviruses, need to specifically cleave numerous sites within the viral polyprotein in order to reproduce. Thus, changing protease specificity requires concomitant changes to several

48

independent cleavage sites, which is difficult to accomplish in a single evolutionary step. On top of that, protease cleavage motifs often only span a small number of amino acids (Schechter and Berger, 1967), potentially facilitating the independent evolution of these SLIMs in host proteins. Here, we show that the inflammasome protein, NLRP1, serves as a sensor for diverse proteases from the *Picornaviridae* family of human pathogens by mimicking the highly conserved protease cleavage sites found within the viral polyproteins. By exploiting a constrained feature of viral evolution and tying it to a pro-inflammatory immune response, such a system allows the immune system to recognize and respond to a wide range of viral proteases expressed in the host cytoplasm. NLRP1 represents one of the few known cases of mammalian ETI (Cui et al., 2015; Fischer et al., 2020; Jones et al., 2016), where pathogen-mediated cleavage of NLRP1 promotes its activation. By holding the small C-terminal CARD-containing fragment in a non-covalent association with the larger N-terminal fragment, the majority of the protein can serve as a sensor for pathogen-encoded effectors (Mitchell et al., 2019; Taabazuing et al., 2020). This presents an opportunity to allow NLRP1 to evolve to be recognized by pathogenic effectors, ultimately leading to degradation of the N-terminal fragment. Indeed, mouse NLRP1B has been shown to be specifically cleaved by the protease-containing secreted effector from B. anthracis (LF) as well as being ubiquitylated by an E3-ubiquitin ligase from S. flexneri (IpaH7.8) (Sandstrom et al., 2019). While these two examples provide evidence that the mouse NLRP1B inflammasome operates by a 'functional degradation' model, a direct pathogen-encoded activator of human NLRP1 had remained elusive. We now show, using an evolution-guided approach, that proteases from diverse picornaviruses, including human pathogens such as coxsackievirus B3 (CVB3), human rhinovirus A (HRV), enterovirus D68 (EV68) and poliovirus 1 (PV1) and rosavirus A2 (Rosa2), specifically cleave several independently evolved sites in human NLRP1, leading to

activation of the NLRP1 inflammasome and release of pro-inflammatory cytokines such as IL-1β. Together with recent findings (Robinson et al., 2020), our work has thus identified proteases from a diverse range of picornaviruses as pathogen-encoded activators of human NLRP1. We previously speculated that the unique domain architecture of NLRP1 would allow the N-terminal linker of human NLRP1 to freely evolve to be recognized by pathogenic effectors. Indeed, by harvesting publicly available enterovirus polyprotein sequences for known 3Cpro cleavage sites, we created a 3Cpro cleavage motif that was used to successfully predict the site of enterovirus 3Cpro cleavage at position 130–131 within the rapidly-evolving linker NLRP1. Additionally, our finding that numerous enteroviruses also cleave at the Q130-G131 site and activate pro-inflammatory cytokine release suggests that human NLRP1 serves as a general enteroviral protease sensor by encoding a polyprotein cleavage site mimic. Our phylogenetic assessment of the Q130-G131 3Cpro cleavage site in NLRP1 suggests that NLRP1 sensing of enteroviruses at this specific site is an innovation in the primate lineage, and is largely absent in all other mammalian lineages with exception of a possible independent acquisition by members within the Caprinae subfamily of mammals (e.g. goats, sheep) (Figure 2.5). Interestingly, even within the primate lineage and a small fraction of the human population, some primate orthologs and human variants are cleavage-resistant and therefore do not activate the inflammasome upon cytoplasmic expression of 3Cpro. Such data may hint at three different possible explanations for these changes. First, evolutionary drift in the absence of pressure from pathogenic enteroviruses may account for loss of enterovirus 3Cpro responsiveness in these genes. Second, selection to sense another viral protease may shape the same region of the linker. Finally, while the ETI model of NLRP1 suggests that enteroviral cleavage of NLRP1 has evolved to activate a beneficial immune response in certain contexts, the effects of NLRP1 overactivation may be

detrimental in other contexts. In human skin keratinocytes, where NLRP1 is regarded as the key inflammasome, all components of the NLRP1 inflammasome are basally expressed and thus poised to elicit an inflammatory response (Zhong et al., 2016). Here, germline mutations in NLRP1 that result in overactivation can cause growth of warts in the upper airway in a condition known as recurrent respiratory papillomatosis (JRRP) (Drutman et al., 2019) and an increase in skin cancer susceptibility and skin disorders such as multiple self-healing palmoplantar carcinoma (MSPC), familial keratosis lichenoides chronica (FKLC) and auto-inflammation with arthritis and dyskeratosis (AIADK) (Grandemange et al., 2017; Herlin et al., 2020; Soler et al., 2013; Zhong et al., 2016; Zhong et al., 2018). Additional recent work has indicated that dsRNA can also activate the NLRP1 inflammasome in human keratinocytes (Bauernfried et al., 2020), adding to the role that NLRP1 may play in the inflammatory response. Beyond the skin, NLRP1 is also basally expressed in tissues such as the gut and brain (D'Osualdo et al., 2015; Kaushal et al., 2015; Kummer et al., 2007), which are sites of picornavirus replication where overactivation upon infection may result in immunopathology. Further in vivo studies will help determine the role of NLRP1 in antiviral immunity and/or immunopathology during viral infection. Facilitating these studies, our discovery that 3Cpro from HRV potently cleaves and activates NLRP1B from B6 but not 129 mice suggests that rhinovirus infection of B6 mice may be a good model for studying the in vivo consequences of viral-mediated NLRP1 inflammasome activation. Intriguingly, 3Cpros from nearly every genus of human-infecting picornavirus can cleave NLRP1 somewhere in the rapidly evolving linker region between the PYD and NLR domain, although only enteroviruses cleave at the specific site between position 130 and 131. These data suggest that this extended linker, which we previously found showed widespread signatures of positive selection (Chavarría-Smith et al., 2016), may be convergently evolving to mimic

cleavage sites from a diverse range of viruses at multiple independent sites. Supporting that model, we observe a similar phenomenon in mouse NLRP1B, where multiple viral proteases cleave at different sites within NLRP1 in a strain-specific manner. These data highlight the important functional differences in cleavage specificity between even closely related 3Cpro that are not accounted for by predictive models. Further studies will be required to understand the precise relationships between sites within NLRP1 and individual protease specificity. Intriguingly, not all these cleavage events lead to inflammasome activation in the same way that enteroviral cleavage does, and we find evidence for antagonism of NLRP1 activation by some 3Cpros, suggesting that additional activities of 3Cpro may be the next step in the arms race, serving to prevent inflammasome activation even after the tripwire has been tripped.

Taken together, our work suggests that host mimicry of viral polyprotein cleavage motifs could be an important evolutionary strategy in the ongoing arms race between host and viruses. Indeed, one explanation for the somewhat surprising observation that the specificity of viral proteases changes at all within a viral family such as the picornaviruses is that there is evolutionary pressure from the host to evolve cleavage sites and protease specificity. Prior work has highlighted the roles that viral proteases can play in antagonizing host immune factors and driving host evolution to avoid being cleaved (Patel et al., 2012; Stabell et al., 2018). In that case, the viral proteases would evolve to antagonize new factors while maintaining polyprotein cleavage. However, mimicry coupled with cleavage-activating immunity as seen with NLRP1 could be an even stronger pressure to shape the protease specificity. By turning the tables, these host processes may drive the type of functional diversification of viral protease specificity that we observe in order to avoid cleaving NLRP1 and other similar ETI factors. We expect that this

work may lead to the discovery that such an evolutionary strategy may be more broadly deployed at other sites of host-pathogen conflicts.

Materials and methods

Motif generation and search

To build the motif, 2658 nonredundant enteroviral polyprotein sequences were collected from the Viral Pathogen Resource (ViPR) and aligned with 20 well-annotated reference enteroviral polyprotein sequences from RefSeq (Supplementary file 2.1). P1 and P1' of the eight annotated cleavage sites across the RefSeq sequences served as reference points for putative cleavage sites across the 2658 ViPR sequences, with the exception of enterovirus D polyproteins. The 3Cpro cleavage site for VP3-VP1 within polyproteins from the clade of enterovirus D have been described to be undetectable and have thus been removed (Tan et al., 2013). Four amino acyl residues upstream (P4-P1) and downstream (P1'-P4') of each cleavage site were extracted from every MAFFT-aligned polyprotein sequence, resulting in 2678 sets of cleavage sites (RefSeq sites included). Each set of cleavage sites representative of each polyprotein was then concatenated. Next, 1884 duplicates were removed from the 2678 concatenated cleavage sites. The remaining 796 nonredundant, concatenated cleavage sites were then split into individual 8-mer cleavage sites and the 6333 8-mers were aligned using MAFFT to generate Geneious-defined sequence logo information at each aligned position. Pseudo-counts to the position-specific scoring matrix were adjusted by total information content within each position relative to the two most information-dense position P1 and P1' (pseudocount = 0) and the least information-dense position P3 (pseudocount = 1). The 0.002 p-value threshold for FIMO motif searching against human NLRP1 was determined to optimize the capture of 95% of initial input

cleavage sites within the set of 2678 whole enteroviral polyproteins and a majority sites within a previously described dataset of enteroviral 3Cpro targets (Laitinen et al., 2016).

NetSurfP

Prediction of the coil probability across human NLRP1 (NCBI accession NP_127497.1) was conducted using the protein FASTA as the input for the NetSurfP web server (http://www.cbs.dtu.dk/services/NetSurfP/).

Sequence alignments, phylogenetic trees, and NLRP1 phylogenomics

Complete polyprotein sequences from 796 picornaviruses with non-redundant 3Cpro cleavage sites (see 'Motif generation and search' section above) were downloaded from ViPR. Sequences were aligned using MAFFT (Katoh and Standley, 2013) and a neighbor-joining phylogenetic tree was generated using Geneious software (Kearse et al., 2012). An alignment and phylogenetic tree of all the 3Cpro sequences used in this study was generated similarly. To identify mammalian NLRP1 homologs, and species that lack NLRP1, the human NLRP1 protein sequence was used to query the RefSeq protein sequence database, a curated collection of the most well-assembled genomes, using BLASTp (Altschul et al., 1997). Sequences were downloaded and aligned using MAFFT implemented in Geneious software. Consensus sequence logos shown were generated using Geneious software. We determined that NLRP1 was 'absent' from a clade of species using the following criteria: (1) when searching with human NLRP1, we found an obvious homolog of another NLRP protein (generally NLRP3, NLRP12 or NLRP14) but no complete or partial homolog of NLRP1 and (2) this absence was apparent in every member of the clade of species (>2 species) in the RefSeq database.

Plasmids and constructs

For NLRP1 cleavage assays, the coding sequences of human NLRP1 WT (NCBI accession NP_127497.1), human NLRP1 mutants (G131P, G131R, Q130R, G127E), human NLRP1 TEV or mouse NLRP1B (129 allele, NCBI accession AAZ40510.1; B6 allele, NCBI accession XM_017314698.2) were cloned into the pcDNA5/FRT/TO backbone (Invitrogen, Carlsbad, CA) with an N-terminal 3xFlag and mCherry tag. For NLRP1 activation, the same sequences were cloned into the pQCXIP vector backbone (Takara Bio, Mountain View, CA) with a C-terminal Myc tag (human NLRP1 sequences) or N-terminal EGFP and C-terminal HA (mouse NLRP1B sequences). Vectors containing the coding sequences of human NLRP1 TEV (NLRP1-TEV2), ASC, human and mouse CASP1, human IL-1β-V5, mouse IL-1β, and TEV protease (Chavarría-Smith et al., 2016) were generous gifts from Dr. Russell Vance, UC Berkeley. Single point mutations were made using overlapping stitch PCR. A list of primers used to generate the wild-type and mutant NLRP1 constructs are described in Supplementary file 2.5. CVB3 3Cpro and EMCV 3Cpro were cloned from CVB3-Nancy and EMCV-Mengo plasmids (generous gifts from Dr. Julie Pfeiffer, UT Southwestern). Remaining 3Cpro sequences were ordered as gBlocks (Integrated DNA Technologies, San Diego, CA). Each 3Cpro was cloned with an N-terminal HA tag into the QCXIP vector backbone. Catalytic mutations were made using overlapping stitch PCR. A list of primers and gBlocks used to generate the protease constructs are described in Supplementary file 2.5.

Following cloning, all plasmid stocks were sequenced across the entire inserted region to verify that no mutations were introduced during the cloning process.

Cell culture and transient transfection

All cell lines (HEK293T, HEK-Blue-IL-1β, and HaCaT) are routinely tested for mycoplasma by PCR kit (ATCC, Manassas, VA) and kept a low passage number to maintain less than one year since purchase, acquisition or generation. HEK293T cells were obtained from ATCC (catalog # CRL-3216), HEK-Blue-IL-1β cells were obtained from Invivogen (catalog # hkb-il1b) and HaCaT cells were obtained from the UC Berkeley Cell Culture Facility (https://bds.berkeley.edu/facilities/cell-culture) and all lines were verified by those sources. All cells were grown in complete media containing DMEM (Gibco, Carlsbad, CA), 10% FBS (Peak Serum, Wellington, CO), and appropriate antibiotics (Gibco, Carlsbad, CA). For transient transfections, HEK293T cells were seeded the day prior to transfection in a 24-well plate (Genesee, El Cajon, CA) with 500 µl complete media. Cells were transiently transfected with 500 ng of total DNA and 1.5 µl of Transit X2 (Mirus Bio, Madison, WI) following the manufacturer's protocol. HEK-Blue IL-1β reporter cells (Invivogen, San Diego, CA) were grown and assayed in 96-well plates (Genesee, El Cajon, CA).

HaCaT knockouts

To establish NLRP1 and CASP1 knockouts in human immortalized keratinocyte HaCaT cells, lentivirus-like particles were made by transfecting HEK293T cells with the plasmids psPAX2 (gift from Didier Trono, Addgene plasmid # 12260) and pMD2.G (gift from Didier Trono, Addgene plasmid # 12259) and either the pLB-Cas9 (gift from Feng Zhang, Addgene plasmid # 52962) (Sanjana et al., 2014) or a plentiGuide-Puro, which was adapted for ligation-independent cloning (kindly gifted by Moritz Gaidt) (Schmidt et al., 2015). Guide sequences are shown in Supplementary file 2.5. Conditioned supernatant was harvested 48 and 72 hr post-

transfection and used for spinfection of HaCaT cells at 1200 x g for 90 min at 32°C. Forty-eight hours post-transduction, cells with stable expression of Cas9 were selected in media containing 100 µg/ml blasticidin. Blasticidin-resistant cells were then transduced with sgRNA-encoding lentivirus-like particles, and selected in media containing 1.3 µg/ml puromycin. Cells resistant to blasticidin and puromycin were single cell cloned by limiting dilution in 96-well plates, and confirmed as knockouts by Sanger sequencing (Figure 2.7).

NLRP1 cleavage assays

100 ng of epitope-tagged human NLRP1 WT, human NLRP1 mutants (G131P, G131R, Q130R, G127E), human NLRP1 TEV or mouse NLRP1B was co-transfected with 250 ng of HA-tagged protease-producing constructs. Twenty-four hours post-transfection, the cells were harvested, lysed in 1x NuPAGE LDS sample buffer (Invitrogen, Carlsbad, CA) containing 5% β-mercaptoethanol (Fisher Scientific, Pittsburg, PA) and immunoblotted with antibodies described below.

NLRP1 activity assays

For human NLRP1 activation assays, 5 ng of ASC, 100 ng of CASP1, 50 ng of IL-1β-V5, and 100 ng of various protease-producing constructs were co-transfected with 4 ng of either pQCXIP empty vector, wild-type or mutant pQCXIP-NLRP1-Myc constructs. For inhibitor treatments, cells were treated with either 0.5 µM MG132 or 1.0 µM MLN4924 18 hr after transfection. Twenty-four hours post-transfection, cells were harvested and lysed in 1x NuPAGE LDS sample buffer containing 5% β-mercaptoethanol or in 1x RIPA lysis buffer with protease

inhibitor cocktail (Roche) and immunoblotted with antibodies described below or culture media was harvested for quantification of IL-1β levels by HEK-Blue assays (see below).

For mouse NLRP1B activation assays, 50 ng of mouse CASP1, 50 ng of mouse IL-1β, and 100 ng of various protease-producing constructs were co-transfected with either 4 ng of 129 NLRP1B or 2.5 ng B6 NLRP1B constructs. Twenty-four hours post-transfection, cells were harvested in 1x RIPA lysis buffer with protease inhibitor cocktail (Roche) and immunoblotted with antibodies described below.

Viral stocks and viral infections

CVB3 and EMCV viral stocks were generated by co-transfection of CVB3-Nancy or EMCV-Mengo infectious clone plasmids with a plasmid expressing T7 RNA polymerase (generous gifts from Dr. Julie Pfeiffer, UT Southwestern) as previously described (McCune et al., 2020). Supernatant was harvested, quantified by plaque assay or TCID50 on HEK293T cells, and frozen in aliquots at −80°C.

For viral infections of HEK293T cells, cells were transfected in 24-well plates and infected with 250,000 PFU (MOI = ~1) CVB3 or EMCV or mock infected for the indicated times. For cleavage assays, cells were transfected with 100 ng of the indicated NLRP1 construct and, 24 hr after transfection, cells were harvested and lysed in 1x NuPAGE LDS sample buffer containing 5% β-mercaptoethanol and immunoblotted with antibodies described below. For activation assays, cells were transfected with 4 ng of the indicated NLRP1 construct and 5 ng of ASC, 100 ng of CASP1, 50 ng of IL-1β-V5. Twenty-four hours after transfections, cells were infected with virus (or mock infected) and culture supernatant was collected 8 hr later (32 hr

post-transfection). Culture supernatant was filtered through a 100,000 MWCO centrifugal spin filter (MilliporeSigma, Burlington, MA) for 10 min at 12,000xg to remove infectious virus and IL-1β levels were quantified by HEK-Blue assays (see below).

For viral infections of HaCaT cells, cells were plated in 24-well plates. The next day, cells were infected with 100,000 PFU/well (MOI = ~0.4) CVB3 or EMCV or mock infected. Forty-eight hours after infection, culture supernatant was collected, spin filtered as described above to remove infectious virus, and IL-1β levels were quantified by HEK-Blue assays (see below).

HEK-Blue IL-1β assay

To quantify the levels of bioactive IL-1β released from cells, we employed HEK-Blue IL-1β reporter cells (Invivogen, San Diego, CA). In these cells, binding to IL-1β to the surface receptor IL-1R1 results in the downstream activation of NF-kB and subsequent production of secreted embryonic alkaline phosphatase (SEAP) in a dose-dependent manner (Figure 2.5). SEAP levels are detected using a colorimetric substrate assay, QUANTI-Blue (Invivogen, San Diego, CA) by measuring an increase in absorbance at OD655.

Culture supernatant from inflammasome-reconstituted HEK293T cells or HaCaT cells that had been transfected with 3Cpro or virally infected (see above) was added to HEK-Blue IL-1β reporter cells plated in 96-well format in a total volume of 200 µl per well. On the same plate, serial dilutions of recombinant human IL-1β (Invivogen, San Diego, CA) were added in order to generate a standard curve for each assay. Twenty-four hours later, SEAP levels were assayed by taking 20 µl of the supernatant from HEK-Blue IL-1β reporter cells and adding to 180 µl of QUANTI-Blue colorimetric substrate following the manufacturer's protocol. After incubation at

37°C for 30–60 min, absorbance at OD655 was measured on a BioTek Cytation five plate reader (BioTek Instruments, Winooski, VT) and absolute levels of IL-1β were calculated relative to the standard curve. All assays, beginning with independent transfections or infections, were performed in triplicate.

Immunoblotting and antibodies

Harvested cell pellets were washed with 1X PBS, and lysed with 1x NuPAGE LDS sample buffer containing 5% β-mercaptoethanol at 98C for 10 min. The lysed samples were spun down at 15000 RPM for two minutes, followed by loading into a 4–12% Bis-Tris SDS-PAGE gel (Life Technologies, San Diego, CA) with 1X MOPS buffer (Life Technologies, San Diego, CA) and wet transfer onto a nitrocellulose membrane (Life Technologies, San Diego, CA). Membranes were blocked with PBS-T containing 5% bovine serum albumin (BSA) (Spectrum, New Brunswick, NJ), followed by incubation with primary antibodies for V5 (IL-1β), FLAG (mCherry-fused NLRP1 for protease assays), Myc (NLRP1-Myc for activation assays), HA (viral protease or mouse NLRP1B), β-tubulin, or GAPDH. Membranes were rinsed three times in PBS-T then incubated with the appropriate HRP-conjugated secondary antibodies. Membranes were rinsed again three times in PBS-T and developed with SuperSignal West Pico PLUS Chemiluminescent Substrate (Thermo Fisher Scientific, Carlsbad, CA). The specifications, source, and clone info for antibodies are described in Supplementary file 2.6.

Table 2.1. Key resources table

Reagent type (species) or resource	Designation	Source or reference	Identifiers	Additional information
Gene (*Homo sapiens*)	NLRP1	NCBI	NCBI: NP_127497.1	
Gene (*Mus musculus*)	NLRP1B (129)	NCBI	NCBI: AAZ40510.1	
Gene (*Mus musculus*)	NLRP1B (B6)	NCBI	NCBI: XM_017314698.2	
Cell line (*Homo sapiens*)	HEK293T	ATCC	CRL-3216	
Cell line (*Homo sapiens*)	HEK-Blue IL-1β cells	Invivogen	HKB-IL1B	
Cell line (*Homo sapiens*)	HaCaT (parental)	UC Berkeley Cell Culture Facility		
Cell line (*Homo sapiens*)	HaCaT Cas9 (WT)	This paper		
Cell line (*Homo sapiens*)	HaCaT Cas9 ΔNLRP1 #1 (NLRP1 KO clone #1)	This paper		Exon 5 target (TCCACTGCTTGTACGAGACT)
Cell line (*Homo sapiens*)	HaCaT Cas9 ΔNLRP1 #2 (NLRP1 KO clone #2)	This paper		Exon 2 target (TGTAGGGGAATGAGGGAGAG)
Cell line (*Homo sapiens*)	HaCaT Cas9 ΔCASP1 #1 (CASP1 KO clone #1)	This paper		Exon 2 target (CCAAACAGACAAGGTCCTGA)
Cell line (*Homo sapiens*)	HaCaT Cas9 ΔCASP1 #2 (CASP1 KO clone #2)	This paper		Exon 2 target (CCAAACAGACAAGGTCCTGA)
Recombinant DNA reagent	pcDNA5/FRT/TO (plasmid)	Invitrogen	V652020	
Recombinant DNA reagent	pQCXIP (plasmid)	Takara Bio	631516	
Recombinant DNA reagent	psPAX2 (plasmid)	Addgene	12260	Gift from Dr. Didier Trono
Recombinant DNA reagent	pMD2.G (plasmid)	Addgene	12259	Gift from Dr. Didier Trono
Recombinant DNA reagent	pLB-Cas9 (plasmid)	Addgene	52962	Gift from Dr. Feng Zhang

Table 2.1. Key resources table (continued)

Reagent type (species) or resource	Designation	Source or reference	Identifiers	Additional information
Recombinant DNA reagent	pLentiGuide-Puro (plasmid)	Other		Gift from Dr. Mortiz Gaidt
Recombinant DNA reagent	Inflammasome reconstitution plasmids	PMID: 27926929		Gifts from Dr. Russell Vance: human NLRP1 TEV (NLRP1-TEV2), human ASC, human and mouse CASP1, human IL-1B-V5, mouse IL-1B, and TEV protease
Recombinant DNA reagent	CVB3-Nancy infectious clone plasmid	PMID: 2410905		Gift from Dr. Julie Pfeiffer
Recombinant DNA reagent	EMCV-Mengo infectious clone plasmid	PMID: 2538661		Gift from Dr. Julie Pfeiffer
Commercial assay or kit	QUANTI-Blue assay reagent (for HEK-Blue IL-1b cells)	Invivogen	REP-QBS	Includes necessary reagents for measuring IL-1b release from HEK-Blue-IL-1B reporter cell line
Chemical compound, drug	TransIT-X2	Mirus	MIR 6000	
Chemical compound, drug	MG132	Sigma-Aldrich	M7449	
Chemical compound, drug	MLN4924	APExBIO	B1036	
Antibody	V5-Tag Rabbit mAb	Cell Signaling Technology	13202S	Dilution ratio 1:1000
Antibody	Flag-Tag Mouse mAb	Sigma-Aldrich	F1804	Dilution ratio 1:2000
Antibody	Myc-Tag Rabbit mAb	Cell Signaling Technology	2278S	Dilution ratio 1:1000
Antibody	HA-Tag Rat mAb	Roche	11867423001	Dilution ratio 1:1000
Antibody	GAPDH Rabbit mAb	Cell Signaling Technology	2118S	Dilution ratio 1:2000
Antibody	Goat anti-Rat IgG (H+L) Secondary Antibody, HRP	Thermo Fisher Scientific	31470	Dilution ratio 1:10000
Antibody	Goat anti-Rabbit IgG (H+L) Secondary Antibody, HRP	Biorad	1706515	Dilution ratio 1:10000
Antibody	Goat anti-Mouse IgG (H+L) Secondary Antibody, HRP	Biorad	1706516	Dilution ratio 1:10000

Table 2.1. Key resources table (continued)

Reagent type (species) or resource	Designation	Source or reference	Identifiers	Additional information
Antibody	β-Tubulin Mouse mAb	Sigma-Aldrich	T4026	Dilution ratio 1:2000
Antibody	Goat anti-mouse IL-1β antibody	R&D Systems	AF401SP	Dilution ratio 1:1000
Sequence-based reagent	Oligonucleotides	Other		See Supplementary file 2.5 for list of oligonucleotides used in this study
Software, algorithm	MEME v5.0.3	PMID: 25953851		Motif finder (FIMO)
Software, algorithm	MAFFT 7.309	PMID: 23329690		
Software, algorithm	NetSurfP	PMID: 30785653		http://www.cbs.dtu.dk/services/NetSurfP/ (Original); https://services.healthtech.dtu.dk/service.php?NetSurfP-2.0 (Alternate)
Software, algorithm	Geneious	PMID: 22543367		Neighbor-joining phylogenetic tree
Software, algorithm	BLASTp	PMID: 9254694		

Chapter 2 is published and can be found available in eLife in Immunology and Inflammation

Microbiology and Infectious Disease 2021, including co-authors Brian V. Tsu, Andrew P. Ryan,

Rimjhim Agarwal, Patrick S. Mitchell, Matthew D. Daugherty. I, Christopher Beierschmitt, am

the co-first author of this paper, alongside Brian V. Tsu.

References

Altschul, S. F., Madden, T. L., Schaffer, A. A., Zhang, J., Zhang, Z., Miller, W., & Lipman, D. J. (1997). Gapped BLAST and PSI-BLAST: a new generation of protein database search programs. *Nucleic Acids Res, 25*(17), 3389-3402. doi:10.1093/nar/25.17.3389

Bailey, T. L., Boden, M., Buske, F. A., Frith, M., Grant, C. E., Clementi, L., . . . Noble, W. S. (2009). MEME SUITE: tools for motif discovery and searching. *Nucleic Acids Res, 37*(Web Server issue), W202-208. doi:10.1093/nar/gkp335

Bauernfried, S., Scherr, M. J., Pichlmair, A., Duderstadt, K. E., & Hornung, V. (2020). Human NLRP1 is a sensor for double-stranded RNA. *Science*. doi:10.1126/science.abd0811

Blom, N., Hansen, J., Blaas, D., & Brunak, S. (1996). Cleavage site analysis in picornaviral polyproteins: discovering cellular targets by neural networks. *Protein Sci, 5*(11), 2203-2216. doi:10.1002/pro.5560051107

Boyden, E. D., & Dietrich, W. F. (2006). Nalp1b controls mouse macrophage susceptibility to anthrax lethal toxin. *Nat Genet, 38*(2), 240-244. doi:10.1038/ng1724

Broz, P., & Dixit, V. M. (2016). Inflammasomes: mechanism of assembly, regulation and signalling. *Nat Rev Immunol, 16*(7), 407-420. doi:10.1038/nri.2016.58

Cagliani, R., Forni, D., Tresoldi, C., Pozzoli, U., Filippi, G., Rainone, V., . . . Sironi, M. (2014). RIG-I-like receptors evolved adaptively in mammals, with parallel evolution at LGP2 and RIG-I. *J Mol Biol, 426*(6), 1351-1365. doi:10.1016/j.jmb.2013.10.040

Chavarria-Smith, J., Mitchell, P. S., Ho, A. M., Daugherty, M. D., & Vance, R. E. (2016). Functional and Evolutionary Analyses Identify Proteolysis as a General Mechanism for NLRP1 Inflammasome Activation. *PLoS Pathog, 12*(12), e1006052. doi:10.1371/journal.ppat.1006052

Chavarria-Smith, J., & Vance, R. E. (2013). Direct proteolytic cleavage of NLRP1B is necessary and sufficient for inflammasome activation by anthrax lethal factor. *PLoS Pathog, 9*(6), e1003452. doi:10.1371/journal.ppat.1003452

Chemes, L. B., de Prat-Gay, G., & Sanchez, I. E. (2015). Convergent evolution and mimicry of protein linear motifs in host-pathogen interactions. *Curr Opin Struct Biol, 32*, 91-101. doi:10.1016/j.sbi.2015.03.004

Chui, A. J., Okondo, M. C., Rao, S. D., Gai, K., Griswold, A. R., Johnson, D. C., . . . Bachovchin, D. A. (2019). N-terminal degradation activates the NLRP1B inflammasome. *Science, 364*(6435), 82-85. doi:10.1126/science.aau1208

Croft, S. N., Walker, E. J., & Ghildyal, R. (2018). Human Rhinovirus 3C protease cleaves RIPK1, concurrent with caspase 8 activation. *Sci Rep, 8*(1), 1569. doi:10.1038/s41598-018-19839-4

Cui, H., Tsuda, K., & Parker, J. E. (2015). Effector-triggered immunity: from pathogen perception to robust defense. *Annu Rev Plant Biol, 66*, 487-511. doi:10.1146/annurev-arplant-050213-040012

D'Osualdo, A., Anania, V. G., Yu, K., Lill, J. R., Kaufman, R. J., Matsuzawa, S., & Reed, J. C. (2015). Transcription Factor ATF4 Induces NLRP1 Inflammasome Expression during Endoplasmic Reticulum Stress. *PLoS One, 10*(6), e0130635. doi:10.1371/journal.pone.0130635

D'Osualdo, A., Weichenberger, C. X., Wagner, R. N., Godzik, A., Wooley, J., & Reed, J. C. (2011). CARD8 and NLRP1 undergo autoproteolytic processing through a ZU5-like domain. *PLoS One, 6*(11), e27396. doi:10.1371/journal.pone.0027396

Daugherty, M. D., & Malik, H. S. (2012). Rules of engagement: molecular insights from host-virus arms races. *Annu Rev Genet, 46*, 677-700. doi:10.1146/annurev-genet-110711-155522

Drutman, S. B., Haerynck, F., Zhong, F. L., Hum, D., Hernandez, N. J., Belkaya, S., . . . Casanova, J. L. (2019). Homozygous NLRP1 gain-of-function mutation in siblings with a

syndromic form of recurrent respiratory papillomatosis. *Proc Natl Acad Sci U S A, 116*(38), 19055-19063. doi:10.1073/pnas.1906184116

Elde, N. C., & Malik, H. S. (2009). The evolutionary conundrum of pathogen mimicry. *Nat Rev Microbiol, 7*(11), 787-797. doi:10.1038/nrmicro2222

Evavold, C. L., & Kagan, J. C. (2019). Inflammasomes: Threat-Assessment Organelles of the Innate Immune System. *Immunity, 51*(4), 609-624. doi:10.1016/j.immuni.2019.08.005

Fan, X., Li, X., Zhou, Y., Mei, M., Liu, P., Zhao, J., . . . Yi, L. (2020). Quantitative Analysis of the Substrate Specificity of Human Rhinovirus 3C Protease and Exploration of Its Substrate Recognition Mechanisms. *ACS Chem Biol, 15*(1), 63-73. doi:10.1021/acschembio.9b00539

Finger, J. N., Lich, J. D., Dare, L. C., Cook, M. N., Brown, K. K., Duraiswami, C., . . . Gough, P. J. (2012). Autolytic proteolysis within the function to find domain (FIIND) is required for NLRP1 inflammasome activity. *J Biol Chem, 287*(30), 25030-25037. doi:10.1074/jbc.M112.378323

Fischer, N. L., Naseer, N., Shin, S., & Brodsky, I. E. (2020). Publisher Correction: Effector-triggered immunity and pathogen sensing in metazoans. *Nat Microbiol, 5*(3), 528. doi:10.1038/s41564-020-0682-4

Frew, B. C., Joag, V. R., & Mogridge, J. (2012). Proteolytic processing of Nlrp1b is required for inflammasome activity. *PLoS Pathog, 8*(4), e1002659. doi:10.1371/journal.ppat.1002659

Grandemange, S., Sanchez, E., Louis-Plence, P., Tran Mau-Them, F., Bessis, D., Coubes, C., . . . Genevieve, D. (2017). A new autoinflammatory and autoimmune syndrome associated with NLRP1 mutations: NAIAD (NLRP1-associated autoinflammation with arthritis and dyskeratosis). *Ann Rheum Dis, 76*(7), 1191-1198. doi:10.1136/annrheumdis-2016-210021

Grant, C. E., Bailey, T. L., & Noble, W. S. (2011). FIMO: scanning for occurrences of a given motif. *Bioinformatics, 27*(7), 1017-1018. doi:10.1093/bioinformatics/btr064

Greaney, A. J., Portley, M. K., O'Mard, D., Crown, D., Maier, N. K., Mendenhall, M. A., . . . Moayeri, M. (2020). Frontline Science: Anthrax lethal toxin-induced, NLRP1-mediated IL-1beta release is a neutrophil and PAD4-dependent event. *J Leukoc Biol*. doi:10.1002/JLB.4HI0320-028R

Hagai, T., Azia, A., Babu, M. M., & Andino, R. (2014). Use of host-like peptide motifs in viral proteins is a prevalent strategy in host-virus interactions. *Cell Rep, 7*(5), 1729-1739. doi:10.1016/j.celrep.2014.04.052

Hancks, D. C., Hartley, M. K., Hagan, C., Clark, N. L., & Elde, N. C. (2015). Overlapping Patterns of Rapid Evolution in the Nucleic Acid Sensors cGAS and OAS1 Suggest a Common Mechanism of Pathogen Antagonism and Escape. *PLoS Genet, 11*(5), e1005203. doi:10.1371/journal.pgen.1005203

Herlin, T., Jorgensen, S. E., Host, C., Mitchell, P. S., Christensen, M. H., Laustsen, M., . . . Mogensen, T. H. (2019). Autoinflammatory disease with corneal and mucosal dyskeratosis caused by a novel NLRP1 variant. *Rheumatology (Oxford)*. doi:10.1093/rheumatology/kez612

Huang, L., Liu, Q., Zhang, L., Zhang, Q., Hu, L., Li, C., . . . Weng, C. (2015). Encephalomyocarditis Virus 3C Protease Relieves TRAF Family Member-associated NF-kappaB Activator (TANK) Inhibitory Effect on TRAF6-mediated NF-kappaB Signaling through Cleavage of TANK. *J Biol Chem, 290*(46), 27618-27632. doi:10.1074/jbc.M115.660761

Jagdeo, J. M., Dufour, A., Klein, T., Solis, N., Kleifeld, O., Kizhakkedathu, J., . . . Jan, E. (2018). N-Terminomics TAILS Identifies Host Cell Substrates of Poliovirus and Coxsackievirus B3 3C Proteinases That Modulate Virus Infection. *J Virol, 92*(8). doi:10.1128/JVI.02211-17

Janeway, C. A., Jr. (1989). Approaching the asymptote? Evolution and revolution in immunology. *Cold Spring Harb Symp Quant Biol, 54 Pt 1*, 1-13. doi:10.1101/sqb.1989.054.01.003

Jones, J. D., Vance, R. E., & Dangl, J. L. (2016). Intracellular innate immune surveillance devices in plants and animals. *Science, 354*(6316). doi:10.1126/science.aaf6395

Karczewski, K. J., Francioli, L. C., Tiao, G., Cummings, B. B., Alfoldi, J., Wang, Q., . . . MacArthur, D. G. (2020). The mutational constraint spectrum quantified from variation in 141,456 humans. *Nature, 581*(7809), 434-443. doi:10.1038/s41586-020-2308-7

Katoh, K., & Standley, D. M. (2013). MAFFT multiple sequence alignment software version 7: improvements in performance and usability. *Mol Biol Evol, 30*(4), 772-780. doi:10.1093/molbev/mst010

Kaushal, V., Dye, R., Pakavathkumar, P., Foveau, B., Flores, J., Hyman, B., . . . LeBlanc, A. C. (2015). Neuronal NLRP1 inflammasome activation of Caspase-1 coordinately regulates inflammatory interleukin-1-beta production and axonal degeneration-associated Caspase-6 activation. *Cell Death Differ, 22*(10), 1676-1686. doi:10.1038/cdd.2015.16

Kearse, M., Moir, R., Wilson, A., Stones-Havas, S., Cheung, M., Sturrock, S., . . . Drummond, A. (2012). Geneious Basic: an integrated and extendable desktop software platform for the organization and analysis of sequence data. *Bioinformatics, 28*(12), 1647-1649. doi:10.1093/bioinformatics/bts199

Kimura, M. (1983). *The neutral theory of molecular evolution*. Cambridge Cambridgeshire ; New York: Cambridge University Press.

Klausen, M. S., Jespersen, M. C., Nielsen, H., Jensen, K. K., Jurtz, V. I., Sonderby, C. K., . . . Marcatili, P. (2019). NetSurfP-2.0: Improved prediction of protein structural features by integrated deep learning. *Proteins, 87*(6), 520-527. doi:10.1002/prot.25674

Kummer, J. A., Broekhuizen, R., Everett, H., Agostini, L., Kuijk, L., Martinon, F., . . . Tschopp, J. (2007). Inflammasome components NALP 1 and 3 show distinct but separate expression profiles in human tissues suggesting a site-specific role in the inflammatory response. *J Histochem Cytochem, 55*(5), 443-452. doi:10.1369/jhc.6A7101.2006

Kuriakose, T., & Kanneganti, T. D. (2019). Pyroptosis in Antiviral Immunity. *Curr Top Microbiol Immunol*. doi:10.1007/82_2019_189

Laitinen, O. H., Svedin, E., Kapell, S., Nurminen, A., Hytonen, V. P., & Flodstrom-Tullberg, M. (2016). Enteroviral proteases: structure, host interactions and pathogenicity. *Rev Med Virol, 26*(4), 251-267. doi:10.1002/rmv.1883

Lei, X., Zhang, Z., Xiao, X., Qi, J., He, B., & Wang, J. (2017). Enterovirus 71 Inhibits Pyroptosis through Cleavage of Gasdermin D. *J Virol, 91*(18). doi:10.1128/JVI.01069-17

Levinsohn, J. L., Newman, Z. L., Hellmich, K. A., Fattah, R., Getz, M. A., Liu, S., . . . Moayeri, M. (2012). Anthrax lethal factor cleavage of Nlrp1 is required for activation of the inflammasome. *PLoS Pathog, 8*(3), e1002638. doi:10.1371/journal.ppat.1002638

Martinon, F., Burns, K., & Tschopp, J. (2002). The inflammasome: a molecular platform triggering activation of inflammatory caspases and processing of proIL-beta. *Mol Cell, 10*(2), 417-426. doi:10.1016/s1097-2765(02)00599-3

McCune, B. T., Lanahan, M. R., tenOever, B. R., & Pfeiffer, J. K. (2020). Rapid Dissemination and Monopolization of Viral Populations in Mice Revealed Using a Panel of Barcoded Viruses. *J Virol, 94*(2). doi:10.1128/JVI.01590-19

Meyerson, N. R., & Sawyer, S. L. (2011). Two-stepping through time: mammals and viruses. *Trends Microbiol, 19*(6), 286-294. doi:10.1016/j.tim.2011.03.006

Mitchell, P. S., Sandstrom, A., & Vance, R. E. (2019). The NLRP1 inflammasome: new mechanistic insights and unresolved mysteries. *Curr Opin Immunol, 60*, 37-45. doi:10.1016/j.coi.2019.04.015

Moayeri, M., Crown, D., Newman, Z. L., Okugawa, S., Eckhaus, M., Cataisson, C., . . . Leppla, S. H. (2010). Inflammasome sensor Nlrp1b-dependent resistance to anthrax is mediated by caspase-1, IL-1 signaling and neutrophil recruitment. *PLoS Pathog, 6*(12), e1001222. doi:10.1371/journal.ppat.1001222

Moayeri, M., Sastalla, I., & Leppla, S. H. (2012). Anthrax and the inflammasome. *Microbes Infect, 14*(5), 392-400. doi:10.1016/j.micinf.2011.12.005

Mukherjee, A., Morosky, S. A., Delorme-Axford, E., Dybdahl-Sissoko, N., Oberste, M. S., Wang, T., & Coyne, C. B. (2011). The coxsackievirus B 3C protease cleaves MAVS and TRIF to attenuate host type I interferon and apoptotic signaling. *PLoS Pathog, 7*(3), e1001311. doi:10.1371/journal.ppat.1001311

O'Donoghue, A. J., Eroy-Reveles, A. A., Knudsen, G. M., Ingram, J., Zhou, M., Statnekov, J. B., . . . Craik, C. S. (2012). Global identification of peptidase specificity by multiplex substrate profiling. *Nat Methods, 9*(11), 1095-1100. doi:10.1038/nmeth.2182

Okondo, M. C., Rao, S. D., Taabazuing, C. Y., Chui, A. J., Poplawski, S. E., Johnson, D. C., & Bachovchin, D. A. (2018). Inhibition of Dpp8/9 Activates the Nlrp1b Inflammasome. *Cell Chem Biol, 25*(3), 262-267 e265. doi:10.1016/j.chembiol.2017.12.013

Patel, M. R., Loo, Y. M., Horner, S. M., Gale, M., Jr., & Malik, H. S. (2012). Convergent evolution of escape from hepaciviral antagonism in primates. *PLoS Biol, 10*(3), e1001282. doi:10.1371/journal.pbio.1001282

Pickett, B. E., Greer, D. S., Zhang, Y., Stewart, L., Zhou, L., Sun, G., . . . Scheuermann, R. H. (2012). Virus pathogen database and analysis resource (ViPR): a comprehensive bioinformatics database and analysis resource for the coronavirus research community. *Viruses, 4*(11), 3209-3226. doi:10.3390/v4113209

Qian, S., Fan, W., Liu, T., Wu, M., Zhang, H., Cui, X., . . . Qian, P. (2017). Seneca Valley Virus Suppresses Host Type I Interferon Production by Targeting Adaptor Proteins MAVS, TRIF, and TANK for Cleavage. *J Virol, 91*(16). doi:10.1128/JVI.00823-17

Rathinam, V. A., & Fitzgerald, K. A. (2016). Inflammasome Complexes: Emerging Mechanisms and Effector Functions. *Cell, 165*(4), 792-800. doi:10.1016/j.cell.2016.03.046

Rathinam, V. A., Vanaja, S. K., & Fitzgerald, K. A. (2012). Regulation of inflammasome signaling. *Nat Immunol, 13*(4), 333-342. doi:10.1038/ni.2237

Robinson, K. S., Teo, D. E. T., Tan, K. S., Toh, G. A., Ong, H. H., Lim, C. K., . . . Reversade, B. (2020). Enteroviral 3C protease activates the human NLRP1 inflammasome in airway epithelia. *Science, 370*(6521). doi:10.1126/science.aay2002

Sandstrom, A., Mitchell, P. S., Goers, L., Mu, E. W., Lesser, C. F., & Vance, R. E. (2019). Functional degradation: A mechanism of NLRP1 inflammasome activation by diverse pathogen enzymes. *Science, 364*(6435). doi:10.1126/science.aau1330

Sanjana, N. E., Shalem, O., & Zhang, F. (2014). Improved vectors and genome-wide libraries for CRISPR screening. *Nat Methods, 11*(8), 783-784. doi:10.1038/nmeth.3047

Schechter, I., & Berger, A. (1967). On the size of the active site in proteases. I. Papain. *Biochem Biophys Res Commun, 27*(2), 157-162. doi:10.1016/s0006-291x(67)80055-x

Schmidt, T., Schmid-Burgk, J. L., & Hornung, V. (2015). Synthesis of an arrayed sgRNA library targeting the human genome. *Sci Rep, 5*, 14987. doi:10.1038/srep14987

Sironi, M., Cagliani, R., Forni, D., & Clerici, M. (2015). Evolutionary insights into host-pathogen interactions from mammalian sequence data. *Nat Rev Genet, 16*(4), 224-236. doi:10.1038/nrg3905

Soler, V. J., Tran-Viet, K. N., Galiacy, S. D., Limviphuvadh, V., Klemm, T. P., St Germain, E., . . . Young, T. L. (2013). Whole exome sequencing identifies a mutation for a novel form of corneal intraepithelial dyskeratosis. *J Med Genet, 50*(4), 246-254. doi:10.1136/jmedgenet-2012-101325

Solomon, T., Lewthwaite, P., Perera, D., Cardosa, M. J., McMinn, P., & Ooi, M. H. (2010). Virology, epidemiology, pathogenesis, and control of enterovirus 71. *Lancet Infect Dis, 10*(11), 778-790. doi:10.1016/S1473-3099(10)70194-8

Spel, L., & Martinon, F. (2020). Detection of viruses by inflammasomes. *Curr Opin Virol, 46*, 59-64. doi:10.1016/j.coviro.2020.10.001

Stabell, A. C., Meyerson, N. R., Gullberg, R. C., Gilchrist, A. R., Webb, K. J., Old, W. M., . . . Sawyer, S. L. (2018). Dengue viruses cleave STING in humans but not in nonhuman primates, their presumed natural reservoir. *Elife, 7*. doi:10.7554/eLife.31919

Sun, D., Chen, S., Cheng, A., & Wang, M. (2016). Roles of the Picornaviral 3C Proteinase in the Viral Life Cycle and Host Cells. *Viruses, 8*(3), 82. doi:10.3390/v8030082

Taabazuing, C. Y., Griswold, A. R., & Bachovchin, D. A. (2020). The NLRP1 and CARD8 inflammasomes. *Immunol Rev*. doi:10.1111/imr.12884

Tan, J., George, S., Kusov, Y., Perbandt, M., Anemuller, S., Mesters, J. R., . . . Hilgenfeld, R. (2013). 3C protease of enterovirus 68: structure-based design of Michael acceptor inhibitors and their broad-spectrum antiviral effects against picornaviruses. *J Virol, 87*(8), 4339-4351. doi:10.1128/JVI.01123-12

Tenthorey, J. L., Kofoed, E. M., Daugherty, M. D., Malik, H. S., & Vance, R. E. (2014). Molecular basis for specific recognition of bacterial ligands by NAIP/NLRC4 inflammasomes. *Mol Cell, 54*(1), 17-29. doi:10.1016/j.molcel.2014.02.018

Terra, J. K., Cote, C. K., France, B., Jenkins, A. L., Bozue, J. A., Welkos, S. L., . . . Bradley, K. A. (2010). Cutting edge: resistance to Bacillus anthracis infection mediated by a lethal toxin sensitive allele of Nalp1b/Nlrp1b. *J Immunol, 184*(1), 17-20. doi:10.4049/jimmunol.0903114

Tian, X., Pascal, G., & Monget, P. (2009). Evolution and functional divergence of NLRP genes in mammalian reproductive systems. *BMC Evol Biol, 9*, 202. doi:10.1186/1471-2148-9-202

Timms, R. T., Zhang, Z., Rhee, D. Y., Harper, J. W., Koren, I., & Elledge, S. J. (2019). A glycine-specific N-degron pathway mediates the quality control of protein N-myristoylation. *Science, 365*(6448). doi:10.1126/science.aaw4912

Ting, J. P., Lovering, R. C., Alnemri, E. S., Bertin, J., Boss, J. M., Davis, B. K., . . . Ward, P. A. (2008). The NLR gene family: a standard nomenclature. *Immunity, 28*(3), 285-287. doi:10.1016/j.immuni.2008.02.005

Vance, R. E., Isberg, R. R., & Portnoy, D. A. (2009). Patterns of pathogenesis: discrimination of pathogenic and nonpathogenic microbes by the innate immune system. *Cell Host Microbe, 6*(1), 10-21. doi:10.1016/j.chom.2009.06.007

Wang, C., Fung, G., Deng, H., Jagdeo, J., Mohamud, Y., Xue, Y. C., . . . Luo, H. (2019). NLRP3 deficiency exacerbates enterovirus infection in mice. *FASEB J, 33*(1), 942-952. doi:10.1096/fj.201800301RRR

Wang, D., Fang, L., Li, K., Zhong, H., Fan, J., Ouyang, C., . . . Xiao, S. (2012). Foot-and-mouth disease virus 3C protease cleaves NEMO to impair innate immune signaling. *J Virol, 86*(17), 9311-9322. doi:10.1128/JVI.00722-12

Wang, D., Fang, L., Wei, D., Zhang, H., Luo, R., Chen, H., . . . Xiao, S. (2014). Hepatitis A virus 3C protease cleaves NEMO to impair induction of beta interferon. *J Virol, 88*(17), 10252-10258. doi:10.1128/JVI.00869-14

Wang, H., Lei, X., Xiao, X., Yang, C., Lu, W., Huang, Z., . . . Wang, J. (2015). Reciprocal Regulation between Enterovirus 71 and the NLRP3 Inflammasome. *Cell Rep, 12*(1), 42-48. doi:10.1016/j.celrep.2015.05.047

Wang, Y., Qin, Y., Wang, T., Chen, Y., Lang, X., Zheng, J., . . . Zhong, Z. (2018). Pyroptosis induced by enterovirus 71 and coxsackievirus B3 infection affects viral replication and host response. *Sci Rep, 8*(1), 2887. doi:10.1038/s41598-018-20958-1

Wen, W., Yin, M., Zhang, H., Liu, T., Chen, H., Qian, P., . . . Li, X. (2019). Seneca Valley virus 2C and 3C inhibit type I interferon production by inducing the degradation of RIG-I. *Virology, 535*, 122-129. doi:10.1016/j.virol.2019.06.017

Wickliffe, K. E., Leppla, S. H., & Moayeri, M. (2008). Killing of macrophages by anthrax lethal toxin: involvement of the N-end rule pathway. *Cell Microbiol, 10*(6), 1352-1362. doi:10.1111/j.1462-5822.2008.01131.x

Xiang, Z., Li, L., Lei, X., Zhou, H., Zhou, Z., He, B., & Wang, J. (2014). Enterovirus 68 3C protease cleaves TRIF to attenuate antiviral responses mediated by Toll-like receptor 3. *J Virol, 88*(12), 6650-6659. doi:10.1128/JVI.03138-13

Xiang, Z., Liu, L., Lei, X., Zhou, Z., He, B., & Wang, J. (2016). 3C Protease of Enterovirus D68 Inhibits Cellular Defense Mediated by Interferon Regulatory Factor 7. *J Virol, 90*(3), 1613-1621. doi:10.1128/JVI.02395-15

Xiao, X., Qi, J., Lei, X., & Wang, J. (2019). Interactions Between Enteroviruses and the Inflammasome: New Insights Into Viral Pathogenesis. *Front Microbiol, 10*, 321. doi:10.3389/fmicb.2019.00321

Xu, H., Shi, J., Gao, H., Liu, Y., Yang, Z., Shao, F., & Dong, N. (2019). The N-end rule ubiquitin ligase UBR2 mediates NLRP1B inflammasome activation by anthrax lethal toxin. *EMBO J, 38*(13), e101996. doi:10.15252/embj.2019101996

Zaragoza, C., Saura, M., Padalko, E. Y., Lopez-Rivera, E., Lizarbe, T. R., Lamas, S., & Lowenstein, C. J. (2006). Viral protease cleavage of inhibitor of kappaBalpha triggers host cell apoptosis. *Proc Natl Acad Sci U S A, 103*(50), 19051-19056. doi:10.1073/pnas.0606019103

Zell, R. (2018). *Picornaviridae*-the ever-growing virus family. *Arch Virol, 163*(2), 299-317. doi:10.1007/s00705-017-3614-8

Zhong, F. L., Mamai, O., Sborgi, L., Boussofara, L., Hopkins, R., Robinson, K., . . . Reversade, B. (2016). Germline NLRP1 Mutations Cause Skin Inflammatory and Cancer Susceptibility Syndromes via Inflammasome Activation. *Cell, 167*(1), 187-202 e117. doi:10.1016/j.cell.2016.09.001

Zhong, F. L., Robinson, K., Teo, D. E. T., Tan, K. Y., Lim, C., Harapas, C. R., . . . Reversade, B. (2018). Human DPP9 represses NLRP1 inflammasome and protects against autoinflammatory diseases via both peptidase activity and FIIND domain binding. *J Biol Chem, 293*(49), 18864-18878. doi:10.1074/jbc.RA118.004350

Chapter 3: Antiviral function and viral antagonism of the rapidly evolving dynein activating adaptor NINL

Abstract

Viruses interact with the intracellular transport machinery to promote viral replication. Such host-virus interactions can drive host gene adaptation, leaving signatures of pathogen-driven evolution in host genomes. Here we leverage these genetic signatures to identify the dynein activating adaptor, ninein-like (NINL), as a critical component in the antiviral innate immune response and as a target of viral antagonism. Unique among genes encoding for dynein subunits, subunits of its co-factor dynactin, and dynein activating adaptors, NINL has evolved under recurrent positive selection, specifically in its carboxy-terminal cargo binding region. Consistent with a role for NINL in host immunity, NINL knockout cells are more permissive to viral replication as a result of a severe attenuation of interferon stimulated gene (ISG) production following interferon treatment. Moreover, we show that proteases encoded by diverse picornaviruses and coronaviruses cleave and disrupt NINL function in a host- and virus-specific manner. Our work reveals the importance of NINL in the antiviral response and the utility of using signatures of host-virus conflicts to uncover new components of antiviral immunity and targets of viral antagonism.

Introduction

Viruses interact directly with host proteins at nearly every step of their life cycle. Such molecular interactions can either benefit the host (*e.g.,* immune recognition) or the virus (*e.g.,* viral co-option of host machinery or viral antagonism of host immunity) and are thus critical determinants of the outcome of a viral infection. These competing interests can drive genetic innovation on both sides of the host-virus conflict, resulting in signatures of recurrent adaptation that have been described as molecular 'arms races' (Daugherty and Malik, 2012; Duggal and

Emerman, 2012; Tenthorey et al., 2022). Indeed, many host antiviral factors that directly interact with viral proteins have been shown to display signatures of recurrent positive selection throughout their evolution, and genetic variation in these host-virus interactions shapes species-specific susceptibility to circulating and emerging pathogens (Meyerson and Sawyer, 2011; Rothenburg and Brennan, 2020). These data suggest that there is great potential to use evolutionary signatures of rapid evolution not only as an approach to more deeply understand known host-virus conflicts but also as a means to discover new proteins engaged in viral interactions (Daugherty and Malik, 2012). Compellingly, it is estimated that around 30% of all adaptive amino acid changes in humans result from viral selective pressure (Enard et al., 2016; Enard and Petrov, 2018), suggesting that many host-virus conflicts remain undescribed.

One potential source of host-virus conflicts is over the active transport of macromolecules within the cell. The relatively large size of eukaryotic cells, coupled with the density of macromolecules in the cytoplasm, limits the effectiveness of diffusion to localize and transport large intracellular components, such as organelles, membrane vesicles, RNAs, and protein complexes (Luby-Phelps, 2000; Seksek et al., 1997). Eukaryotic cells overcome this problem by actively transporting large intracellular cargos using dynein and kinesin motors, which move on microtubules in opposite directions. Aspects of viral infection, viral replication, and the host immune response all require microtubule-based transport. For example, viruses co-opt the microtubule cytoskeleton for cell entry, transport of viral components to sites of replication, remodeling of cellular compartments, and viral egress (Brandenburg and Zhuang, 2007; Dodding and Way, 2011; Döhner et al., 2005; Radtke et al., 2006). Similarly, the host adaptive and innate immune responses to infection require movement of signaling components,

transport of endocytic and exocytic vesicles, organelle recycling and cellular remodeling, all of which require the microtubule-based trafficking machinery (Ilan-Ber and Ilan, 2019; Kast and Dominguez, 2017; Man and Kanneganti, 2016; Mostowy and Shenoy, 2015). Despite the clear role of microtubule-based transport in both aiding and inhibiting viral replication, the degree to which host-virus conflicts shape the basic biology of this machinery is poorly understood.

Here, we set out to determine if there were undescribed genetic conflicts between viruses and the intracellular transport machinery that could lead to a greater understanding of the role of this machinery in viral replication and the immune response. We focused on the dynein transport machinery, which moves dozens of cellular cargos towards microtubule minus-ends (generally anchored to centrosomes near the nucleus). In human cells, only one dynein motor-containing gene, cytoplasmic dynein-1 (*DYNC1H1*), is responsible for long-distance transport in the cytoplasm. Current evidence suggests that the active cytoplasmic dynein-1 complex (dynein hereafter) is composed of dynein subunits, the dynactin complex, and one of a growing list of activating adaptors (McKenney et al., 2014; Schlager et al., 2014). In addition to being required for robust processive motility, activating adaptors provide cargo specificity for dynein (Olenick and Holzbaur, 2019; Reck-Peterson et al., 2018). However, the biological functions and cargo preferences for most activating adaptors remain unknown.

We now show that NINL is unique among dynein, dynactin, and activating adaptor genes, showing signs of recurrent positive selection. NINL knockout (KO) cells show increased susceptibility to viral infections. Our data suggest that this is due to an attenuation of the interferon response and a dramatic decrease in interferon-stimulated gene (ISG) production.

Further, we show that various picornavirus and coronavirus proteases specifically cleave NINL, suggesting a mechanism of viral antagonism that we show is capable of severing dynein from a cargo. Our results reveal a novel function for NINL and a new means by which viruses antagonize the innate immune response. More broadly, our results implicate a component of the dynein transport machinery in host-virus conflicts and establish the utility of our evolution-guided approach.

Results

The dynein activating adaptor, NINL, has evolved under positive selection

Active dynein complexes in human cells are large, multi-subunit machines. The dynein/dynactin complex is composed of two copies of the ATPase-containing heavy chain, two copies of five additional dynein chains, the 23-subunit dynactin complex, and an activating adaptor (Olenick and Holzbaur, 2019; Reck-Peterson et al., 2018) (Figure 3.1A). To generate hypotheses about potential conflicts between the dynein machinery and pathogens, we analyzed all of the dynein and dynactin subunits and the 13 activating adaptors that were known at the time of this analysis for signatures of positive selection across simian primate evolution using maximum likelihood methods. Each human dynein gene was compared to orthologs in 13-19 diverse simian primates, and a gene-wide dN/dS (also known as omega) value was calculated, which compares the gene-wide rate of nonsynonymous changes (i.e., amino acid altering) to the rate of synonymous (i.e., silent) changes. Consistent with the critical role of dynein-mediated intracellular transport, most genes we analyzed were extremely well conserved with dN/dS values of <0.1, while one dynein activating adaptor, NINL, showed an elevated rate compared to the rest (Figure 3.1B and Supplementary File 3.1). To determine whether any genes had

individual codons that have been subject to recurrent positive selection, we performed codon-based analyses of positive selection. Consistent with their low dN/dS values, we observed that most dynein, dynactin and activating adaptor genes showed no evidence for positive selection (p-value > 0.05). In contrast, NINL showed strong evidence for recurrent positive selection in primates consistent with previous data (Gordon et al., 2020) (Figure 3.1B and Supplementary File 3.1), establishing the possibility that NINL could be at the interface of a host-pathogen interaction.

In order to attribute the signatures of positive selection in NINL to known functional domains within NINL, we performed additional analyses to identify codons that have evolved under positive selection using three independent methods, PAML, FEL, and MEME (Kosakovsky Pond and Frost, 2005; Murrell et al., 2012; Yang, 2007). We identified 30 codons that show signatures of positive selection based on one or more of these methods (Figure 3.1C and Supplementary File 3.2). Most (24 of 30) of these codons are excluded from the known dynein/dynactin binding region of NINL (residues 1-702) (Redwine et al., 2017) and instead are located in the carboxy-terminal region of the protein that is expected to interact with cargo (residues 703-1382). When we analyzed individual domains on their own, we found no evidence for positive selection in the amino-terminus alone, while the carboxy-terminus retained a significant signature of positive selection (Figure 3.1D and Supplementary File 3.3). Taken together, our evolutionary analyses indicate that NINL stands out among components of the

active dynein complex by having evolved under recurrent positive selection in primates.
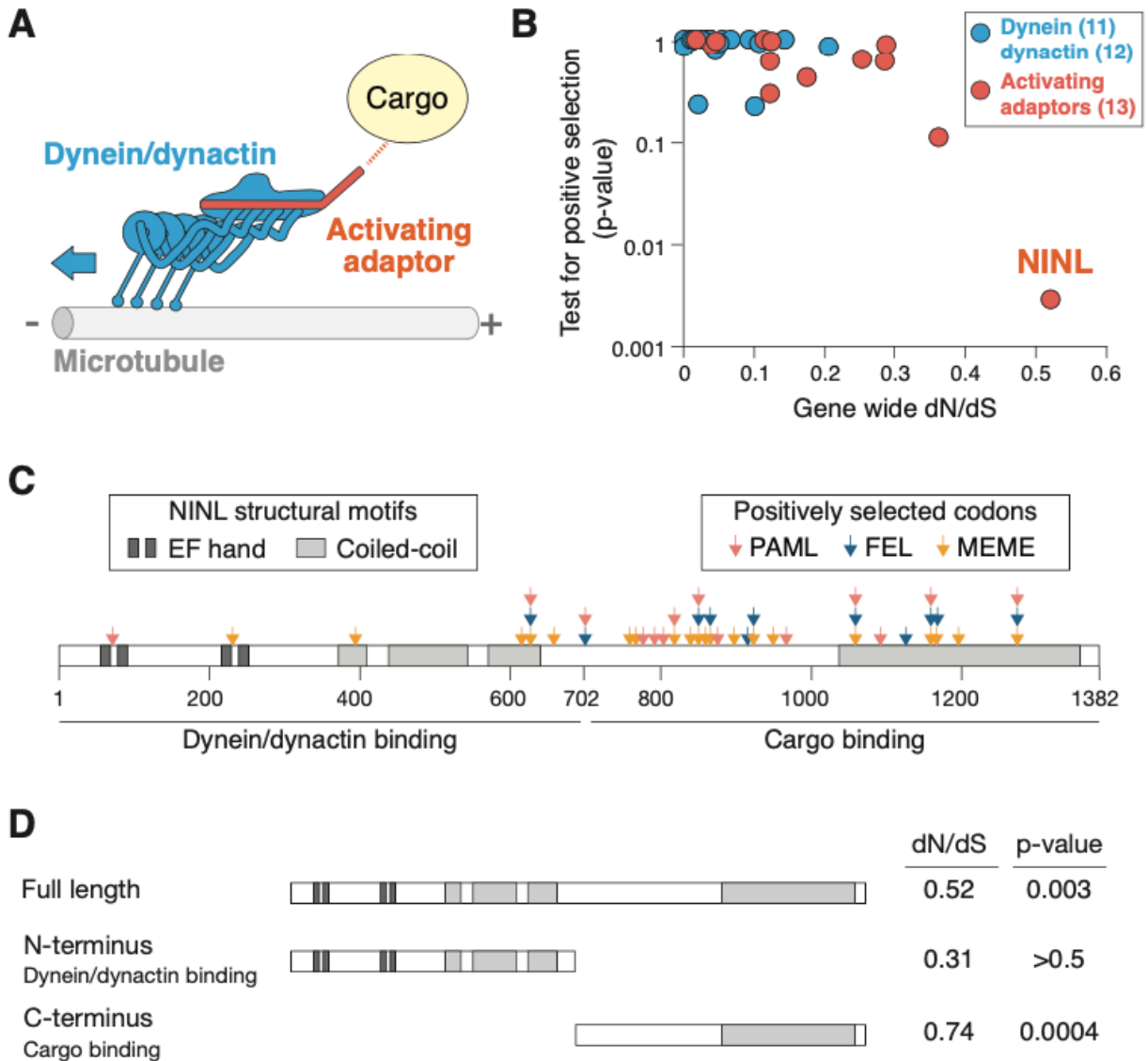
Figure 3.1. The dynein activating adaptor, NINL, has evolved under positive selection in primates. (**A**) A schematic of the cytoplasmic dynein-1 transport machinery, which includes dynein and dynactin subunits (blue) and an activating adaptor (orange). Dynein moves toward the minus end of microtubules (blue arrow). (**B**) A scatterplot displaying evolutionary signatures of selection for 23 dynein and dynactin genes (blue) and 13 dynein activating adaptor genes (orange). The x-axis displays the rate of non-synonymous changes (dN) divided by the rate of synonymous changes (dS) in the coding sequence across primate evolution. The y-axis displays the calculated probability of the gene having evolved under positive selection using PAML. Complete data are found in Supplemental File 3.1. (**C**) A schematic of human NINL isoform 1 with EF hand (dark grey) and coiled-coil (light grey) domains shown. The amino-terminal dynein/dynactin binding region and the carboxy-terminal candidate cargo binding domains are indicated. Sites of positive selection predicted by three evolutionary models are shown as colored arrows: PAML (light red), FEL (blue), MEME (orange). A full list of sites and their calculated probabilities are shown in Supplemental File 3.2. (**D**) Full-length NINL, the dynein/dynactin binding amino-terminus of NINL and the candidate cargo binding carboxy-terminus of NINL were analyzed for signatures of positive selection. Select dN/dS and p-values are shown, with additional evolutionary data in Supplemental Files 3.2 and 3.3.

Viral replication is increased in cells lacking NINL

Our observation that NINL displays a signature of positive selection that is unique among dynein components led us to hypothesize that NINL may be co-opted by viruses for viral replication or may play a role in the immune response to viruses. To evaluate this hypothesis, we generated a human A549 cell line that lacked NINL (NINL KO) (Figure 3.2A, Figure 3.3A, B). At a qualitative level, these cells appeared to have a normal microtubule architecture and centrosomes (Figure 3.3A). In parallel, we generated cells that lacked ninein (NIN KO) (Figure 3.2A, Figure 3.3C), the closest human paralog to NINL, which shares a similar domain architecture with NINL and is also a dynein activator adaptor (Redwine et al., 2017), but shows no evidence for positive selection (Figure 3.1B and Supplemental File 3.1). To evaluate the effect that NINL or NIN have on viral replication or the innate immune response to viral infection, we infected WT, NINL KO, or NIN KO A549 cells with a model enveloped negative-sense single-stranded RNA (-ssRNA) virus, vesicular stomatitis virus (VSV), with and without pretreatment with the antiviral signaling cytokine interferon alpha (IFNα). Consistent with the strong antiviral effect of IFNα, we observed a >100-fold decrease in viral replication in WT and NIN cells that had been pretreated with IFNα (Figure 3.2B). In contrast, we observed that the effect of IFNα was significantly attenuated in NINL KO cells, where we found that IFNα pretreatment reduced VSV replication <10-fold (Figure 3.2B). To attribute the changes in viral replication to the absence of NINL rather than off-target perturbations or cell-line specific effects, we generated additional NINL KO cell lines in human U-2 OS cells (Figure 3.3D, E). We again observed that NINL KO cells had a significant reduction in the antiviral effects of IFNα pretreatment (Figure 3.2C). To test whether this effect was specific to VSV replication, we tested two positive-sense single-stranded RNA (+ssRNA) viruses: Sindbis virus (SinV)– an enveloped

virus, and coxsackievirus B3 (CVB3)– a non-enveloped virus in both A549 and U-2 OS cells. In

both cases, we observed a potent antiviral effect of IFNα pretreatment in WT and NIN KO cells,

while this effect was reduced in NINL KO cells (Figure 3.2D, Figure 3.4A-D). The attenuation

of the IFN-induced antiviral effect against viruses from three distinct families suggests that

NINL may broadly play a role in the IFN-mediated innate immune response to viruses.
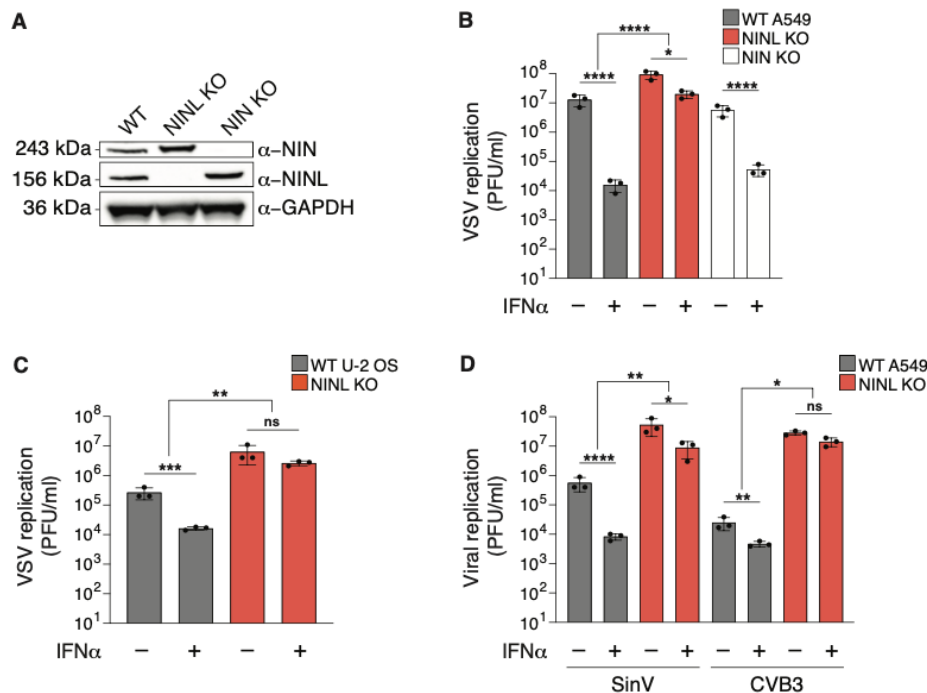
Figure 3.2. The antiviral potency of IFNα is reduced in NINL KO cells. (**A**) Immunoblots of WT A549 cells, and CRISPR/Cas9-generated NINL and NIN KO A549 cells probed with the indicated antibodies. GAPDH served as a loading control. Protein molecular weight markers are shown in kilodaltons (kDa) to the left of each immunoblot. Representative images from three biological replicates are shown. (**B**) WT, NINL KO, and NIN KO A549 cells were treated with 100U IFNα for 24 hours and then infected with VSV (5000 PFU/mL, MOI ≈ 0.01). Virus-containing supernatants were collected nine hours post-infection and viral titers (y-axis, plaque forming units per mL) were determined by plaque assay. (**C**) WT or NINL KO U-2 OS cells were treated with 100U IFNα for 24 hours and then infected with VSV (5000 PFU/mL, MOI ≈ 0.01). Virus-containing supernatant was collected nine hours post-infection and viral titers (y-axis, plaque forming units per mL) were determined by plaque assay. (**D**) WT or NINL KO A549 cells were treated with 100U IFNα for 24 hours and then infected with Sindbis virus (500,000 PFU/mL, MOI ≈ 1.0) (left) or treated with 1000U IFNα for 24 hours and then infected with coxsackievirus B3 (5000 PFU/mL, MOI ≈ 0.01) (right). Virus-containing supernatants were collected 24 hours post-infection and viral titers (y-axis, plaque forming units per mL) were determined by plaque assay. (**B-D**) Data are presented as mean ± standard deviation of three experiments, with individual points shown. Data were analyzed by two-way ANOVA with Tukey's method adjustment for multiple comparisons for IFNα treatment within each cell line, two-way ANOVA interaction comparison for IFNα interaction between cell lines. *$p<0.05$, **$p<0.01$, ***$p<0.001$, ****$p<0.0001$, ns = not significant.
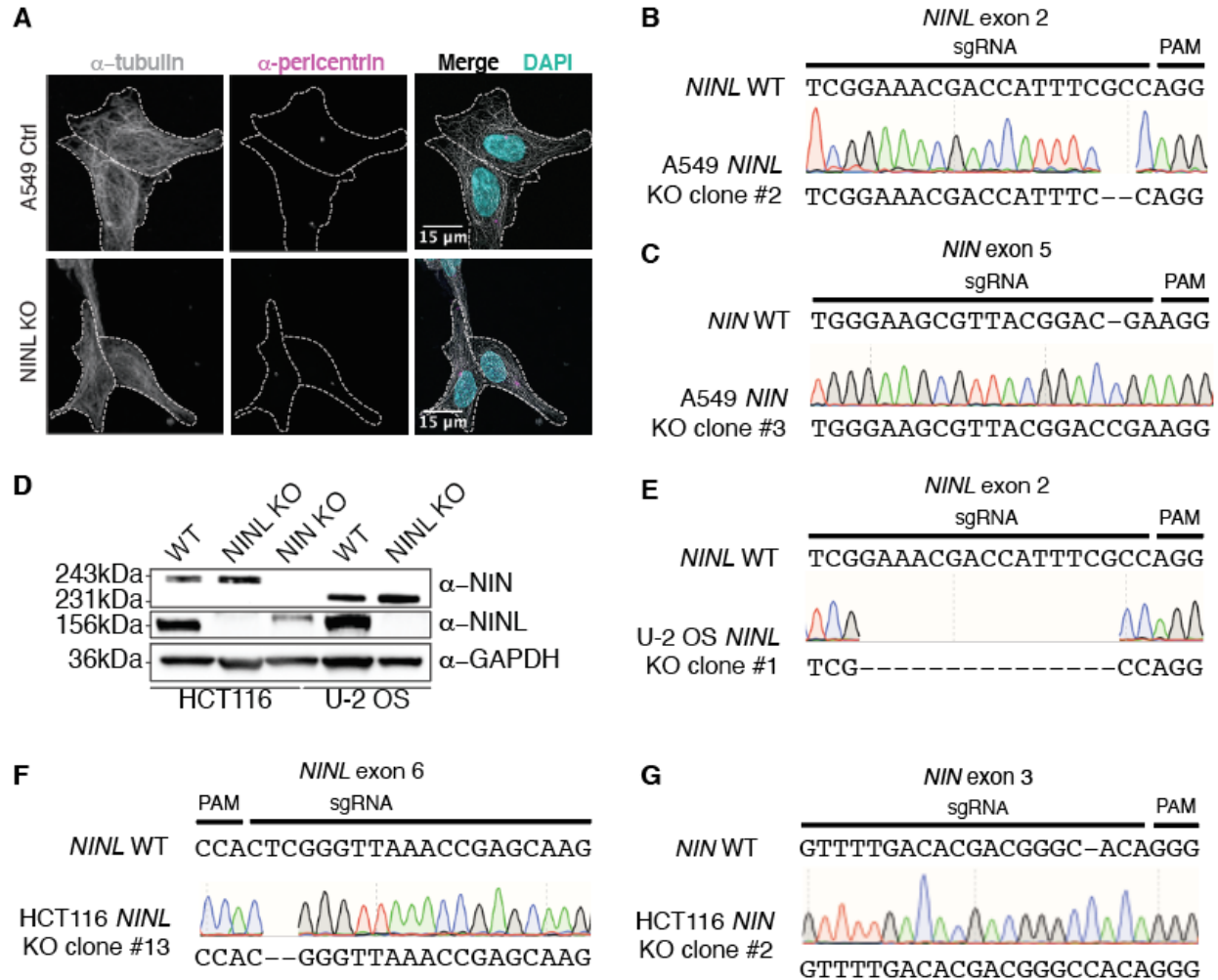
Figure 3.3. Validation of CRISPR/Cas9-editing to generate NINL and NIN KO cells. (**A**) Confocal micrographs displayed as maximum intensity projections of WT and NINL KO A549 cells. Immunostaining with anti-pericentrin and anti-tubulin antibodies was used to visualize centrosomes and microtubules, respectively. Nuclei were visualized with DAPI. 15 μm scale bars are shown in the merged micrographs. Dashed white lines denote cellular boundaries. Representative micrographs from two biological replicates are shown. (**B**) Sequence verification of exon 2-targeted NINL KO A549 cells. An excerpt of the WT *NINL* sequence is shown with the CRISPR-targeting sgRNA and PAM sequences indicated (top), the sequencing chromatogram (middle), and the sequence of the NINL KO (bottom). (**C**) Sequence verification of exon 5-targeted NIN KO A549 cells. (**D**) Immunoblots of control (CTRL) HCT116 and U-2 OS cells, and CRISPR/Cas9-generated NINL and NIN KO HCT116 and U-2 OS cells probed with the indicated antibodies. GAPDH served as a loading control. Protein molecular weight markers are shown in kilodaltons (kDa) to the left of each immunoblot. Representative images from three biological replicates are shown. (**E**) Sequence verification of exon 2-targeted NINL KO U-2 OS cells. (**F**) Sequence verification of exon 6-targeted NINL KO HCT116 cells. (**G**) Sequence verification of exon 3-targeted NIN KO HCT116 cells.

81
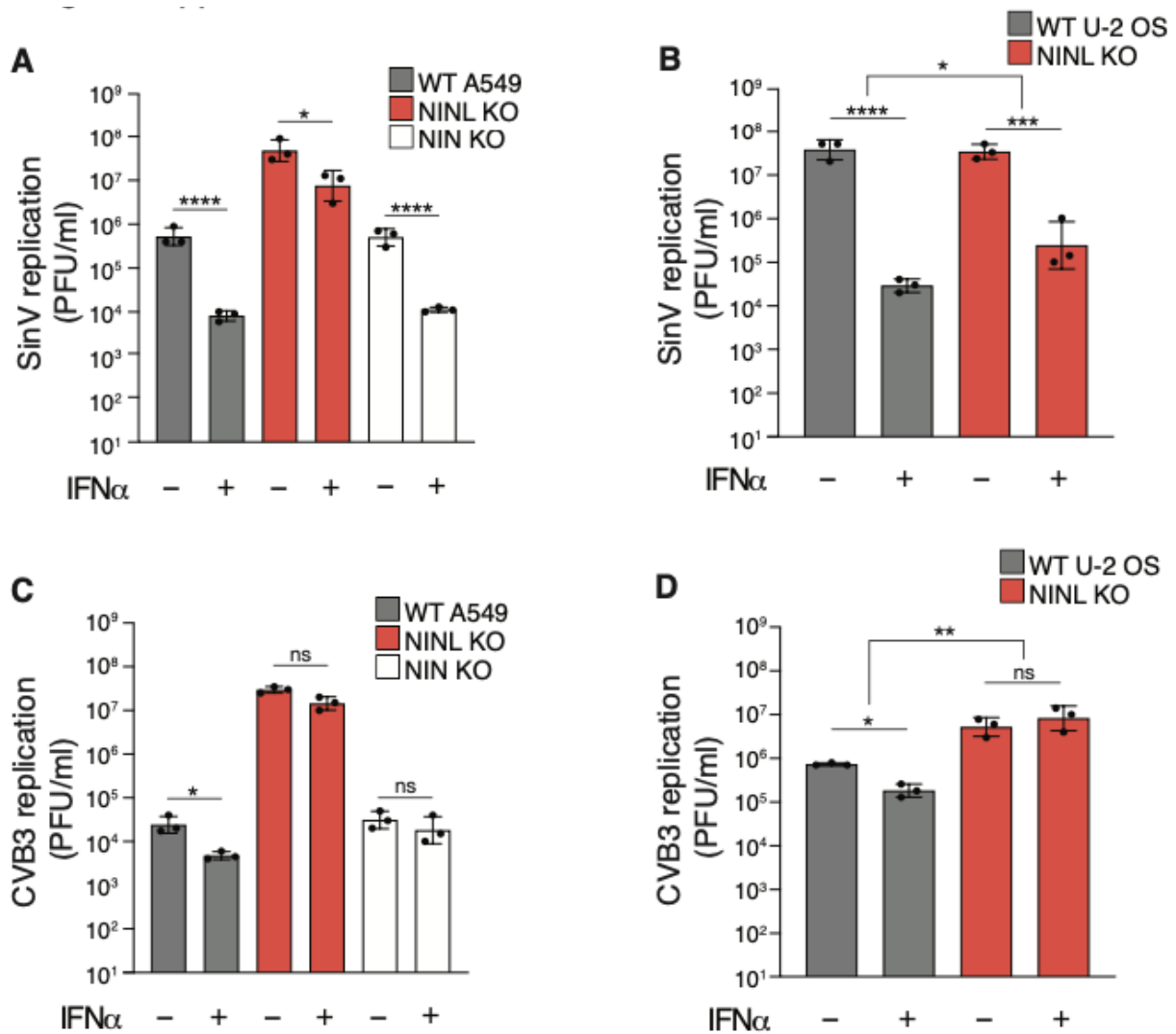
Figure 3.4. Reduction of IFNα-mediated antiviral response is observed across multiple cell lines. (**A**) A549 WT, NINL KO, or NIN KO cells were treated with 100U IFNα for 24 hours, then infected with Sindbis virus (500,000 PFU/mL, MOI ≈ 1.0). Cells were collected 24 hours post-infection and viral titers (y-axis, plaque forming units per mL) were determined by plaque assay. WT and NINL KO data are reproduced from Figure 3.2D for comparison. (**B**) U-2 OS WT or NINL KO cells were treated, infected, harvested, and quantified as described in (**A**). (**C**) A549 WT, NINL KO, or NIN KO cells were treated with 1000U IFNα for 24 hours, then infected with coxsackievirus B3 (5,000 PFU/mL, MOI ≈ 0.01). Cells were collected 24 hours post-infection and viral titers (y-axis, plaque forming units per mL) were determined by plaque assay. WT and NINL KO data are reproduced from Figure 3.2D for comparison. (**D**) U-2 OS WT or NINL KO cells treated, infected, harvested, and quantified as described in (C). (A-D) Data are presented as mean ± standard deviation of three experiments, with individual points shown. Data were analyzed by two-way ANOVA with Tukey's method adjustment for multiple comparisons for IFNα treatment within each cell line, two-way ANOVA interaction comparison for IFNα interaction between cell lines. *p<0.05, **p<0.01, ***p<0.001, ****p<0.0001, ns = not significant.

*Loss of NINL results in an attenuated antiviral immune response*

Based on the reduced antiviral potency of IFNα in cells lacking NINL, we next investigated whether there was an attenuation of IFN-mediated signaling in NINL KO cells. Type I IFNs, such as IFNα, activate the Janus kinase/signal transducer and activator of transcription (JAK/STAT) pathway to trigger the expression of IFN-stimulated genes (ISGs), which include potent antiviral effectors (Schoggins, 2019). Therefore, we asked whether there was a defect in the JAK/STAT signaling cascade by western blot analysis of the phosphorylation of the transcription factors STAT1 (pSTAT1(Y701)) and STAT2 (pSTAT2(Y690)) as well as the induction of ISG expression following IFNα pretreatment. Despite robust phosphorylation of STAT1 and STAT2 in response to IFNα pretreatment in WT, NINL KO, and NIN KO cells, protein expression of the canonical ISGs–MX1, IFIT3, OAS1, and ISG15 was greatly reduced in NINL KO cells relative to WT or NIN KO cells (Figure 3.5A). To again confirm that this was not specific to cell type, we showed that this lack of ISG protein expression was independent of cell background or the choice of CRISPR guide (Figure 3.3A-G, Figure 3.6A). Next, we performed RNAseq analyses on WT, NINL KO, and NIN KO A549 cells in the presence or absence of IFNα pretreatment. In WT cells, we identified 88 ISGs that were significantly (adjusted p-value ≤ 0.05, log2fold change ≥ 1) upregulated in response to IFN treatment (Figure 3.7A). We then compared the transcriptional profiles of these ISGs between IFNα-treated WT, NINL KO, and NIN KO cells. Consistent with our western blot analysis, the induction pattern of ISG transcripts in WT and NIN KO cells was similar, whereas many ISG transcripts from IFNα treated NINL KO cells were downregulated compared to IFNα treated WT cells (Figure 3.5B, Figure 3.8A, Figure 3.9A-C). Other transcripts unrelated to the IFN response also showed altered expression in NINL KO cells relative to WT cells (Figure 3.9A-C and Supplementary File 3.4).

However, the overall lower expression of ISGs in NINL KO relative to WT cells (Figure 3.9A-B) indicates that cells lacking NINL have a distinct defect in their ability to mount an effective antiviral immune response.

To further demonstrate that the lack of ISG expression in cells lacking NINL has a profound effect on the interferon-mediated antiviral response, we took advantage of a virus in which interferon sensitivity can be modulated genetically. Vaccinia virus (VacV) is a large double-stranded DNA virus that is relatively insensitive to the effects of IFNα due to the large number of proteins the virus encodes that antagonize the immune response (Yu et al., 2021). However, a point mutation in the J3 methyltransferase protein (VacV J3) confers interferon sensitivity by sensitizing the virus to the antiviral effects of the IFIT family of ISGs (Daffis et al., 2010; Daugherty et al., 2016; Johnson et al., 2018; Latner et al., 2002). As IFIT1, IFIT2, and IFIT3 were among the ISGs we saw decreased in NINL KO cells relative to WT and NIN KO cells, we hypothesized that NINL KO cells may lack the ability to inhibit the J3 mutant vaccinia virus after IFNα pretreatment. As expected, in WT and NIN KO A549 cells, wildtype VacV (VacV WT) was insensitive to IFNα, whereas VacV J3 replication was significantly reduced upon IFNα pretreatment (Figure 3.5C, Figure 3.10A). In contrast, mutant and wildtype viruses replicated equivalently in the NINL KO cells regardless of IFNα pretreatment (Figure 3.5D). We found the same differential response to the J3 VacV mutant between WT and NINL KO cells in U-2 OS cells, showing that this phenotype is not cell type specific (Figure 3.10B, C). All together, these data suggest NINL plays a critical role during the IFN-mediated antiviral immune response, further substantiating our hypothesis that NINL is at the center of an antagonistic host-pathogen interaction.
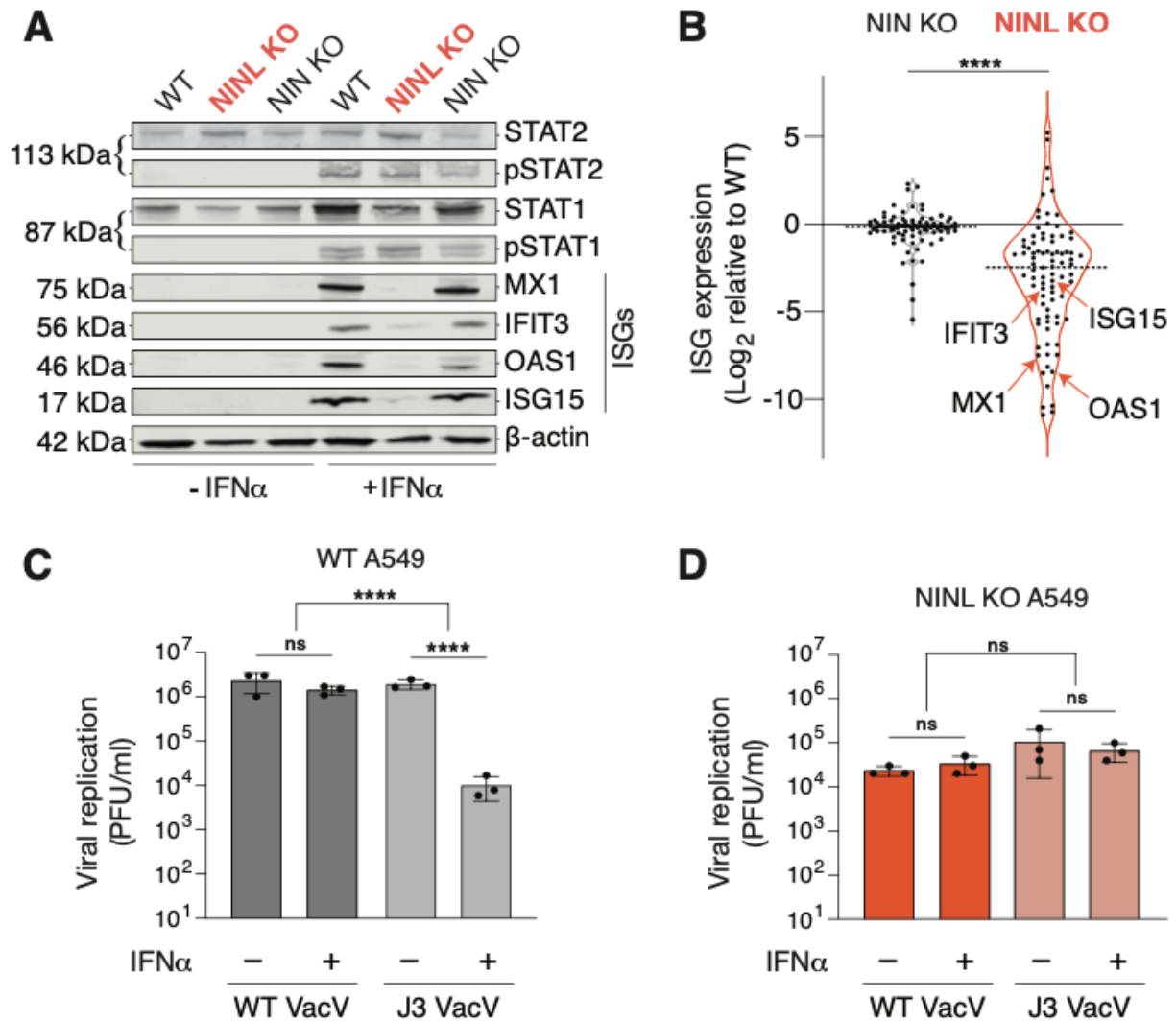
Figure 3.5. NINL KO cells fail to mount an effective IFN response. (**A**) Immunoblot of extracts from WT, NINL KO, and NIN KO A549 cells untreated (-) or treated (+) with IFNα. Immunoblots were probed with anti-STAT2, anti-Phospho-STAT2 (Tyr690), anti-STAT1, anti-Phospho-STAT1 (Tyr701), anti-Mx1, anti-IFIT3, anti-OAS1, anti-ISG15, and anti-β-actin antibodies. Protein molecular weight markers are shown in kilodaltons (kDa) to the left of each immunoblot. Representative images from three biological replicates are shown. (**B**) Differential ISG expression in WT, NINL KO, and NIN KO cells induced with IFNα. ISGs were identified as the 88 genes whose expression was upregulated in WT cells after IFNα pretreatment (Figure 3.7). Data are displayed as a violin plot of ISG expression in NIN KO or NINL KO cells relative to WT cells. **** = $p<0.0001$ based on paired t-test. Dotted line indicates mean. Individual data points for ISGs shown in panel (A) are indicated. (**C**) A549 WT cells were treated with 1000U IFNα for 24 hours, then infected with wild-type vaccinia virus (WT VacV) or J3 mutant vaccinia virus (J3 VacV) (50,000 PFU/mL, MOI ≈ 0.1). Cell-associated virus was collected 24 hours post-infection and viral titers (y-axis, plaque forming units per mL) were determined by plaque assay. (**D**) A549 NINL KO cells were treated, infected, harvested, and quantified as described in (C). (C-D) Data are presented as mean ± standard deviation of three experiments, with individual points shown. Data were analyzed by two-way ANOVA with Tukey's method adjustment for multiple comparisons for IFNα treatment within each cell line, two-way ANOVA interaction comparison for IFNα interaction between cell lines. ****$p<0.0001$, ns = not significant.
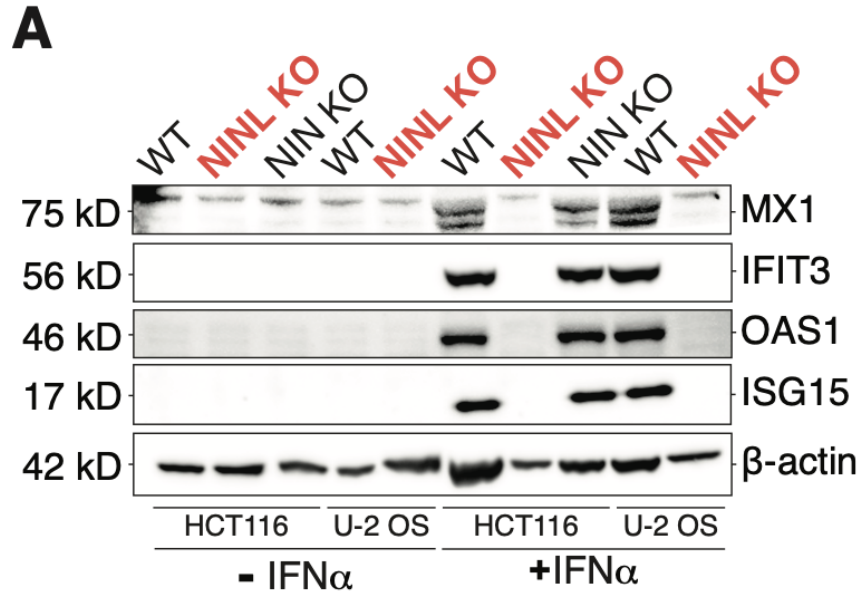
Figure 3.6. Reduced ISG production occurs following NINL KO in multiple cell lines generated using different CRISPR gRNAs (A) Immunoblot of extracts from WT HCT116, HCT116 NINL KO, HCT 116 NIN KO, WT U2-OS, U2-OS NINL KO, and U2-OS NIN KO cells untreated or treated with IFNα. Immunoblots were probed with anti-STAT2, anti-Phospho-STAT2 (Tyr690), anti-STAT1, anti-Phospho-STAT1 (Tyr701), anti-Mx1, anti-IFIT3, anti-OAS1, anti-ISG15, and anti-β-actin antibodies. Protein molecular weight markers are shown in kilodaltons (kDa) to the left of each immunoblot. Representative images from three biological replicates are shown.
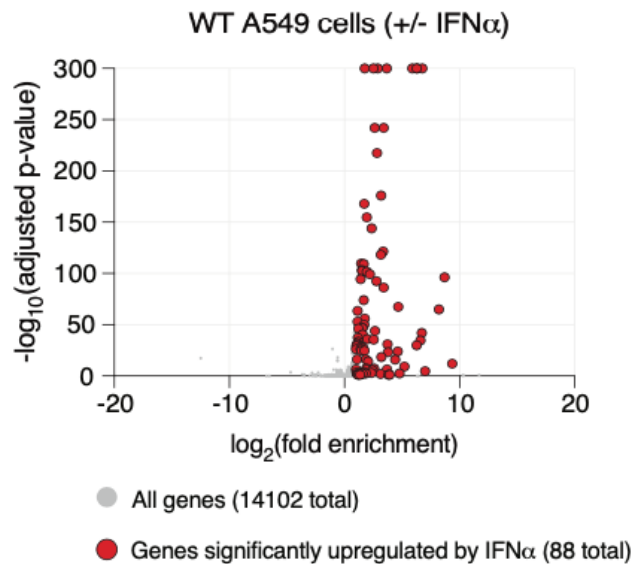
Figure 3.7. Identification of 88 ISGs in WT A549 cells. Differential gene expression from RNAseq analyses of WT A549 cells pretreated with IFNα compared to untreated. Each condition (untreated or IFNα) was performed in triplicate, with independent RNA extractions, sequencing library preparation, and sequencing. RNA levels for a total of 14102 genes (grey dots) could be compared (see Materials and Methods). Only 88 genes (red dots) showed a statistically significant upregulation (adjusted p-value ≤0.05, $\log_2$-fold change ≥1), which we refer to in subsequent analyses as ISGs.
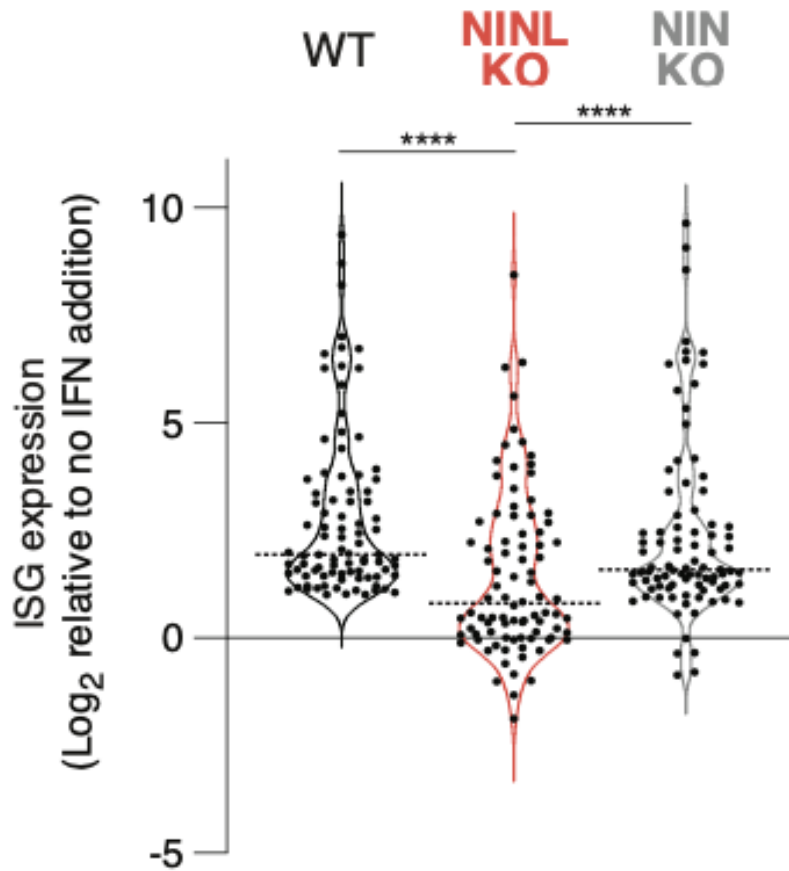
Figure 3.8. Interferon induction has a reduced effect on ISG expression in NINL KO cells. Differential gene expression of 88 ISGs (identified in Figure 3.7) from RNAseq analyses of the indicated cell lines pretreated with IFNα compared to untreated. Each condition (untreated or IFNα) was performed in triplicate, with independent RNA extractions, sequencing library preparation, and sequencing. Only the 88 genes significantly upregulated in WT cells, which we refer to as ISGs (adjusted p-value ≤0.05, $\log_2$-fold change ≥1), are shown for each cell line. Data are displayed as a violin plot of ISG upregulation, with the dotted line indicating the mean. ****p<0.0001 based on one-way ANOVA test.
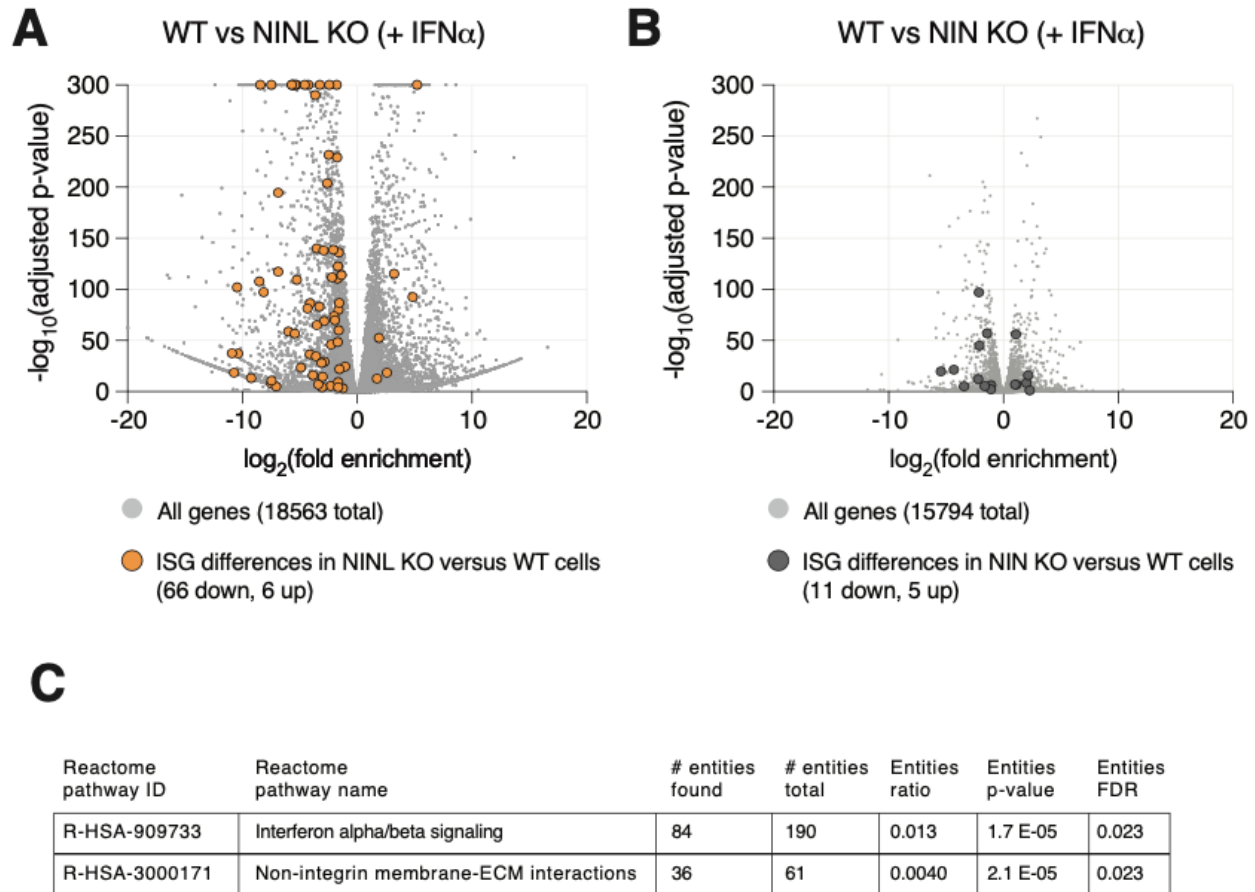
Figure 3.9. Differential gene expression in NINL KO and NIN KO cells compared to WT cells. (**A**) Differential gene expression from RNAseq analyses of NINL KO cells treated with IFNα compared to WT A549 cells treated with IFNα. Each cell line (NINL KO or WT) was treated with IFNα in triplicate, with independent RNA extractions, sequencing library preparation, and sequencing. RNA levels for a total of 18563 genes (grey dots) could be compared (see Methods). Orange dots highlight the 72 ISGs that are significantly differentially expressed between cell lines, with the majority (66 of 72) of ISGs significantly lower in NINL KO cells (adjusted p-value ≤0.05, $\log_2$-fold change ≤-1). (**B**) Differential gene expression from RNAseq analyses of NIN KO cells treated with IFNα compared to WT A549 cells treated with IFNα. Dark grey dots highlight the 11 ISGs that are significantly differentially expressed between cell lines. (**C**) Reactome pathway analysis (Jassal et al., 2020) of the 3549 genes with significantly lower expression (adjusted p-value ≤0.05, $\log_2$-fold change ≤-1) in NINL KO cells treated with IFNα relative to WT cells treated with IFNα. Only the two pathways shown were identified as significantly different between the cell lines. The number of genes found to be lower in NINL KO cells (# entities found) compared to the number of genes in the indicated pathway (# entities total) is shown. The p-value, as well as false discovery rate (FDR) adjusted p-values are shown.
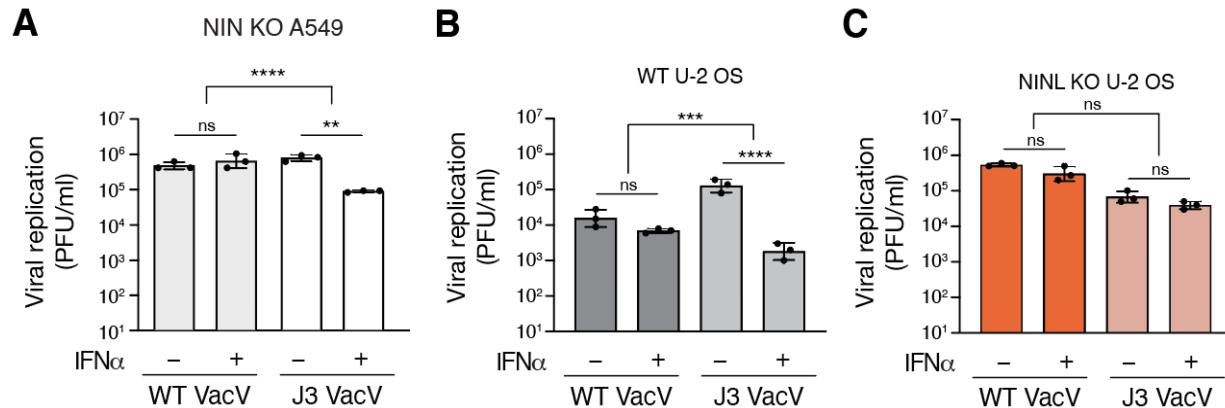
Figure 3.10. NINL KO results in loss of interferon sensitivity of the VacV J3 mutant. (**A**) A549 NIN KO cells were treated with 1000U IFNα for 24 hours, then infected with wildtype vaccinia virus (VacV WT) or J3 mutant vaccinia virus (J3 VacV) (50,000 PFU/mL, MOI ≈ 0.1). Cell-associated virus was collected 24 hours post-infection and viral titers (y-axis, plaque forming units per mL) were determined by plaque assay. (**B**) U-2 OS WT cells were treated with 1000U IFNα for 24 hours, then infected with wild-type vaccinia virus or J3 mutant vaccinia virus (50,000 PFU/mL, MOI ≈ 0.1). Cells were collected 24 hours post-infection and viral titers (y-axis, plaque forming units per mL) were determined by plaque assay. (**C**) U-2 OS NINL KO cells were treated, infected, harvested, and collected as indicated in (B). (A-C) Data are presented as mean ± standard deviation of three experiments, with individual points shown. Data were analyzed by two-way ANOVA with Tukey's method adjustment for multiple comparisons for IFNα treatment within each viral infection, two-way ANOVA interaction comparison for IFNα interaction between viral infections. are presented as mean ± standard deviation of three experiments, with individual points shown. **p<0.01, *** p<0.001, ns = not significant.

Viral proteases cleave NINL in a host-specific manner

The IFN response is the first line of host antiviral defense during viral infection. Thus, viruses have developed many strategies to evade or subvert the host IFN response (Beachboard and Horner, 2016; Hoffmann et al., 2015). Our data indicating that NINL is important for the IFN response, combined with the observation that NINL is evolving under positive selection, led us to hypothesize that viruses may antagonize NINL function. As one such viral antagonism strategy is to deploy virus-encoded proteases to cleave components of the host antiviral defense system (Lei and Hilgenfeld, 2017; Tsu et al., 2021), we investigated whether viral proteases cleave NINL. Using a predictive model of enteroviral 3C protease (3C^{pro}) target specificity (Tsu et al., 2021), we identified three high-confidence sites of potential cleavage within NINL at residues 231, 827, and 1032 (Figure 3.11A) that all exhibit amino acid changes within primates

that are expected to alter 3C^{pro} cleavage probability (Figure 3.11B). Indeed, upon transfection of

cells with NINL and CVB3 3C^{pro}, we observed an overall reduction of full-length NINL and the

appearance of two cleavage products at sizes that correspond to predicted cleavage at sites 827

and 1032 (Figure 3.11C, D). We also observed a weaker product at a size that corresponds to the

predicted size of NINL after cleavage at site 231. To confirm cleavage site specificity, we

generated NINL point mutants that take advantage of the diversity of these sites found in

primates (Figure 3.11B). Specifically, we replaced the glutamine immediately preceding the site

of cleavage (the P1 position) with an arginine found in non-human primates that we predicted

would prevent cleavage by 3C^{pros} (Tsu et al., 2021) for each of the predicted sites. Co-

transfection of CVB3 3C^{pro} with NINL containing these mutations individually (Q1032R) or in

combination (double mutant Q827R/Q1032R and triple mutant Q231R/Q827R/Q1032R)

confirmed the sites of cleavage, with the NINL triple mutant eliminating all cleavage products by

CVB3 3C^{pro} (Figure 3.11D). We also noted that two of these sites (Q827 and Q1032), along with

many of the codons predicted to be evolving under positive selection (Figure 3.1C), reside in a

single exon (exon 17) within the carboxy-terminal region of NINL (Figure 3.11A). Intriguingly,

this exon is lacking in an alternatively spliced isoform of NINL (isoform 2) (Dona et al., 2015;

Kersten et al., 2012; van Wijk et al., 2009). We therefore tested whether isoform 2 is cleaved by

CVB3 3C^{pro}. Consistent with the loss of two primary sites of cleavage, we observed little

decrease in the full-length product when isoform 2 was co-transfected with CVB3 3C^{pro},

although we did observe weak protease-mediated cleavage at site 231 in isoform 2 (Figure

3.11D).

We next sought to understand the degree to which cleavage of NINL is conserved across viral proteases. We, therefore, tested a panel of 3C^{pros} from diverse viruses in the *Picornaviridae* family (Tsu et al., 2021). Interestingly, while we found that all proteases tested were able to cleave NINL to some degree, the strength and position of cleavage was variable, even among proteases from closely related viruses such as members of the enterovirus genus (Figure 3.12A). We also tested a panel of 3C-like proteases (3CL^{pros}) from members of the *Coronaviridae* family, including proteases from the betacoronaviruses SARS-CoV-2 and SARS-CoV, and an alphacoronavirus, NL63-CoV. We again observed numerous cleavage products, some of which map to residues 827 and 1032 (Figure 3.12B), consistent with 3C^{pros} and 3CL^{pros} having similar active sites and cleavage preferences (Ng et al., 2021). Together, these data indicate that NINL is cleaved at species-specific sites by various proteases from human viruses. Such host- and virus-specificity of cleavage is a hallmark of host-virus arms races, further supporting the model that NINL's role in the interferon response positions it in evolutionary conflict with viruses.

We next aimed to confirm that infection-mediated cleavage efficiency and specificity recapitulated results we observed from transiently transfected viral proteases. We therefore infected cells expressing WT NINL and the NINL triple mutant with CVB3, a virus that encodes a 3C^{pro} that strongly cleaves NINL at multiple sites, and EMCV, a virus that encodes a 3C^{pro} that only weakly cleaves NINL at a single site in the N-terminus (Figure 3.12A). Consistent with the results we obtained with transfected 3C^{pros}, we observed cleavage of NINL at species-specific sites 231, 827, and 1032 when we infected with CVB3, and little to no cleavage upon EMCV infection (Figure 3.11E). These data further support that NINL is a target of viral antagonism upon infection in a manner that is both host- and virus-specific.

91

Figure 3.11. NINL is cleaved at species-specific sites by virally encoded proteases. (**A**) Schematic of human NINL, with positions of predicted 3C^{pro} cleavage sites annotated. Shown are the four amino acids on each side of the predicted cleavage site in human NINL, along with the residue positions and cleavage score predicted using a motif search with the consensus enterovirus cleavage site (see Methods). (**B**) NINL sequences from 12 primate species and mice for each predicted 3C^{pro} cleavage site. Amino acid changes relative to human NINL are highlighted in colors to denote differences in polarity and charge. (**C**) Schematic of 3xFLAG-NINL-Myc isoform 1 and isoform 2 constructs, with predicted molecular weights for both amino-terminal (FLAG) and carboxy-terminal (Myc) products upon cleavage by 3C^{pro}. (**D**) Immunoblots of extracts from HEK293T cells co-transfected with the indicated NINL constructs and either CVB3 3C^{pro} or the catalytically inactive (C147A) CVB3 3C^{pro} (mutant). Immunoblots were probed with anti-FLAG (NINL amino-terminus), anti-Myc (NINL carboxy-terminus), anti-HA (3C^{pro}), and anti-GAPDH (loading control). Arrows to the left of each immunoblot indicate full-length products as well as products corresponding to cleavage at the indicated amino acid residue. Protein molecular weight markers are shown in kilodaltons (kDa) to the right of each immunoblot. Representative images from three biological replicates are shown. (**E**) Immunoblots of extracts from HEK293T cells transfected with the indicated amino-terminal FLAG and carboxyl-terminal Myc tagged NINL constructs and infected with either CVB3 or EMCV (500,000 PFU/mL, MOI ≈ 1.0 for 8 h). Immunoblots were probed with anti-FLAG (NINL amino-terminus), anti-Myc (NINL carboxy-terminus), and anti-GAPDH (loading control). Arrows to the left of each immunoblot indicate full length products as well as products corresponding to CVB3 3C^{pro} cleavage at the indicated amino acid residue. Protein molecular weight markers are shown in kilodaltons (kDa) to the right of each immunoblot. Representative images from three biological replicates are shown.

A

Q231   Q827   Q1032

VGLQGLEK   AEMQALPK   ADPQGSWQ

Position: 228 - 235   824 - 831   1029 - 1036
p-value: 0.000972   0.00202   0.000133

B

	VGLQGLEK	AEM-QALPK	ADPQGSWQ
Human	VGLQGLEK	AEM-QALPK	ADPQGSWQ
Chimpanzee	VGLQGLEK	AEMLQALPK	ADPQGSWQ
Gorilla	VGLQGLEK	AEMLQALPK	ADPQGSWQ
Orangutan	VGLQGLEK	AEMLRALPK	ADPRGSWQ
Gibbon	VGLQGLKK	AEMLNALPK	ADPRGSWQ
Rhesus macaque	VGLRGLEK	AEMLGALPK	AEPGASRQ
Olive baboon	VGLREGLEK	AEMLGALPK	ADPRASRQ
Drill	VGLRGLEK	AEMLGALPK	ADPRASRQ
Gelada	VGLRGELEK	AEMLGALPK	ADPRGSGQ
Snub-nosed monkey	IGLRGLEK	AEMLGALPK	ADPRASRQ
Squirrel monkey	VGLQGLKK	AEMLLALPK	SDPRGAGQ
Marmoset	VGRGLKK	AEMLRALPK	SDLRGAGQ
Mouse	IGLHSLEK	ADVLRALLK	PNP----Q

C

	Predicted α-FLAG (N-term) mol. weight		Predicted α-Myc (C-term) mol. weight
Isoform 1	159 kDa	3x-FLAG ▭ Myc	159 kDa
	25 kDa	3x-FLAG ✂231 Myc	134 kDa
	93 kDa	3x-FLAG ✂827 Myc	66 kDa
	115kDa	3x-FLAG ✂1032 Myc	44 kDa

Exon 17

| Isoform 2 | 121 kDa | 3x-FLAG ▭ Myc | 121 kDa |
| | 25 kDa | 3x-FLAG ✂231 Myc | 96 kDa |

D

α-FLAG (N-terminal)

α-Myc (C-terminal)

α-GAPDH

α-HA

E

α-FLAG (N-terminal)

α-Myc (C-terminal)

α-GAPDH

93

Figure 3.12. 3C and 3CL proteases from diverse viruses cleave NINL at redundant and unique sites. (**A**) Immunoblots of extracts from HEK293T cells co-transfected with the indicated NINL constructs and 3C^pro from the indicated picornavirus. CVB3: coxsackievievirus B3, CVB3 mutant: catalytically inactive (C147A) CVB3 3C^pro, EV71: enterovirus A71, PV1: poliovirus 1, EV68: enterovirus D68, HRVA: human rhinovirus A, EMCV: encephalomyocarditis virus, Parecho: parechovirus A, HepA: hepatitis A virus, Sali: salivirus A. Immunoblots were probed with anti-Myc (NINL carboxy-terminus), anti-HA (3C^pro), and anti-GAPDH (loading control). Arrows to the left of each immunoblot indicate full-length products as well as products corresponding to CVB3 3C^pro cleavage at the indicated amino acid residue. Protein molecular weight markers are shown in kilodaltons (kDa) to the right of each immunoblot. Representative images from three biological replicates are shown. (**B**) Immunoblots of extracts from HEK293T cells co-transfected with the indicated NINL constructs and the indicated coronaviral 3CL^pro. SARS2: SARS-CoV-2, SARS2 mutant: catalytically inactive (C145A) SARS-CoV-2 3CL^pro SARS1: SARS-CoV, NL63: HCoV-NL63. 3CL^pros were expressed as self-cleaving constructs that remove a carboxy-terminal mCherry-HA tag. Immunoblots were probed with anti-Myc (NINL carboxy-terminal), anti-HA (cleaved mCherry-HA from catalytically active protease constructs, or eGFP-3CL^pro-mCherry-HA from catalytically inactive protease constructs), and anti-GAPDH (loading control). Arrows to the left of each immunoblot indicate full-length products as well as products corresponding to SARS-CoV-2 3CL^pro cleavage at the indicated amino acid residue. Protein molecular weight markers are shown in kilodaltons (kDa) to the right of each immunoblot. Representative images from three biological replicates are shown.
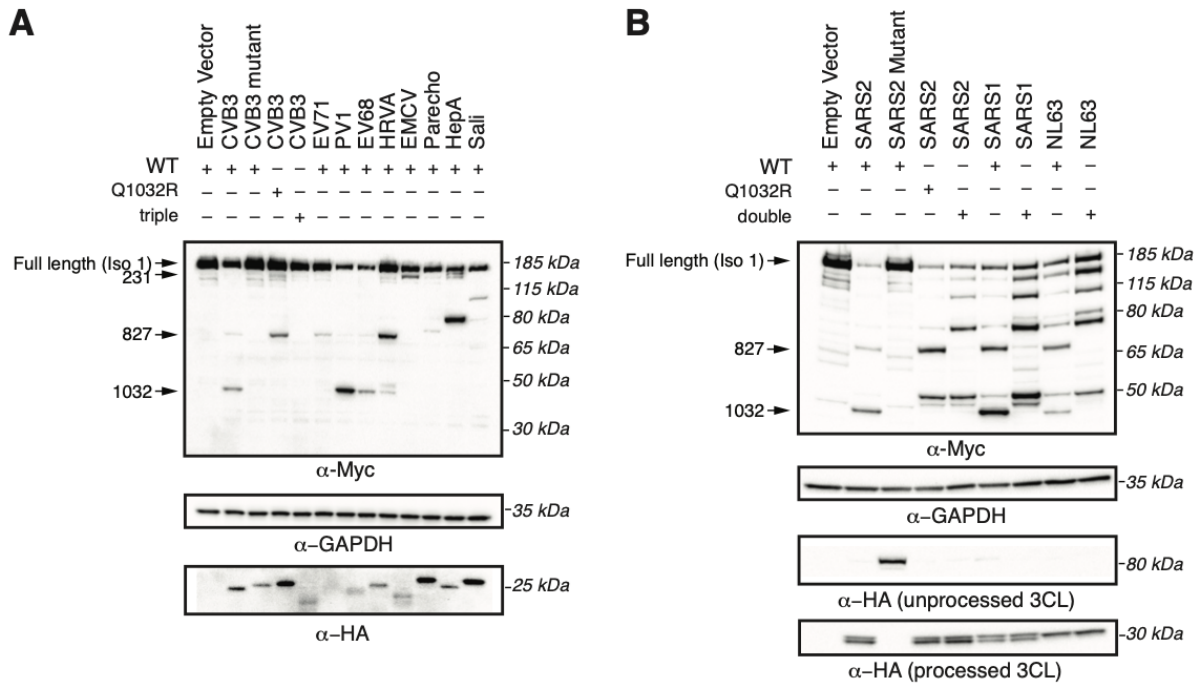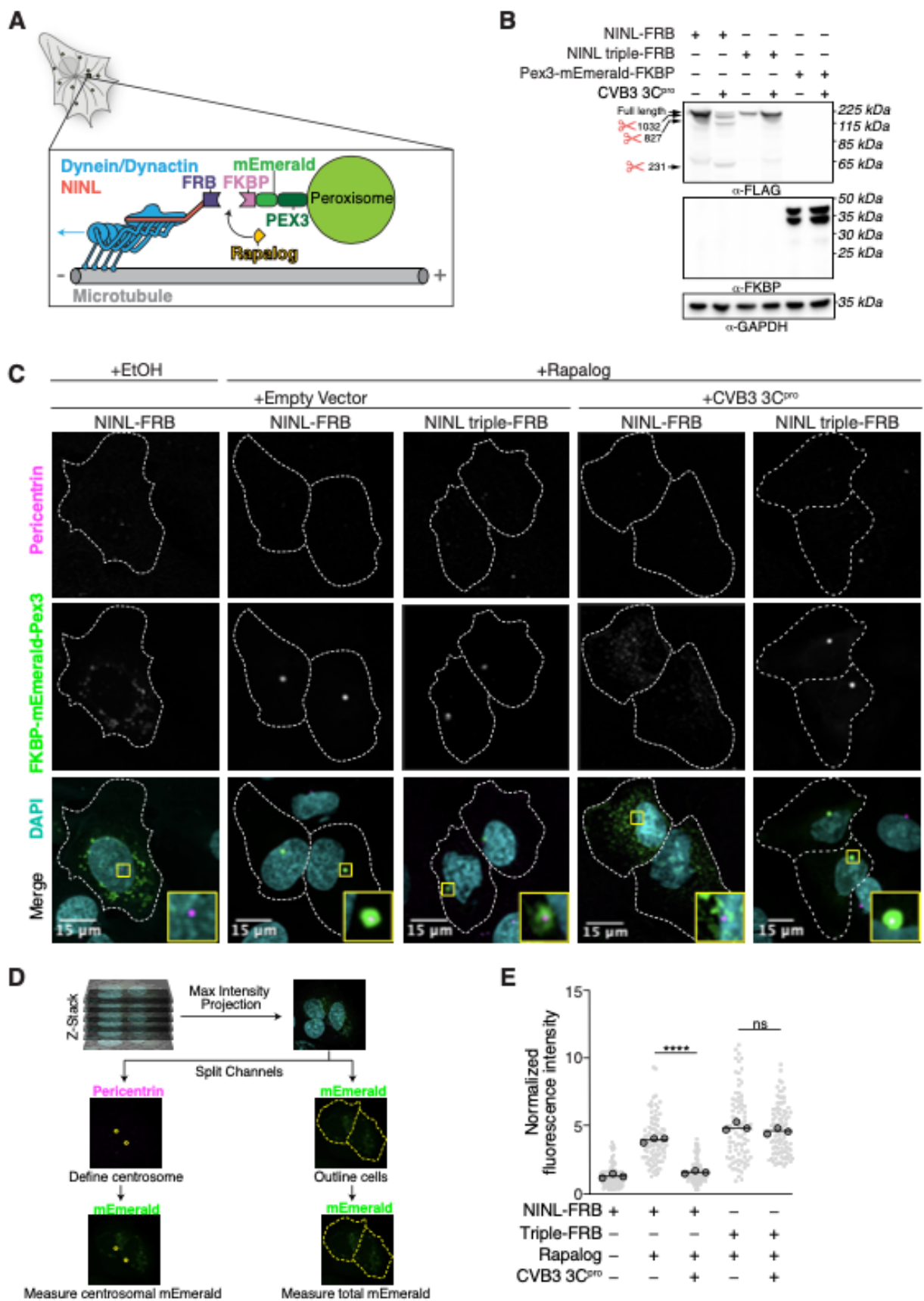
94

Viral proteases disrupt NINL trafficking function

As NINL is a dynein activating adaptor, we next sought to investigate whether proteolytic

cleavage of NINL could interfere with cargo trafficking. NINL is well known as a centrosome-

associated protein and may also be involved in trafficking endo/lysosomal

membranes(Bachmann-Gagescu et al., 2015; Xiao et al., 2021). In addition, a number of NINL-

interacting proteins have been described (Bachmann-Gagescu et al., 2015; Casenghi et al., 2003;

Dona et al., 2015; Kersten et al., 2012; Redwine et al., 2017; van Wijk et al., 2009). However, in

the context of the interferon response, we have not yet identified a NINL cargo. Thus, we chose

to reconstitute NINL's role in dynein-mediated microtubule transport using a heterologous

approach (Kapitein et al., 2010; Passmore et al., 2021). This well-established method uses an

inducible heterodimerization system (Figure 3.13A) to induce the movement of normally

immotile peroxisomes by recruiting dynein via an activating adaptor to the peroxisome (Htet et

al., 2020; Huynh and Vale, 2017; Wang et al., 2019). Briefly, a rapamycin-binding FKBP

domain was targeted to peroxisome membranes via the peroxisome targeting sequence (PTS1) of

human PEX3. Another rapamycin-binding FRB domain was fused to the NINL and the NINL

triple mutant constructs. We truncated the NINL constructs at residue 1062 because some

activating adaptors are autoinhibited via interactions between their amino- and carboxy-termini

(Liu et al., 2013; Terawaki et al., 2015; Urnavicius et al., 2015). Co-transfection of cells with

CVB3 3C[pro], PEX3-mEmerald-FKBP, and WT NINL or the uncleavable NINL triple mutant

confirmed that WT NINL is cleaved by CVB3 3C[pro], while the NINL triple mutant is not (Figure

3.13B and Figure 3.14A). When we introduced these constructs into human U-2 OS peroxisomes

were distributed throughout the cytoplasm (Figure 3.13C and Figure 3.14B, C), but redistributed

to the centrosome upon the addition of the rapamycin analog, rapalog (which induces

95

dimerization of FRB and FKBP (Ho et al., 1996) (Figure 3.13C-E). In contrast, when NINL was

co-expressed with CVB3 3C^{pro}, peroxisomes no longer localized to the centrosome (Figure

3.13C-E). However, the uncleavable NINL triple mutant was still able to redistribute

peroxisomes in the presence of CVB3 3C^{pro} just as effectively as cells not expressing CVB3

3C^{pro} (Figure 3.13C-E). Finally, to determine if viral infection could also disrupt NINL-mediated

trafficking, we infected cells with CVB3 following transfection of PEX3-mEmerald-FKBP, and

WT NINL or the uncleavable NINL triple mutant. Similar to transfection with viral protease, live

CVB3 infection led to a significant reduction in peroxisomes that localized to the centrosome in

cells expressing NINL, but not in cells expressing the uncleavable NINL triple mutant (Figure

3.15A, B and Figure 3.16A, B). Together, these data demonstrate that site-specific cleavage of

NINL by CVB3 3C^{pro} could disrupt NINL's role in cargo transport.

Figure 3.13. CVB3 3Cpro cleavage of NINL prevents rapalog-induced dynein-dependent transport of intracellular cargoes. (**A**) Schematic of the peroxisomal trafficking assay. The peroxisomal targeting signal (PTS1) of human PEX3 (amino acids 1–42) was fused to mEmerald and FKBP and a truncated NINL (amino acids 1-1062) was fused to FRB. Dynein-dependent accumulation of peroxisomes at the centrosome, where most minus-ends are located, is initiated by the rapalog-mediated heterodimerization of FKBP and FRB. Blue arrow indicates dynein motility. (**B**) Indicated FRB and FKBP constructs transiently expressed with (+) or without (-) the transient co-expression of HA-tagged CVB3 3C^{pro} in HEK293T cells. Immunoblots were probed with anti-FLAG, anti-FKBP, anti-GAPDH and anti-HA antibodies. Protein molecular weight markers are shown in kilodaltons (kDa) to the left of each immunoblot. Representative images from three biological replicates are shown. (**C**) Confocal micrographs are displayed as maximum intensity projections of U-2 OS cells, transfected with Pex3-mEmerald-FKBP and the indicated cleavable or uncleavable NINL-FRB fusion constructs with or without the co-expression of CVB3 3C^{pro}. Where indicated, cells were treated for one hour with ethanol (EtOH) as a control or 1 μM rapalog in EtOH prior to fixation. Centrosomes were immunostained with anti-pericentrin and nuclei were visualized with DAPI. 15 μm scale bars indicated in lower left corner of merged micrographs. Yellow rectangles denote region of cropped inset. Dashed white lines denote cellular boundaries. Representative micrographs from three biological replicates are shown. (**D**) Schematic of the analysis pipeline. (**E**) Quantification of peroxisomal trafficking assays from three biological replicates. The fluorescence intensity of Pex3-mEmerald-FKBP at the centrosome was normalized to the whole-cell fluorescence, and to the areas of the regions of interest used to quantify centrosome versus whole-cell fluorescence. Each datapoint corresponds to an individual cell. The dark grey, large, outlined circles correspond to the mean for each biological replicate. For each condition n = ~80. The mean across all replicates is denoted by the bold line. Data were analyzed using Kruskal–Wallis with Dunn's post hoc test for multiple comparisons. ****$p<0.0001$, ns = not significant.

A

Dynein/Dynactin
NINL
FRB
FKBP
mEmerald
PEX3
Peroxisome
Rapalog
Microtubule
− +

B

NINL-FRB   + + − − − −
NINL triple-FRB   − − + + − −
Pex3-mEmerald-FKBP   − − − − + +
CVB3 3C^pro   − + − + − +

Full length
1032
827
231

225 kDa
115 kDa
85 kDa
65 kDa

α-FLAG

50 kDa
35 kDa
30 kDa
25 kDa

α-FKBP

35 kDa

α-GAPDH

C

+EtOH   +Rapalog

+Empty Vector   +CVB3 3C^pro

NINL-FRB   NINL-FRB   NINL triple-FRB   NINL-FRB   NINL triple-FRB

Pericentrin

FKBP-mEmerald-Pex3

DAPI

Merge

15 µm   15 µm   15 µm   15 µm   15 µm

D

Z-Stack
Max Intensity Projection
Split Channels

Pericentrin
Define centrosome
mEmerald
Measure centrosomal mEmerald

mEmerald
Outline cells
mEmerald
Measure total mEmerald

E

Normalized fluorescence intensity

ns
****

NINL-FRB   + + + − −
Triple-FRB   − − − + +
Rapalog   − + + + +
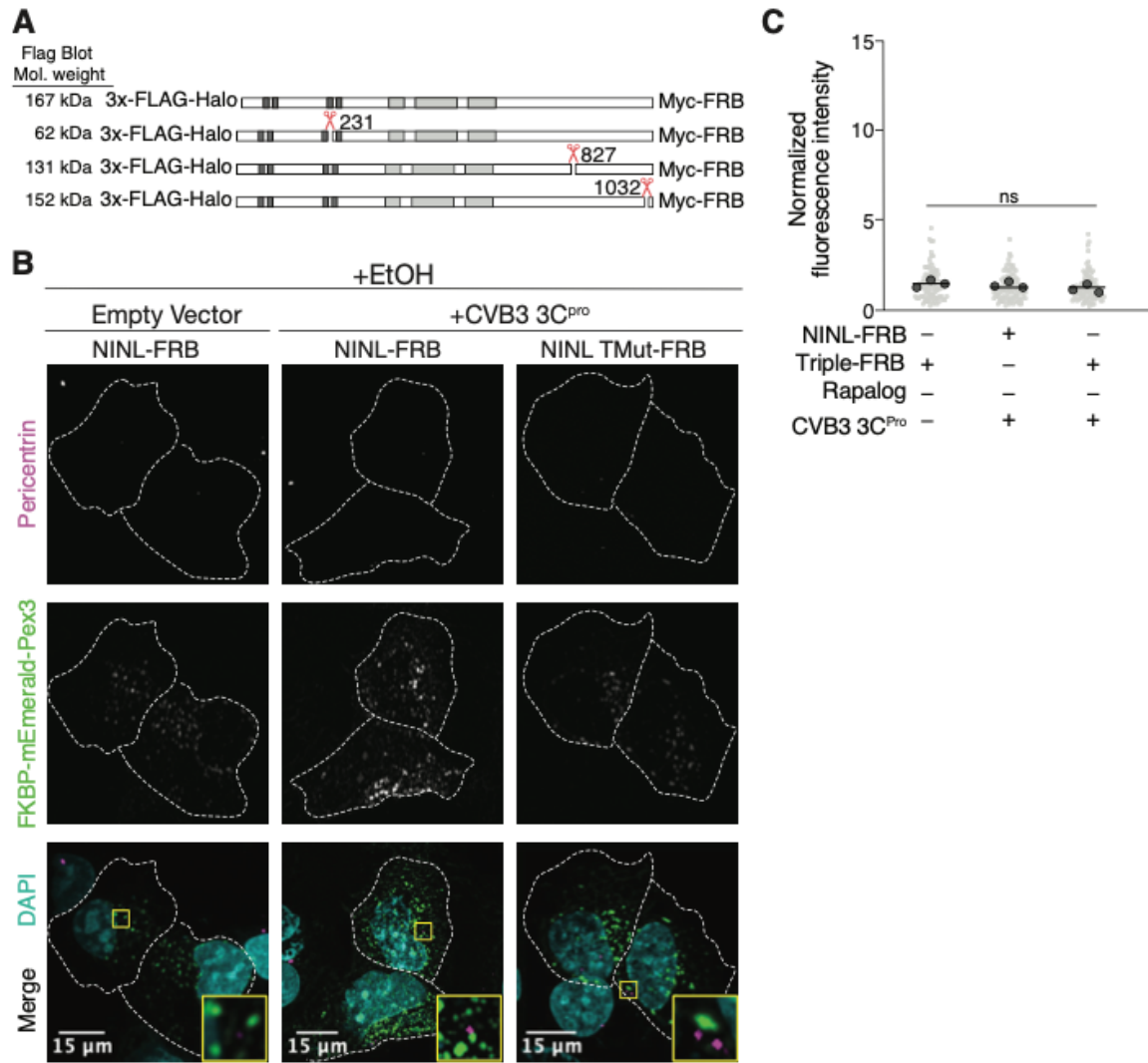CVB3 3C^pro   − − + − +

98

Figure 3.14. Peroxisome distribution remains consistent regardless of presence of CVB3 3Cpro prior to rapalog induced dynein-dependent transport. (**A**) Schematic of NINL-FRB fusion constructs. Predicted molecular weights for each 3xFLAG tagged amino-terminal cleavage product produced by 3C[pro]. (**B**) Peroxisome distribution controls. Confocal micrographs displayed as maximum intensity projections of U-2 OS cells, transfected with Pex3-mEmerald-FKBP and the indicated cleavable or uncleavable NINL-FRB fusion constructs with or without the co-expression of CVB3 3C[pro] treated for one hour with ethanol (EtOH) prior to fixation. Centrosomes were immunostained with anti-pericentrin and nuclei were visualized with DAPI. 15 μm scale bars are indicated in the lower left corner of the merged micrographs. Yellow rectangles denote region of cropped inset. Dashed white lines denote cellular boundaries. Representative micrographs from three biological replicates are shown. (**C**) Quantification of peroxisomal trafficking assay from three biological replicates. The fluorescence intensity of Pex3-mEmerald-FKBP at the centrosome was normalized to the whole-cell fluorescence, and to the areas of the regions of interest used to quantify centrosome versus whole-cell fluorescence. Each datapoint corresponds to an individual cell and biological replicates can be distinguished by shade. For each condition n = ~80. The mean across all replicates is denoted by the bold line. Bold circles correspond to the mean for each biological replicate. Data were analyzed using Kruskal–Wallis with Dunn's post hoc test for multiple comparisons. ns = not significant.

Figure 3.15. Cleavage of NINL during viral infection prevents dynein-dependent transport of an intracellular cargo. (**A**) Confocal micrographs displayed as maximum intensity projections of uninfected or CVB3 infected U-2 OS cells. Cells were transfected with Pex3-mEmerald-FKBP and the indicated cleavable or uncleavable NINL-FRB fusion constructs, and infected (or mock infected) with CVB3 (250,000 PFU/well, MOI = ~2) for five hours. Cells were then treated for one hour with ethanol (EtOH) or 1 μM rapalog prior to fixation. Centrosomes were immunostained with anti-pericentrin and nuclei were visualized with DAPI. 15 μm scale bars are indicated in the lower left corner of the merged micrographs. Yellow rectangles denote region of cropped inset. Dashed white lines denote cellular boundaries. Representative micrographs from three biological replicates are shown. (**B**) Quantification of peroxisomal trafficking assays from three biological replicates. The fluorescence intensity of Pex3-mEmerald-FKBP at the centrosome was normalized to the whole-cell fluorescence, and to the areas of the regions of interest used to quantify centrosome versus whole-cell fluorescence. Each datapoint corresponds to an individual cell and biological replicates can be distinguished by shade. For each condition n = ~80. The mean across all replicates is denoted by the bold line. Bold circles correspond to the mean for each biological replicate. Data were analyzed using Kruskal–Wallis with Dunn's post hoc test for multiple comparisons. ****$p<0.0001$, ns = not significant. (**C**) Schematic of the rapalog-induced pericentrosomal accumulation of peroxisomes and loss of accumulation upon viral infection.
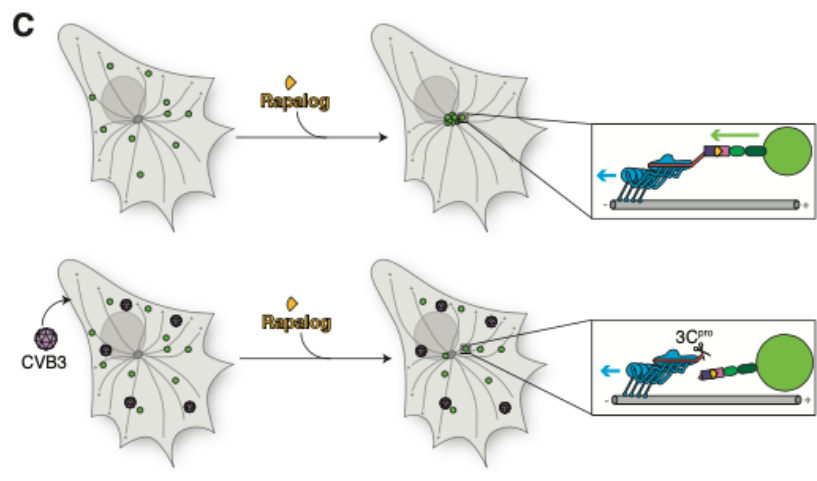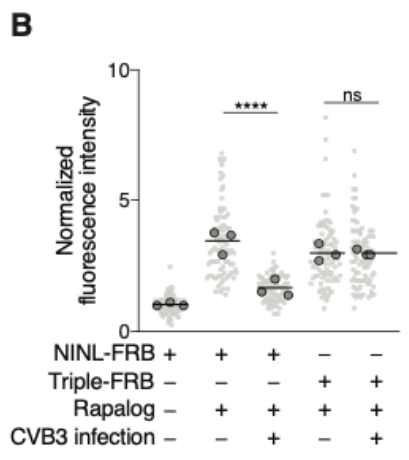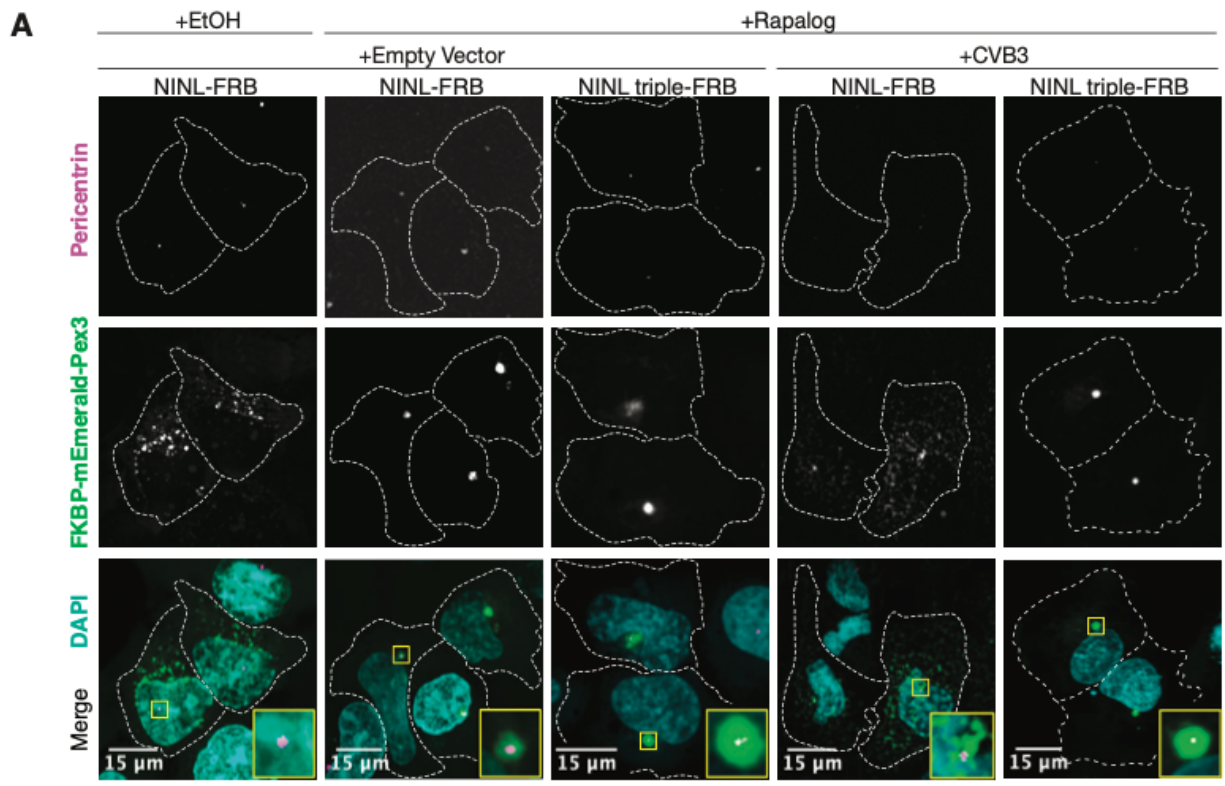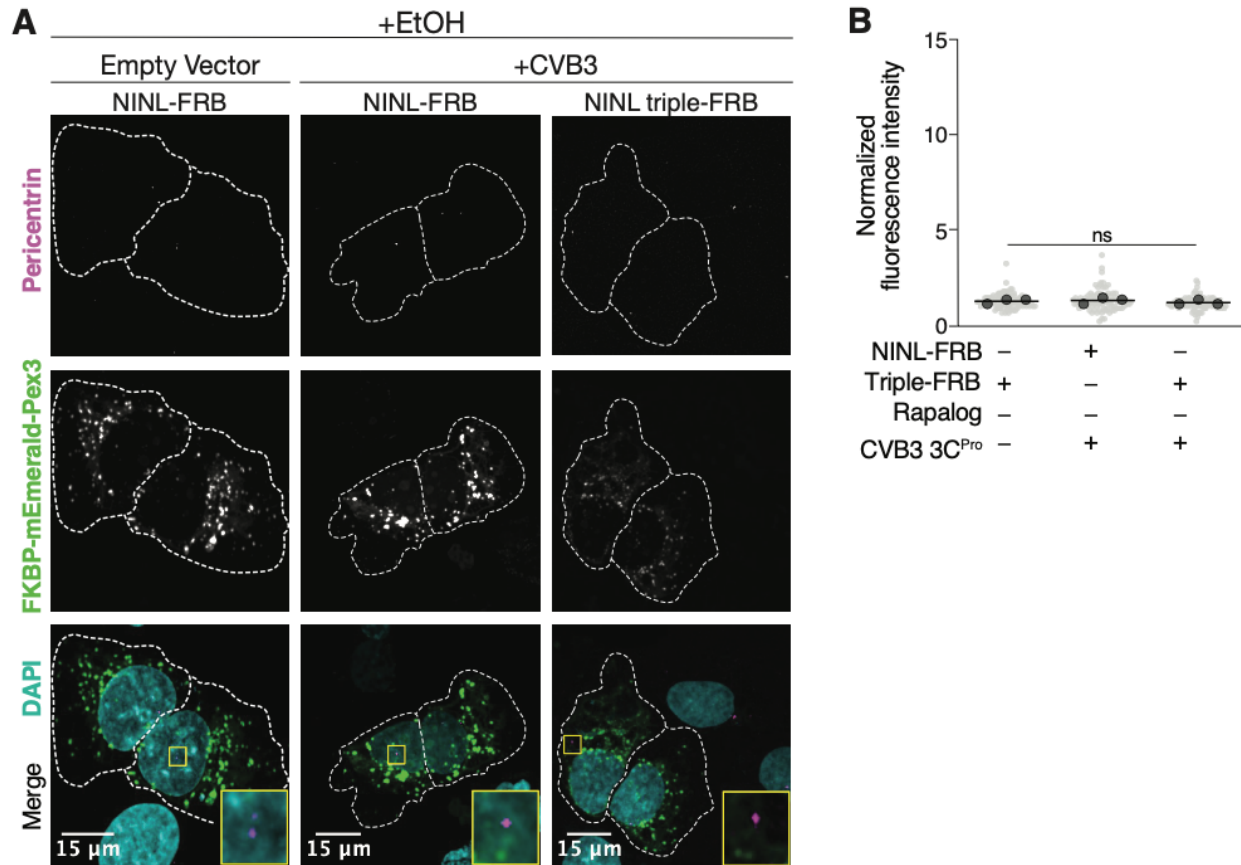
Figure 3.16. Peroxisome distribution remains consistent regardless of CVB3 infection prior to rapalog induced dynein-mediated transport. (**A**) Peroxisome distribution controls. Confocal micrographs displayed as maximum intensity projections of uninfected or CVB3 infected U-2 OS cells expressing Pex3-mEmerald-FKBP and the indicated cleavable or uncleavable NINL-FRB fusion constructs treated for one hour with ethanol (EtOH) prior to fixation. Centrosomes were immunostained with anti-pericentrin and nuclei were stained with DAPI. 15 μm scale bars are indicated in the lower left corner of the merged micrographs. Yellow rectangles denote region of cropped inset. Dashed white lines denote cellular boundaries. Representative micrographs from three biological replicates are shown. (**B**) Quantification of peroxisomal trafficking assays from three biological replicates. Fluorescence intensity of Pex3-mEmerald-FKBP at the centrosome was normalized to the whole-cell fluorescence, and to the areas of the regions of interest used to quantify centrosome versus whole-cell fluorescence. Each datapoint corresponds to an individual cell and biological replicates can be distinguished by shade. For each condition n = ~80. The mean across all replicates is denoted by a bold line. Bold circles correspond to the mean for each biological replicate. Data were analyzed using Kruskal–Wallis with Dunn's post hoc test for multiple comparisons. ns = not significant.

Discussion

Pathogenic viruses and their hosts are engaged in genetic conflicts at every step of the viral life cycle. Each of these points of conflict, which center on direct interactions between viral and host proteins, have the potential to determine the degree to which a virus can replicate and cause pathogenesis in a given host cell, and the degree to which the immune system can inhibit viral replication. As such, evolutionary adaptation in both host and viral genomes shape these molecular interactions, leaving behind signatures of rapid evolution that can serve as beacons for points of host-virus interaction (Daugherty and Malik, 2012; Duggal and Emerman, 2012; Tenthorey et al., 2022). Here we use this evolutionary principle to reveal an antiviral role for the dynein activating adaptor NINL. Unique among 36 analyzed dynein, dynactin, and activating adaptor genes, we found that NINL displays a signature of recurrent positive selection in primates. Based on this unusual evolutionary signature in an otherwise highly conserved cellular machine, we hypothesized that NINL may be engaged in an undescribed host-pathogen conflict. Using multiple cell types and knockout clones, we reveal that loss of NINL results in reduced activation of the antiviral innate immune response following IFNα treatment. Consequently, in NINL KO cells several RNA and DNA viruses show significantly increased replication after IFNα pretreatment relative to WT cells. These results indicate NINL plays an important role in the antiviral immune response.

Further work will be required to determine the mechanistic basis for NINL's antiviral function. The role of activating adaptors in inducing processive dynein motility was only first described in 2014 (McKenney et al., 2014; Schlager et al., 2014). Since that time, the number of established activating adaptors has rapidly expanded, as has our understanding of the molecular

interactions between activating adaptors and dynein/dynactin (Agrawal et al., 2022; Cason et al., 2021; Chaaban and Carter, 2022; Fenton et al., 2021; Lau et al., 2021; Lee et al., 2020; Olenick and Holzbaur, 2019; Reck-Peterson et al., 2018). However, for many activating adaptors, including NINL, much less is known about cargo specificity. Our observation that NINL KO cells have a defect in ISG production following IFNα treatment, despite normal phosphorylation of the STAT1 and STAT2 transcription factors, suggests a role for NINL in the IFN signaling pathway. However, whether a signaling complex is a direct cargo of NINL, or whether NINL's interaction with dynein and dynactin is required for this function, remain to be determined.

Notably, we observe several transcriptional changes in NINL KO cells relative to WT cells, suggesting that NINL plays regulatory roles in the cell beyond our observation of its role in the IFN effect. Like other activating adaptors, understanding the full range of cargos and biological functions of NINL will require additional studies.

Despite the uncertainty of NINL's mechanistic role in the antiviral immune response, we find that several viruses can antagonize NINL function through proteolytic cleavage. Using the model enterovirus, CVB3, we show that the virally-encoded 3C protease (3C^{pro}) cleaves NINL at multiple sites, all of which toggle between cleavable and uncleavable even within the primate clade. These changes within the cleavage sites of NINL in primates suggest that virally-encoded proteases are one potential evolutionary pressure that is driving the rapid evolution of NINL (that differentiates it from other components of the dynein machinery). Related 3C^{pros} from other picornaviruses, as well as 3CL^{pros} from coronaviruses, also cleave NINL. Intriguingly, even closely related proteases, for instance within the enterovirus clade, have different site preferences within NINL, suggesting that viral protease evolution may be shaping its interactions with NINL.

Indeed, among the diversity of picornavirus and coronavirus proteases we tested, we find that that NINL cleavage is maintained despite a wide array of site preferences and cleavage efficiencies. Compellingly, cleavage of NINL by 3C^{pro} during viral infection disrupts the NINL-mediated transport of a heterologous cargo. Along with our data indicating that one function of NINL is to potentiate the innate immune response, these data suggest that cleavage of NINL could be a mechanism employed by viruses to dampen the interferon response to promote their own replicative success.

Altogether, our study demonstrates the effectiveness of leveraging genetic signatures of pathogen-driven evolution to identify new components of host innate immunity. Our insights into the conflict between viruses and NINL provides a glimpse into the impact that viruses may have on the evolution of the intracellular transport machinery and identify a new role for a dynein activating adaptor in the antiviral immune response. These results indicate that components of the otherwise conserved cytoplasmic dynein transport machinery can be engaged in host- and virus-specific interactions and suggest intracellular transport could be an important battleground for host-virus arms races.

Materials and Methods

Evolutionary Analysis

For evolutionary analyses of dynein, dynactin, and activating adaptor genes, Uniprot reference protein sequences were used as a search query against NCBI's non-redundant (NR) database using tBLASTn (Altschul et al., 1990). For each primate species, the nucleotide sequence with the highest bit score was downloaded and aligned to the human ORF nucleotide

sequence using MAFFT (Katoh, 2002) implemented in Geneious software (Dotmatics; geneious.com). Poorly aligning sequences or regions were removed from subsequent analyses. Maximum likelihood (ML) tests were performed with codeml in the PAML software suite (Yang, 2007). Aligned sequences were subjected to ML tests using NS sites models disallowing (M7) or allowing (M8) positive selection. The p-value reported is the result of a chi-squared test on twice the difference of the log likelihood (lnL) values between the two models using two degrees of freedom. Analyses were performed using two models of frequency (F61 and F3x4) and both sets of values are reported. For each codon model, we confirmed convergence of lnL values by performing each analysis using two starting omega (dN/dS) values (0.4 and 1.5). For evolutionary analyses of the isolated NINL amino-terminal (dynein/dynactin binding) and carboxy-terminal (cargo binding) regions, the full-length alignment was truncated to only include codons 1-702 or 703-1382 respectively and PAML analyses were performed as described above.

We used three independent methods to estimate codons within NINL that have been subject to positive selection. PAML was used to identify positively selected codons with a posterior probability greater than 0.90 using a Bayes Empirical Bayes (BEB) analysis and the F61 codon frequency model. The same NINL alignment was also used as input for FEL (Kosakovsky Pond and Frost, 2005) and MEME (Murrell et al., 2012) using the DataMonkey (Weaver et al., 2018) server. In both cases, default parameters were used and codons with a signature of positive selection with a p-value of <0.1 are reported. In all cases, codon numbers correspond to the amino acid position and residue in human NINL (NCBI accession NM_025176.6).

Molecular Cloning

For the plasmid-based CRISPR/Cas9-mediated knockout of NIN and NINL we designed gRNA target sequences with the web tool CHOPCHOP (Labun et al., 2016), available at chopchop.cbu.uib.no, and synthesized oligonucleotides from Eton Biosciences (San Diego, CA, USA). Each oligonucleotide pair was phosphorylated and annealed using the T4 Polynucleotide Kinase (New England Biolabs, Ipswich, MA, USA). Duplexed oligonucleotides were ligated into BbsI (New England Biolabs) digested pSpCas9(BB)-2A- Puro (pX459) V2.0, a gift from Feng Zhang (Addgene plasmid #62988), using the Quick Ligase kit (New England Biolabs). For cleavage assays, the coding sequence of human NINL isoform 1 (NCBI accession NM_025176.6) was subcloned from the previously described pcDNA5/FRT/TO-BioID-NINL-3xFLAG (Redwine et al., 2017) and inserted into pcDNA5/FRT/TO with as part of the following cassette: mCherry-P2A-3xFLAG-NINL-Myc. NINL mutants (Q1032R, Q827/1032R, Q231/827/1032R), human NINL isoform 2 (NCBI accession NM_001318226.2) and the NINL isoform 2 mutant (Q231R) were mutagenized using the Q5 Site-Directed Mutagenesis Kit (New England BioLabs). The plasmids encoding 3C proteases (coxsackievirus B3 (CVB3) 3C^{pro}, catalytically inactive (C147A) CVB3 3C^{pro}, enterovirus A71 (EV71) 3C^{pro}, poliovirus 1 (PV1) 3C^{pro}, enterovirus D68 (EV68) 3C^{pro}, human rhinovirus A (HRVA) 3C^{pro}, encephalomyocarditis virus (EMCV) 3C^{pro}, parechovirus A (Parecho) 3C^{pro}, hepatitis A virus (HepA) 3C^{pro}, and salivirus A (Sali) 3C^{pro}) have been described previously (Tsu et al., 2021). To ensure that 3CL^{pros} have precise amino- and carboxy-termini as a result of self-cleavage, sequences for 3CL proteases (SARS2 3CL^{pro}, SARS1 3CL^{pro}, and NL63 3CL^{pro}), including nine residues from the upstream coding region (nsp4) and downstream coding region (nsp6) were ordered as gBlocks (Integrated DNA Technologies, Coralville, IA) (Supplementary File 3.5) and cloned into the pQCXIP

backbone flanked by an N-terminal eGFP and a C-terminal mCherry-HA sequence. Catalytically

inactive (C145A) SARS2 3CL^{pro} was made using overlapping stitch PCR. For the peroxisome

trafficking assay, the peroxisomal membrane-targeting sequence (amino acids 1–42) of human

PEX3 (NCBI accession NM_003630) with a carboxy-terminal mEmerald fluorescent protein and

FKBP was subcloned from the previously described pcDNA5-PEX3-Emerald-FKBP (Htet et al.,

2020) and into the pcDNA3.1(+) backbone. 3xFLAG-Halo-NINL(1-1062)-Myc-FRB was

synthesized as a gBlock (Integrated DNA Technologies) and cloned into the pcDNA3.1(+)

backbone. To generate an uncleavable mutant of this construct we used sequential Q5

mutagenesis to achieve Q231/827/1032R. Following cloning, all plasmids were verified with

whole plasmid sequencing. Plasmids and primers used in this study can be found in

Supplementary File 3.5.

Transfections

All transfections in this study were performed with TransIT-X2® Transfection Reagent

(Mirus Bio, Madison, WI, USA) according to the manufacturer's instructions. Briefly, 18-24

hours prior to transfection the desired cells were plated at an appropriate density such that they

would be ≥80% confluent at time of transfection. TransIT-X2:DNA complexes were formed

following the manufacturer's protocol. The TransIT-X2:DNA complexes were then evenly

distributed to cells via drop-wise addition and were incubated in a humidified 5% CO_2

atmosphere at 37°C for until they were harvested, assayed, or placed into selection as described

below.

Cell lines

All cell lines used in this study were sourced from the American Type Culture Collection (ATCC; Manassas, VA) unless otherwise indicated and maintained in a humidified 5% CO_2 atmosphere at 37°C. All cell lines are routinely tested for mycoplasma by PCR kit (ATCC). HEK293T (human embryonic kidney epithelial cells, ATCC CRL-3216), A549 (human alveolar adenocarcinoma cells, ATCC CCL-185), U-2 OS (human epithelial osteosarcoma cells, ATCC HTB-96), BSC40 (grivet kidney epithelial cells, ATCC CRL-2761), Vero (African green monkey kidney epithelial cells, ATCC CCL-81), and BHK-21 (Syrian golden hamster kidney fibroblast cells, ATCC CCL-10) were maintained in complete growth media which is composed of Dulbecco's Modified Eagle's Medium with 4.5g/L glucose, L-glutamine, and sodium pyruvate (DMEM; Corning, Manassas, VA, USA) supplemented with 10% (v/v) fetal bovine serum (FBS; Gibco, Grand Island, NY, USA) and 1% (v/v) Penicillin/Streptomycin (PenStrep; Corning). Flp-In™ T-REx™ HCT116 (human colorectal carcinoma cells) were a gift from E. Bennett at the University of California San Diego (La Jolla, CA, USA) but originated in the laboratory of B. Wouters at the University of Toronto (Toronto, ON, Canada) and were maintained in complete growth media supplemented with 100 μg/ml Zeocin. Cells are routinely tested for mycoplasma contamination using mycoplasma by PCR kit (ATCC, Manassas, VA) and kept at low passage to maintain less than one year since acquisition or generation.

CRISPR/Cas9-mediated gene editing

To generate NIN and NINL knock outs in A549, HCT116 and U-2 OS cell lines, the cells were transfected with 250 ng of the pX459 vector containing the appropriate gRNAs. Transfected cells were enriched 48 hours post-transfection by culturing them with complete growth media supplemented with 1 μg/ml puromycin for 48 hours and then were allowed to

recover for 24 hours in complete growth media without puromycin. Following enrichment of transfected cells, monoclonal cell lines were obtained by expanding single-cell clones isolated by limiting dilution. The resulting clones were screened via immunoblotting with gene-specific antibodies anti-NINL rabbit polyclonal antibody (Thermo Fisher Scientific, Waltham, MA,USA) and anti-NIN mouse monoclonal antibody (LSBio, Seattle, WA, USA). Clones determined to be knockouts via immunoblotting were screened further to confirm the presence of CRISPR-induced indels in each allele of the targeted gene. Genomic DNA was isolated using the *DNeasy Blood & Tissue Kit* (Qiagen, Hilden, Germany) and the target exons were amplified with Econo*Taq* polymerase (Lucigen, Middleton, WI, USA). The resulting amplicons were subcloned using the TOPO TA Cloning Kit for Sequencing (Thermo Fisher Scientific) and transformed into DH5α competent cells. Single colonies were picked, and the plasmids were isolated by miniprep (Qiagen) and sequenced individually using T3 and T7-Pro primers.

Immunoblotting

Harvested cell pellets were washed with 1X PBS, and unless otherwise noted, lysed with RIPA lysis buffer: 50 mM 2-Amino-2-(hydroxymethyl)propane-1,3-diol (Tris), pH 7.4; 150 mM sodium chloride (NaCl); 1% (v/v) Octylphenyl-polyethylene glycol (IGEPAL CA-630); 0.5% (w/v) Sodium Deoxycholate (DOC); and 0.1% (w/v) Sodium Dodecyl Sulfate (SDS); 1 mM Dithiothreitol (DTT); and cOmplete Protease Inhibitor Cocktail (Roche, Basel, Switzerland) at 4°C for 10 minutes with end-over-end rotation. Lysates were then centrifuged at maximum speed in a 4°C microcentrifuge for 10 min. The supernatants were transferred to new microcentrifuge tubes and supplemented with NuPage LDS sample buffer (Invitrogen, Carlsbad, CA) and NuPage reducing agent (Invitrogen) prior to a 10 minute heat denaturation at 95°C. Lysates were

resolved on a 4–12% Bis-Tris SDS-PAGE gel (Life Technologies, San Diego, CA), followed by

wet transfer to PVDF membranes (Bio-Rad, Hercules, CA) for 4 hours at 85V using Towbin

buffer: 25mM Tris base, pH 9.2; 192 mM Glycine; 20% (v/v) Methanol. Immunoblots were

blocked with 5% (w/v) blotting grade nonfat dry milk (Apex Bioresearch Products) in TBS-T: 20

mM Tris pH 7.4; 150 mM NaCl, 0.1% Polysorbate 20 (Tween 20) for 1 hour. Primary antibodies

were diluted in TBS-T supplemented with 5% (w/v) BSA and rocked overnight. Primary

antibody adsorbed membranes were rinsed three times in TBS-T and subsequently incubated

with the appropriate HRP-conjugated secondary antibodies. Membranes were rinsed again three

times in TBS-T and developed with SuperSignal West Pico PLUS Chemiluminescent Substrate

(Thermo Fisher Scientific) on a ChemiDoc MP Imaging System (Bio-Rad) using Imagelab (Bio-

Rad) software. Specifications for antibodies are described in Supplementary File 3.6.

The ability of Cas9 Control, NINL KO, and NIN KO to respond to IFNα was assayed by

first culturing cells in the presence or absence of 1000U IFNα. Eighteen hours post-treatment

with IFNα the cells were harvested, lysed and immunoblotted as described above for STAT1,

Phospho-STAT1 (Tyr701), STAT2, Phospho-STAT2 (Tyr690), MX1, IFIT3, OAS1, and ISG15

(Supplementary File 3.6).

RNASeq and analysis

Total RNA from mock-treated or IFNα-treated cell lines (1000 U, 24 hour treatment) was

extracted using an RNeasy Plus Mini Kit (Qiagen) as indicated in the manufacturer's protocol.

The Illumina Stranded mRNA prep kit was used to generate dual-indexed cDNA libraries and

the resulting libraries were sequenced on an Illumina NovaSeq 6000 instrument. Total RNA was

assessed for quality using an Agilent Tapestation 4200, and samples with an RNA Integrity

Number (RIN) greater than 8.0 were used to generate RNA sequencing libraries using the TruSeq Stranded mRNA Sample Prep Kit with TruSeq Unique Dual Indexes (Illumina, San Diego, CA). Samples were processed following manufacturer's instructions, starting with 500 ng of RNA and modifying RNA shear time to five minutes. Resulting libraries were multiplexed and sequenced with 100 basepair (bp) paired end reads (PE100) to a depth of approximately 25 million reads per sample on an Illumina NovaSeq 6000 instrument. Samples were demuxltiplexed using bcl2fastq v2.20 Conversion Software (Illumina, San Diego, CA). Sequencing reads were quantified with Salmon (Patro et al., 2017) in a quasi-mapping-based mode to the reference genome. Read quantifications were imported and differentially expressed genes across experimental conditions were identified using the R package DESeq2 (Love et al., 2014). Reactome pathway analysis was performed by inputting the list of genes with significantly lower expression (adjusted p-value ≤0.05, $\log_2$-fold change ≤-1) in NINL KO cells treated with IFNα relative to WT cells treated with IFNα into the "Analyze Gene List" tool at reactome.org (Jassal et al., 2020).

Viral stocks

CVB3 and EMCV viral stocks were generated by co-transfection of CVB3-Nancy or EMCV-Mengo infectious clone plasmids with a plasmid expressing T7 RNA polymerase (generous gifts from Dr. Julie Pfeiffer, UT Southwestern) as previously described (McCune et al., 2020). The supernatant was harvested, quantified by plaque assay on Vero cells (CVB3) (see below) or TCID50 on HEK293Tcells (EMCV), and frozen in aliquots at −80°C. Wild-type vaccinia virus Western Reserve strain (VacV WT) and the J3 cap1-methlytransferase K175R vaccinia virus mutant (VacV J3) were gifts from Dr. Richard Condit (University of Florida).

VacV was amplified in BHK cells and quantified by plaque assay as described below. VSV-GFP (gift from Dr. John Rose (Yale University)) was amplified in BSC40s and quantified by plaque assay as described below. Sindbis virus (SinV) was generated by electroporation of *in vitro* transcribed RNA from plasmid SINV TE/5′2J-GFP (from Dr. Charles Rice, Rockefeller University) into BHK cells as previously described (Bick et al., 2003) and quantified by plaque assay on BHK cells as described below.

Viral infection and quantification

For quantification of VSV and SinV, cells (as indicated in each experiment) were seeded in 24-well plates and grown overnight, followed by the addition of 2,500 plaque forming units (PFU)/well of VSV or 250,000 PFU/well SinV. Nine hours after infection for VSV or 24 hours after infection for SinV, viral supernatant was harvested from infected cells. The resulting supernatant was serially 10-fold diluted in 24-well plates in DMEM containing 10% FBS and overlaid on BHK cells (ATCC) at 80% confluency for 1 hour. Supernatant was removed from cells 60-120 minutes post-infection and cells were overlaid with complete DMEM media containing 0.8% carboxymethyl cellulose (MilliporeSigma, Burlington, MA, USA). After 24 hours, the overlay was aspirated and the cells were stained with 0.1% Crystal Violet in 20% ethanol, and then de-stained with 20% ethanol. Viral concentrations were determined by manually counting plaques.

For quantification of CVB3, cells (as indicated in each experiment) were seeded in 24-well plates and grown overnight, followed by the addition of 25,000 PFU/well virus. Twenty-four hours after infection, viral supernatant was harvested from the infected cells, serially 10-fold diluted in 12-well plates in DMEM containing 10% FBS and overlaid on Vero cells (ATCC) at

80% confluency for 1 hour. Supernatant was removed from cells 60-120 minutes post-infection and cells were overlaid with complete DMEM media containing 1% agarose (Fisher Scientific) and 1 mg/mL neomycin (Research Products International, Mount Prospect, IL, USA) to enhance plaque visualization (Woods Acevedo et al., 2019). After 48 hours, agarose plugs were washed out with water and the cells were stained with 0.1% Crystal Violet in 20% ethanol, and then de-stained with 20% ethanol. Viral concentrations were determined by manually counting plaques.

For quantification of VacV WT and VacV J3, cells (as indicated in each experiment) were seeded in 24-well plates and grown overnight, followed by the addition of 25,000 PFU/well virus. Twenty-four hours after infection, cell-associated virus was harvested by freeze-thaw lysis of the infected cells. Following pelleting of cell debris, virus-containing supernatant was serially 10-fold diluted in 24-well plates in DMEM containing 10% FBS and overlaid on BSC40 cells (ATCC) at 80% confluency. After 48 hours, the medium was aspirated, and the cells were stained with 0.1% Crystal Violet in 20% ethanol, and then de-stained with 20% ethanol. Viral concentrations were determined by manually counting plaques.

Prediction of NINL cleavage sites by enterovirus 3C^{pro}

Putative enterovirus 3C^{pro} cleavage sites within human NINL were predicted using a previously generated polyprotein cleavage motif (Tsu et al., 2021) constructed from >500 non-redundant enterovirus polyprotein sequences. A FIMO motif search against human NINL was conducted using a 0.002 p-value threshold, which we previously determined was sufficient to capture of 95% of enterovirus cleavage sites (Tsu et al., 2021). To enrich for cleavage sites that may be species-specific, sites in which there is variability in the P1 or P1' sites, which are the primary determinants of cleavage specificity (Tsu et al., 2021), are reported.

NINL protease cleavage assays

HEK293T cells were co-transfected with 100 ng of epitope-tagged human WT NINL, the NINL double mutant (Q827R, Q1032R), the NINL triple mutant (Q231R, Q827R, Q1032R), NINL isoform 2 or the NINL isoform 2 mutant (Q231R) and with 250 ng of HA-tagged protease-producing constructs for 3C^{pro} assays or 5 ng for 3CL^{pro} assays. Twenty-four hours post-transfection, the cells were harvested, lysed in 1x NuPAGE LDS sample buffer (Invitrogen) containing 5% β-mercaptoethanol (Thermo Fisher Scientific) and immunoblotted as described above.

NINL virus cleavage assays

HEK293T cells were transfected with 100 ng of epitope tagged human WT NINL, the NINL double mutant (Q827R, Q1032R), the NINL triple mutant (Q231R, Q827R, Q1032R), NINL isoform 2 or the NINL isoform 2 mutant (Q231R). At 24 h post-transfection, cells were infected with CVB3 or EMCV at a concentration of 250,000 PFU/well. Nine hours post-infection, the cells were harvested, lysed in 1x NuPAGE LDS sample buffer (Invitrogen) containing 5% β-mercaptoethanol (Thermo Fisher Scientific) and immunoblotted as described above.

Immunofluorescence

Cells were grown on fibronectin-coated acid-washed #1.5 glass coverslips. As applicable, cells underwent the desired treatment prior to a brief permeabilization with 300 μl of 0.5 % TritonX-100 (MilliporeSigma) in PHEM buffer: 60 mM piperazine-N,N′-bis(2-ethanesulfonic

acid) (PIPES), 25 mM 4-(2-hydroxyethyl)-1-piperazineethanesulfonic acid (HEPES), 10 mM

Ethylene glycol-bis(2-aminoethylether)-N,N,N′,N′-tetraacetic acid (EGTA), and 4 mM

magnesium sulfate heptahydrate (MgSO$_4$·7H$_2$0). After five minutes, 100 µl of a 4% (v/v)

formaldehyde (Electron Microscopy Sciences, Hatfield, PA) and 0.5% (v/v) glutaraldehyde

(Electron Microscopy Sciences) in PHEM solution was added slowly to the cells and allowed to

incubate. After two minutes, all buffer was aspirated from the cells and replaced with the same

4% (v/v) formaldehyde and 0.5% (v/v) glutaraldehyde in PHEM solution and incubated for 20

minutes at 37 °C. After this incubation, the cells were washed three times for five minutes each

in PHEM-T (PHEM + 0.1 % TritonX-100). The cells were then blocked for one hour with a 5%

secondary-matched serum solution in PHEM supplemented with 30 mM glycine. The blocking

solution was then removed and the desired primary antibodies were added and incubated

overnight at 4 °C. The following day the cells were washed three times for five minutes in

PHEM-T and immunostained with the appropriate secondary antibodies for one hour at room

temperature. The cells were then washed with PHEM-T and counter-stained with 4′,6-diamidino-

2-phenylindole (DAPI, Biotium, Fremont, CA). The cells and coverslips were mounted on glass

slides with Prolong Glass Antifade Mountant (Thermo Scientific). See Supplementary File 3.2

for a list of all antibodies.

Confocal microscopy

Cells were imaged using a CSU-W1 spinning disk confocal scanner unit (Yokogawa

Electric Corporation, Musashino, Tokyo, Japan) coupled to a six-line (405 nm, 445nm, 488 nm,

514nm, 561 nm, and 640 nm) LUN-F-XL laser engine (Nikon Instruments Incorporated,

Melville, NY, USA). Emission light from the DAPI, Alexa Fluor 561, and Alexa Fluor 647 was

filtered using a quad primary dichroic (405/488/568/647nm; Semrock, Rochester, NY, USA) and individual bandpass emission filters mounted within the W1 scan head for each channel (450/50, 595/50, and 700/70; Chroma Technology Corporation, Bellows Falls, VT). The W1 was mounted on a Nikon Ti2-E and an Apo TIRF 60x 1.49 NA objective was used to collect images. Image stacks were acquired using a piezo Z-insert (Mad City Labs, Madison, WI, USA). Illumination and image acquisition was controlled by NIS Elements Advanced Research software (Nikon Instruments Incorporated).

Peroxisome trafficking assay

For imaging of peroxisome accumulation at the centrosome in the presence or absence of $3C^{pro}$ or CVB3 infection, 25,000 U-2 OS cells were plated on fibronectin-coated coverslips and incubated overnight. For $3C^{pro}$ transfected experiments, cells were transfected with the PEX3-Emerald-FKBP construct and either the cleavable NINL-FRB construct or the uncleavable NINL triple mutant construct with or without co-transfection of CVB3 $3C^{pro}$. Eighteen hours after transfection, the cells were treated with or without 1 μM rapalog (Takara Bio) for one hour prior to fixation. For CVB3 infections experiments, the cells were only transfected with the PEX3-Emerald-FKBP construct and either the cleavable NINL-FRB construct or the uncleavable NINL triple mutant construct. Eighteen hours after transfection, cells were infected with 250,000 PFU (MOI ~ 2) or mock infected. Five hours later, cells were treated with or without 1 μM rapalog for one hour (for a total of six hours of infection) prior to fixation. Cells from both $3C^{pro}$ experiments and CVB3 infection experiments were fixed and immunostained as described above. Specifically, the centrosome was immunostained with anti-pericentrin rabbit polyclonal antibodies, goat anti-rabbit IgG (H + L) Alexa Fluor-647 (Thermo Fisher Scientific) and

117

counterstained with DAPI prior to mounting. Z-stacks were acquired using a piezo Z stage. Separate image channels were acquired sequentially using bandpass filters for each channel DAPI: 455/50, PEX3-Emerald-FKBP: 525/50, pericentrin: 705/75.

Max intensity projections of Z-stacks were created in FIJI for each separate channel to quantify the peroxisome accumulation at the centrosome. The brightest pericentrin puncta in the 647 channel was identified as the centrosome, and a 60 pixel-wide circle was drawn around it to create a region of interest (ROI). A whole cell ROI was then manually drawn by adjusting the brightness/contrast module's "Maximum" slider to saturate cellular boundaries. The fluorescence intensity at the centrosome and throughout the cell was then quantified by applying each ROI to the PEX3-Emerald-FKBP/488 channel. The percentage of total fluorescence present at the centrosome was calculated by dividing the intensity of fluorescence at the centrosome by the intensity of fluorescence throughout the cell. The area of the centrosome ROI was then divided by the area of the whole cell ROI to calculate the percentage of the cell's area that the centrosome ROI comprised. The fluorescence intensity ratio was then divided by the area ratio and plotted using GraphPad Prism. Kruskal–Wallis with Dunn's post hoc test for multiple comparisons was performed using GraphPad Prism.

Acknowledgments

References

Agrawal R, Gillies JP, Zang JL, Zhang J, Garrott SR, Shibuya H, Nandakumar J, DeSantis ME. 2022. The KASH5 protein involved in meiotic chromosomal movements is a novel dynein activating adaptor (preprint). Cell Biology. doi:10.1101/2022.03.11.483947

Altschul SF, Gish W, Miller W, Myers EW, Lipman DJ. 1990. Basic local alignment search tool. *Journal of Molecular Biology* **215**:403–410. doi:10.1016/S0022-2836(05)80360-2

Bachmann-Gagescu R, Dona M, Hetterschijt L, Tonnaer E, Peters T, de Vrieze E, Mans DA, van Beersum SEC, Phelps IG, Arts HH, Keunen JE, Ueffing M, Roepman R, Boldt K, Doherty D, Moens CB, Neuhauss SCF, Kremer H, van Wijk E. 2015. The Ciliopathy Protein CC2D2A Associates with NINL and Functions in RAB8-MICAL3-Regulated Vesicle Trafficking. *PLoS Genet* **11**:e1005575. doi:10.1371/journal.pgen.1005575

Beachboard DC, Horner SM. 2016. Innate immune evasion strategies of DNA and RNA viruses. *Current Opinion in Microbiology* **32**:113–119. doi:10.1016/j.mib.2016.05.015

Bick MJ, Carroll J-WN, Gao G, Goff SP, Rice CM, MacDonald MR. 2003. Expression of the zinc-finger antiviral protein inhibits alphavirus replication. *J Virol* **77**:11555–11562. doi:10.1128/jvi.77.21.11555-11562.2003

Brandenburg B, Zhuang X. 2007. Virus trafficking - learning from single-virus tracking. *Nature reviews Microbiology* **5**:197–208.

Casenghi M, Meraldi P, Weinhart U, Duncan PI, Körner R, Nigg EA. 2003. Polo-like kinase 1 regulates Nlp, a centrosome protein involved in microtubule nucleation. *Developmental cell* **5**:113–125.

Cason SE, Carman PJ, Van Duyne C, Goldsmith J, Dominguez R, Holzbaur ELF. 2021. Sequential dynein effectors regulate axonal autophagosome motility in a maturation-dependent pathway. *Journal of Cell Biology* **220**:e202010179. doi:10.1083/jcb.202010179

Chaaban S, Carter AP. 2022. Structure of dynein-dynactin on microtubules shows tandem recruitment of cargo adaptors (preprint). Molecular Biology. doi:10.1101/2022.03.17.482250

Daffis S, Szretter KJ, Schriewer J, Li J, Youn S, Errett J, Lin T-Y, Schneller S, Zust R, Dong H, Thiel V, Sen GC, Fensterl V, Klimstra WB, Pierson TC, Buller RM, Gale Jr M, Shi P-Y, Diamond MS. 2010. 2′-O methylation of the viral mRNA cap evades host restriction by IFIT family members. *Nature* **468**:452–456. doi:10.1038/nature09489

Daugherty MD, Malik HS. 2012. Rules of Engagement: Molecular Insights from Host-Virus Arms Races. *Annual Review of Genetics* **46**:677–700. doi:10.1146/annurev-genet-110711-155522

Daugherty MD, Schaller AM, Geballe AP, Malik HS. 2016. Evolution-guided functional analyses reveal diverse antiviral specificities encoded by IFIT1 genes in mammals. *eLife* **5**:e14228. doi:10.7554/eLife.14228

Dodding MP, Way M. 2011. Coupling viruses to dynein and kinesin-1. *The EMBO journal* **30**:3527–3539.

Döhner K, Nagel C-H, Sodeik B. 2005. Viral stop-and-go along microtubules: taking a ride with dynein and kinesins. *Trends in microbiology* **13**:320–327.

Dona M, Bachmann-Gagescu R, Texier Y, Toedt G, Hetterschijt L, Tonnaer EL, Peters TA, van Beersum SEC, Bergboer JGM, Horn N, de Vrieze E, Slijkerman RWN, van Reeuwijk J, Flik G, Keunen JE, Ueffing M, Gibson TJ, Roepman R, Boldt K, Kremer H, van Wijk E. 2015. NINL and DZANK1 Co-function in Vesicle Transport and Are Essential for Photoreceptor Development in Zebrafish. *PLoS genetics* **11**:e1005574.

Duggal NK, Emerman M. 2012. Evolutionary conflicts between viruses and restriction factors shape immunity. *Nat Rev Immunol* **12**:687–695. doi:10.1038/nri3295

Enard D, Cai L, Gwennap C, Petrov DA. 2016. Viruses are a dominant driver of protein adaptation in mammals. *Elife* **5**. doi:10.7554/eLife.12469

Enard D, Petrov DA. 2018. Evidence that RNA Viruses Drove Adaptive Introgression between Neanderthals and Modern Humans. *Cell* **175**:360-371.e13. doi:10.1016/j.cell.2018.08.034

Fenton AR, Jongens TA, Holzbaur ELF. 2021. Mitochondrial adaptor TRAK2 activates and functionally links opposing kinesin and dynein motors. *Nat Commun* **12**:4578. doi:10.1038/s41467-021-24862-7

Gordon DE, Jang GM, Bouhaddou M, Xu J, Obernier K, White KM, O'Meara MJ, Rezelj VV, Guo JZ, Swaney DL, Tummino TA, Hüttenhain R, Kaake RM, Richards AL, Tutuncuoglu B, Foussard H, Batra J, Haas K, Modak M, Kim M, Haas P, Polacco BJ, Braberg H, Fabius JM, Eckhardt M, Soucheray M, Bennett MJ, Cakir M, McGregor MJ, Li Q, Meyer B, Roesch F, Vallet T, Mac Kain A, Miorin L, Moreno E, Naing ZZC, Zhou Y, Peng S, Shi Y, Zhang Z, Shen W, Kirby IT, Melnyk JE, Chorba JS, Lou K, Dai SA, Barrio-Hernandez I, Memon D, Hernandez-Armenta C, Lyu J, Mathy CJP, Perica T, Pilla KB, Ganesan SJ, Saltzberg DJ, Rakesh R, Liu X, Rosenthal SB, Calviello L, Venkataramanan S, Liboy-Lugo J, Lin Y, Huang X-P, Liu Y, Wankowicz SA, Bohn M, Safari M, Ugur FS, Koh C, Savar NS, Tran QD, Shengjuler D, Fletcher SJ, O'Neal MC, Cai Y, Chang JCJ, Broadhurst DJ, Klippsten S, Sharp PP, Wenzell NA, Kuzuoglu-Ozturk D, Wang H-Y, Trenker R, Young JM, Cavero DA, Hiatt J, Roth TL, Rathore U, Subramanian A, Noack J, Hubert M, Stroud RM, Frankel AD, Rosenberg OS, Verba KA, Agard DA, Ott M, Emerman M, Jura N, von Zastrow M, Verdin E, Ashworth A, Schwartz O, d'Enfert C, Mukherjee S, Jacobson M, Malik HS, Fujimori DG, Ideker T, Craik CS, Floor SN, Fraser JS, Gross JD, Sali A, Roth BL, Ruggero D, Taunton J,

Kortemme T, Beltrao P, Vignuzzi M, García-Sastre A, Shokat KM, Shoichet BK, Krogan NJ. 2020. A SARS-CoV-2 protein interaction map reveals targets for drug repurposing. *Nature* **583**:459–468. doi:10.1038/s41586-020-2286-9

Ho SN, Biggar SR, Spencer DM, Schreiber SL, Crabtree GR. 1996. Dimeric ligands define a role for transcriptional activation domains in reinitiation. *Nature* **382**:822–826. doi:10.1038/382822a0

Hoffmann H-H, Schneider WM, Rice CM. 2015. Interferons and viruses: an evolutionary arms race of molecular interactions. *Trends Immunol* **36**:124–138. doi:10.1016/j.it.2015.01.004

Htet ZM, Gillies JP, Baker RW, Leschziner AE, DeSantis ME, Reck-Peterson SL. 2020. LIS1 promotes the formation of activated cytoplasmic dynein-1 complexes. *Nat Cell Biol* **22**:518–525. doi:10.1038/s41556-020-0506-z

Huynh W, Vale RD. 2017. Disease-associated mutations in human BICD2 hyperactivate motility of dynein–dynactin. *Journal of Cell Biology* **216**:3051–3060. doi:10.1083/jcb.201703201

Ilan-Ber T, Ilan Y. 2019. The role of microtubules in the immune system and as potential targets for gut-based immunotherapy. *Molecular Immunology* **111**:73–82. doi:10.1016/j.molimm.2019.04.014

Jassal B, Matthews L, Viteri G, Gong C, Lorente P, Fabregat A, Sidiropoulos K, Cook J, Gillespie M, Haw R, Loney F, May B, Milacic M, Rothfels K, Sevilla C, Shamovsky V, Shorser S, Varusai T, Weiser J, Wu G, Stein L, Hermjakob H, D'Eustachio P. 2020. The reactome pathway knowledgebase. *Nucleic Acids Res* **48**:D498–D503. doi:10.1093/nar/gkz1031

Johnson B, VanBlargan LA, Xu W, White JP, Shan C, Shi P-Y, Zhang R, Adhikari J, Gross ML, Leung DW, Diamond MS, Amarasinghe GK. 2018. Human IFIT3 Modulates IFIT1 RNA Binding Specificity and Protein Stability. *Immunity* **48**:487-499.e5. doi:10.1016/j.immuni.2018.01.014

Kapitein LC, Schlager MA, van der Zwan WA, Wulf PS, Keijzer N, Hoogenraad CC. 2010. Probing Intracellular Motor Protein Activity Using an Inducible Cargo Trafficking Assay. *Biophysical Journal* **99**:2143–2152. doi:10.1016/j.bpj.2010.07.055

Kast DJ, Dominguez R. 2017. The Cytoskeleton–Autophagy Connection. *Current Biology* **27**:R318–R326. doi:10.1016/j.cub.2017.02.061

Katoh K. 2002. MAFFT: a novel method for rapid multiple sequence alignment based on fast Fourier transform. *Nucleic Acids Research* **30**:3059–3066. doi:10.1093/nar/gkf436

Kersten FF, van Wijk E, Hetterschijt L, Bauβ K, Peters TA, Aslanyan MG, van der Zwaag B, Wolfrum U, Keunen JE, Roepman R, Kremer H. 2012. The mitotic spindle protein SPAG5/Astrin connects to the Usher protein network postmitotically. *Cilia* **1**:2.

Kosakovsky Pond SL, Frost SDW. 2005. Not So Different After All: A Comparison of Methods for Detecting Amino Acid Sites Under Selection. *Molecular Biology and Evolution* **22**:1208–1222. doi:10.1093/molbev/msi105

Labun K, Montague TG, Gagnon JA, Thyme SB, Valen E. 2016. CHOPCHOP v2: a web tool for the next generation of CRISPR genome engineering. *Nucleic Acids Res* **44**:W272-276. doi:10.1093/nar/gkw398

Latner DR, Thompson JM, Gershon PD, Storrs C, Condit RC. 2002. The positive transcription elongation factor activity of the vaccinia virus J3 protein is independent from its (nucleoside-2'-O-) methyltransferase and poly(A) polymerase stimulatory functions. *Virology* **301**:64–80. doi:10.1006/viro.2002.1538

Lau CK, O'Reilly FJ, Santhanam B, Lacey SE, Rappsilber J, Carter AP. 2021. Cryo-EM reveals the complex architecture of dynactin's shoulder region and pointed end. *EMBO J* **40**:e106164. doi:10.15252/embj.2020106164

Lee I-G, Cason SE, Alqassim SS, Holzbaur ELF, Dominguez R. 2020. A tunable LIC1-adaptor interaction modulates dynein activity in a cargo-specific manner. *Nat Commun* **11**:5695. doi:10.1038/s41467-020-19538-7

Lei J, Hilgenfeld R. 2017. RNA-virus proteases counteracting host innate immunity. *FEBS Lett* **591**:3190–3210. doi:10.1002/1873-3468.12827

Liu Y, Salter HK, Holding AN, Johnson CM, Stephens E, Lukavsky PJ, Walshaw J, Bullock SL. 2013. Bicaudal-D uses a parallel, homodimeric coiled coil with heterotypic registry to coordinate recruitment of cargos to dynein. *Genes Dev* **27**:1233–1246. doi:10.1101/gad.212381.112

Love MI, Huber W, Anders S. 2014. Moderated estimation of fold change and dispersion for RNA-seq data with DESeq2. *Genome Biol* **15**:550. doi:10.1186/s13059-014-0550-8

Luby-Phelps K. 2000. Cytoarchitecture and physical properties of cytoplasm: volume, viscosity, diffusion, intracellular surface area. *International review of cytology* **192**:189–221.

Man SM, Kanneganti T-D. 2016. Converging roles of caspases in inflammasome activation, cell death and innate immunity. *Nat Rev Immunol* **16**:7–21. doi:10.1038/nri.2015.7

McCune BT, Lanahan MR, tenOever BR, Pfeiffer JK. 2020. Rapid Dissemination and Monopolization of Viral Populations in Mice Revealed Using a Panel of Barcoded Viruses. *J Virol* **94**:e01590-19. doi:10.1128/JVI.01590-19

McKenney RJ, Huynh W, Tanenbaum ME, Bhabha G, Vale RD. 2014. Activation of cytoplasmic dynein motility by dynactin-cargo adapter complexes. *Science (New York, NY)* **345**:337–341.

Meyerson NR, Sawyer SL. 2011. Two-stepping through time: mammals and viruses. *Trends in Microbiology* **19**:286–294. doi:10.1016/j.tim.2011.03.006

Mostowy S, Shenoy AR. 2015. The cytoskeleton in cell-autonomous immunity: structural determinants of host defence. *Nat Rev Immunol* **15**:559–573. doi:10.1038/nri3877

Murrell B, Wertheim JO, Moola S, Weighill T, Scheffler K, Kosakovsky Pond SL. 2012. Detecting Individual Sites Subject to Episodic Diversifying Selection. *PLoS Genet* **8**:e1002764. doi:10.1371/journal.pgen.1002764

Ng CS, Stobart CC, Luo H. 2021. Innate immune evasion mediated by picornaviral 3C protease: Possible lessons for coronaviral 3C-like protease? *Rev Med Virol* **31**:1–22. doi:10.1002/rmv.2206

Olenick MA, Holzbaur ELF. 2019. Dynein activators and adaptors at a glance. *J Cell Sci* **132**. doi:10.1242/jcs.227132

Passmore JB, Nijenhuis W, Kapitein LC. 2021. From observing to controlling: Inducible control of organelle dynamics and interactions. *Current Opinion in Cell Biology* **71**:69–76. doi:10.1016/j.ceb.2021.02.002

Patro R, Duggal G, Love MI, Irizarry RA, Kingsford C. 2017. Salmon provides fast and bias-aware quantification of transcript expression. *Nat Methods* **14**:417–419. doi:10.1038/nmeth.4197

Radtke K, Döhner K, Sodeik B. 2006. Viral interactions with the cytoskeleton: a hitchhiker's guide to the cell. *Cellular Microbiology* **8**:387–400.

Reck-Peterson SL, Redwine WB, Vale RD, Carter AP. 2018. The cytoplasmic dynein transport machinery and its many cargoes. *Nature Reviews Molecular Cell Biology* **19**:382–398. doi:10.1038/s41580-018-0004-3

Redwine WB, DeSantis ME, Hollyer I, Htet ZM, Tran PT, Swanson SK, Florens L, Washburn MP, Reck-Peterson SL. 2017. The human cytoplasmic dynein interactome reveals novel activators of motility. *eLife* **6**:379.

Rothenburg S, Brennan G. 2020. Species-Specific Host–Virus Interactions: Implications for Viral Host Range and Virulence. *Trends in Microbiology* **28**:46–56. doi:10.1016/j.tim.2019.08.007

Schlager MA, Hoang HT, Urnavicius L, Bullock SL, Carter AP. 2014. In vitro reconstitution of a highly processive recombinant human dynein complex. *The EMBO journal* **33**:1855–1868.

Schoggins JW. 2019. Interferon-Stimulated Genes: What Do They All Do? *Annu Rev Virol* **6**:567–584. doi:10.1146/annurev-virology-092818-015756

Seksek O, Biwersi J, Verkman AS. 1997. Translational Diffusion of Macromolecule-sized Solutes in Cytoplasm and Nucleus. *Journal of Cell Biology* **138**:131–142. doi:10.1083/jcb.138.1.131

Tenthorey JL, Emerman M, Malik HS. 2022. Evolutionary Landscapes of Host-Virus Arms Races. *Annu Rev Immunol* **40**:271–294. doi:10.1146/annurev-immunol-072621-084422

Terawaki S, Yoshikane A, Higuchi Y, Wakamatsu K. 2015. Structural basis for cargo binding and autoinhibition of Bicaudal-D1 by a parallel coiled-coil with homotypic registry. *Biochemical and Biophysical Research Communications* **460**:451–456. doi:10.1016/j.bbrc.2015.03.054

Tsu Brian, Beierschmitt C, Ryan AP, Agarwal R, Mitchell PS, Daugherty MD. 2021. Diverse viral proteases activate the NLRP1 inflammasome. *eLife* **10**:e60609. doi:10.7554/eLife.60609

Tsu Brian, Fay EJ, Nguyen KT, Corley MR, Hosuru B, Dominguez VA, Daugherty MD. 2021. Running With Scissors: Evolutionary Conflicts Between Viral Proteases and the Host Immune System. *Front Immunol* **12**:769543. doi:10.3389/fimmu.2021.769543

Urnavicius L, Zhang K, Diamant AG, Motz C, Schlager MA, Yu M, Patel NA, Robinson CV, Carter AP. 2015. The structure of the dynactin complex and its interaction with dynein. *Science (New York, NY)* **347**:1441–1446.

van Wijk E, Kersten FFJ, Kartono A, Mans DA, Brandwijk K, Letteboer SJF, Peters TA, Märker T, Yan X, Cremers CWRJ, Cremers FPM, Wolfrum U, Roepman R, Kremer H. 2009. Usher syndrome and Leber congenital amaurosis are molecularly linked via a novel isoform of the centrosomal ninein-like protein. *Human molecular genetics* **18**:51–64.

Wang Y, Huynh W, Skokan TD, Lu W, Weiss A, Vale RD. 2019. CRACR2a is a calcium-activated dynein adaptor protein that regulates endocytic traffic. *Journal of Cell Biology* **218**:1619–1633. doi:10.1083/jcb.201806097

Weaver S, Shank SD, Spielman SJ, Li M, Muse SV, Kosakovsky Pond SL. 2018. Datamonkey 2.0: A Modern Web Application for Characterizing Selective and Other Evolutionary Processes. *Molecular Biology and Evolution* **35**:773–777. doi:10.1093/molbev/msx335

Woods Acevedo MA, Erickson AK, Pfeiffer JK. 2019. The Antibiotic Neomycin Enhances Coxsackievirus Plaque Formation. *mSphere* **4**:e00632-18. doi:10.1128/mSphere.00632-18

Xiao W, Yeerken D, Li J, Li Z, Jiang L, Li D, Fu M, Ma L, Song Y, Zhang W, Zhan Q. 2021. Nlp promotes autophagy through facilitating the interaction of Rab7 and FYCO1. *Signal Transduct Target Ther* **6**:152. doi:10.1038/s41392-021-00543-1

Yang Z. 2007. PAML 4: Phylogenetic Analysis by Maximum Likelihood. *Molecular Biology and Evolution* **24**:1586–1591. doi:10.1093/molbev/msm088

Yu H, Bruneau RC, Brennan G, Rothenburg S. 2021. Battle Royale: Innate Recognition of Poxviruses and Viral Immune Evasion. *Biomedicines* **9**:765. doi:10.3390/biomedicines9070765

Chapter 4: Summary and future directions

Concluding thoughts

The research described in Chapter 2 and 3 are examples of two distinct means by which viruses and hosts can engage with each other in an evolutionary struggle. In the case of NLRP1, we have characterized a system where the host has taken advantage of an existing viral evolutionary constraint–the necessity of genomic polyprotein processing by an encoded protease. While pyroptosis has been previously described as a cellular response to viral infection (Kuriakose & Kanneganti 2021), the NLRP1-mediated strategy hosts have employed to activate this response was previously unknown. Conversely, our investigation into the antiviral activity of NINL revealed a more canonical case of direct viral antagonism of a host immune component. However, NINL had not been previously identified as an effector of the innate immune system, nor an important player in the type I interferon response. The results of our research into these two genes, whose relationship with antiviral immunity was previously unexplored, underscore the utility and importance of our discovery pipeline in identifying future host-virus sites of interaction.

Identifying specific mechanism of NINL immune function

Our investigation into the role of NINL in antiviral immunity provided compelling evidence that NINL is involved in the import of the ISGF3 complex (pSTAT1, pSTAT2, and IRF9) into the nucleus of interferon-activated cells, as evidenced by significantly reduced import of pSTAT signal into the nucleus in NINL KO cells. While this observation provided valuable insight to the potential role of NINL, we were unable to establish a specific, dynein-dependent molecular mechanism.

One method by which we could determine how NINL is involved in ISGF3 import is by using a split fluorophore expression system and live-cell microscopy (Romei & Boxer 2019).

Briefly, we could genomically integrate inducible expression for a split fluorophore-fused NINL and a split fluorophore-fused component of ISGF3. In the absence of interferon induction, fluorescence signal should not be present. Upon interferon induction, if NINL is involved in the transport of this signal, we should see fluorescent signal, as well as the movement of signal to the nuclear region. Because one major limitation of split fluorophore expression systems is the lengthy fluorescent protein maturation time, it would be crucial to select for bimolecular fluorescent protein fragments that have been engineered to mature quickly under physiological conditions (Shyu, *et al.* 2009).

Broader investigation of NINL antiviral activity

In Chapter 3 and Figure 3.12, we briefly addressed the potential for broader, protease-mediated antagonism of NINL across different viral families. We were able to show that viruses from the *picornaviridae* and *coronaviridae* families have evolved different strategies to cleave NINL, but out of this panel, we only evaluated the contribution of NINL to viral replication for CVB3. In order to further establish the relationship between cleavage and viral replication, it is necessary to infect wild-type and NINL KO cells with the viruses whose proteases displayed differential cleavage strategies.

As evidenced by the successful implementation of 3CL^{pro} inhibitors like nirmatrelvir to reduce the progression of disease during SARS-CoV-2 infection (Hammond, et al. 2022), there is reasonable precedent to suggest that investigation of viral protease activity is important for understanding how viruses function in the context of human disease. While the essential nature of 3CL^{pro} in completing the viral replicative cycle is well-understood, the array of host targets antagonized by these viral proteases still requires further investigation. If the observed cleavage

of NINL is consequential to viral success, its antiviral activity could be important to understanding the natural course of infection and associated disease.

Determining potential viral antagonism of other cellular transport systems

At the commencement of our project, there were 13 bona fide activating adaptors of the dynein complex. Since then, several new adaptors have been identified and partially characterized (Agrawal, et al. 2022, Cason, et al. 2021, Chaaban & Carter, 2022, Fenton, et al. 2021, Lau et al. 2021, Lee et al. 2020, Olenick & Holzbaur, 2019, Reck-Peterson, et al. 2018). While it remains to be seen which of these new activating adaptors are rapidly evolving or antagonized by viral proteases, our preliminary investigations suggest that some are.

Logically, the most extensively studied targets of viral antagonism have been the canonical components of the innate, intrinsic, and adaptive immune system. Our research suggests that this investigative strategy, though effective, is likely to miss potentially impactful host-virus conflicts associated with intracellular trafficking. The results of research from Chapter 3 suggest that microtubule-associated transport components are important sites of potential viral antagonism. Although our studies focused on the dynein complex, it seems prudent to expand our scope to include kinesins and their co-factors. By taking a closer look at the machinery responsible for the transport of important cellular signals, rather than simply looking at antiviral pathway components, we stand to unveil previously unexplored territory in the fields of virology, immunology, and medicine.

The future of evolution-guided discovery

While our research has revealed novel and intriguing discoveries of how viruses and hosts interact with each other, we have only begun to scratch the surface of how the tools and methods we have developed could be used to further our understanding of molecular mechanisms of immune function and disease. Not only do we still have hundreds of rapidly evolving host candidates to investigate for their role in antiviral defense, but we also have an impressive array of potential picornaviral 3C protease targets to experimentally validate. Beyond more extensive experiments with our already compiled data, we also have the capability to query other 3C and 3C-like proteases to look for sites of host antagonism. It should be noted that this is not solely an intellectual exercise, but also one that is demonstrably useful to addressing viral burden on human disease. Recently, the 3C-like protease inhibitor nirmatrelavir (a component of the drug Paxlovid), has been shown to drastically reduce instances of mortality and overall viral load in high-risk individuals suffering from COVID-19 (Hammond, 2022; Wong, 2022). Because it is impossible to know which virus might be the causal agent for the next epidemic or pandemic, it is important to adopt new methods and perspectives to increase our chances of identifying new elements in the evolutionary struggle between pathogens and their hosts.

References

Agrawal R, Gillies JP, Zang JL, Zhang J, Garrott SR, Shibuya H, Nandakumar J, DeSantis ME. 2022. The KASH5 protein involved in meiotic chromosomal movements is a novel dynein activating adaptor (preprint). Cell Biology. doi:10.1101/2022.03.11.483947

Cason SE, Carman PJ, Van Duyne C, Goldsmith J, Dominguez R, Holzbaur ELF. 2021. Sequential dynein effectors regulate axonal autophagosome motility in a maturation-dependent pathway. *Journal of Cell Biology* **220**:e202010179. doi:10.1083/jcb.202010179

Chaaban S, Carter AP. 2022. Structure of dynein-dynactin on microtubules shows tandem recruitment of cargo adaptors (preprint). *Molecular Biology*. doi:10.1101/2022.03.17.482250

Fenton AR, Jongens TA, Holzbaur ELF. 2021. Mitochondrial adaptor TRAK2 activates and functionally links opposing kinesin and dynein motors. *Nat Commun* **12**:4578. doi:10.1038/s41467-021-24862-7

Hammond J, Leister-Tebbe H, Gardner A, Abreu P, Bao W, Wisemandle W, Baniecki M, Hendrick VM, Damle B, Simón-Campos A, Pypstra R, Rusnak JM; EPIC-HR Investigators. 2022. Oral Nirmatrelvir for High-Risk, Nonhospitalized Adults with Covid-19. *N Engl J Med*. **386(15):**1397-1408. doi: 10.1056/NEJMoa2118542

Kuriakose T, Kanneganti TD. Pyroptosis in Antiviral Immunity. 2019. *Curr Top Microbiol Immunol.* **25**:10.1007/82_2019_189. doi: 10.1007/82_2019_189

Lau CK, O'Reilly FJ, Santhanam B, Lacey SE, Rappsilber J, Carter AP. 2021. Cryo-EM reveals the complex architecture of dynactin's shoulder region and pointed end. *EMBO J* **40**:e106164. doi:10.15252/embj.2020106164

Lee I-G, Cason SE, Alqassim SS, Holzbaur ELF, Dominguez R. 2020. A tunable LIC1-adaptor interaction modulates dynein activity in a cargo-specific manner. *Nat Commun* **11**:5695. doi:10.1038/s41467-020-19538-7

Olenick MA, Holzbaur ELF. 2019. Dynein activators and adaptors at a glance. *J Cell Sci* **132**. doi:10.1242/jcs.227132

Reck-Peterson SL, Redwine WB, Vale RD, Carter AP. 2018. The cytoplasmic dynein transport machinery and its many cargoes. *Nature Reviews Molecular Cell Biology* **19**:382–398. doi:10.1038/s41580-018-0004-3

Romei MG, Boxer SG. 2019. Split Green Fluorescent Proteins: Scope, Limitations, and Outlook. *Annu Rev Biophys*. **48**:19-44. doi: 10.1146/annurev-biophys-051013-022846

Shyu YJ, Liu H, Deng X, Hu CD. 2006. Identification of new fluorescent protein fragments for bimolecular fluorescence complementation analysis under physiological conditions. *Biotechniques*. **40(1):**61-6. doi: 10.2144/000112036

Wong CKH, Au ICH, Lau KTK, Lau EHY, Cowling BJ, Leung GM. 2022. Real-world effectiveness of early molnupiravir and nirmatrelvir/ritonavir among hospitalized, non-oxygen-dependent COVID-19 patients on admission during Hong Kong's Omicron BA.2 wave: an observational study. *medRxiv* 22275291; doi:10.1101/2022.05.19.22275291